



APPROVAL SHEET

Title of Dissertation: Molecular Interactions between Luminescent Quantum Dots  
and Bacteria

Name of Candidate: Denise Nicole Williams-Harris  
Doctor of Philosophy, 2020

Dissertation and Abstract Approved: \_\_\_\_\_



Zeev Rosenzweig, Ph.D.  
Professor and Department Chair  
Department of Chemistry and Biochemistry

Date Approved: 07/23/2020

NOTE: \*The Approval Sheet with the original signature must accompany the thesis or dissertation. No terminal punctuation is to be used.

## ABSTRACT

Title of Document: MOLECULAR INTERACTIONS BETWEEN LUMINESCENT QUANTUM DOTS AND BACTERIA

Denise Nicole Williams-Harris, Doctor of Philosophy, 2020

Directed By: Professor Zeev Rosenzweig, Ph.D., Department of Chemistry and Biochemistry

Luminescent semiconductor quantum dots (QDs) are continuously incorporated into bioassay, imaging, and treatment technologies. Cadmium-based QDs are commonly used in these technologies because of their superior optical properties—within the visible to near infrared wavelengths of light—compared to QDs made of other materials. However, concerns about cadmium toxicity have led to the increased use of protective coatings around cadmium-based QDs and to the development of QDs composed of more benign materials. The varying methods used to attain these QDs produce them with inherently different materials and structures. Additionally, QDs have varying homogeneous or heterogeneous surface chemistries. The QD surface may be either organic or aqueous-miscible; neutrally, positively, or negatively charged; and comprised of either short ligands, bulky biomolecules, or long polymeric chains. The different QD materials, structures, and surface chemistries impact whether QDs will associate with cells, and dictate what other interactions may occur after association.

Our studies aim to concurrently investigate the impact that varying QDs' compositions have on their interactions with human and environmental health models in the context of antibacterial research. This context is important since there is currently a rise in the development of QD-based antibacterial treatments, which harness the inherent cytotoxic activity of QDs and steers it towards the rising onset of multidrug-resistant bacteria. Thus, this dissertation investigates the interactions of QDs with model liposomes, bacterial cells, and human red blood cells. We specifically compared the interactions of 1) CdSe core to ZnSe core QDs, 2) core QDs to ZnS-shelled QDs, 3) QDs with negatively charged ligand terminations to positively charged ligand terminations, and 4) core QDs of varying amine content surface coverage with these models. Various techniques—such as absorbance, emission, mass spectrometry, microscopy, dynamic light scattering, zeta potential, and FRET measurements—were used to characterize the QDs' compositions and their interactions with the biological models. These studies have increased our mechanistic understanding of the interactions between QDs and cells, how to control these interactions, and how to design future QD technologies to have intended interactions with targeted organisms while maintaining minimal impact on organisms which are essential to human and environmental health.

MOLECULAR INTERACTIONS BETWEEN LUMINESCENT QUANTUM DOTS  
AND BACTERIA

By

Denise Nicole Williams-Harris

Dissertation submitted to the Faculty of the Graduate School of the  
University of Maryland, Baltimore County, in partial fulfillment  
of the requirements for the degree of  
Doctor of Philosophy  
2020

© Copyright by  
Denise Nicole Williams-Harris  
2020



## Dedication

For my Nana, who—even posthumous—prompts me to stay focused.

## Acknowledgements

I want to express my deepest appreciation to Dr. Rosenzweig and fellow members of the Rosenzweig lab. Dr. Rosenzweig, you have been pivotal for the development of my scientific and professional skills. Further, your trust in and promotion of my capabilities have been key to the opportunities I have received and the confidence I have had to pursue them. Dr. Swapnil Ambade, Richard Brown, Zachary Clifford, Dr. Taeyuana Curry, Meghan Dands, Em Demiral, Ewa Harazinska, Dr. Jessica Heimann, Chana Honick, Kazi Z. Hossain, Karina Keefe, Laura Kesner, Jenny Klutts, April Laranang, Daniel Morgan, Kaila Noland, Jessica Park, Connor Riahin, Melissa Richardson, Shreyasi Sengupta, Danielle Tyson, and Zheng Zheng—we have known each other for different lengths of time, but our work and personal identities have certainly entwined for the better. To the several seasonal Rosenzweig trainees that I have had the pleasure of interacting with, you are a part of the fuel to my desire to continue in STEM mentorship.

I also want to express my deepest appreciation to the former and current members of my dissertation committee—Drs. Mark Allen, Minjoung Kyoung, Galya Orr, Aaron Smith and Michael Summers. Each of you have challenged and developed my critical awareness and communication of the science included in this document and elsewhere. Thank you for your time, patience, influence, and willingness to mentor me.

I want to recognize the faculty, staff, fellow trainees, and associates of UMBC's Department of Chemistry and Biochemistry, collectively, for your work ethic and various influences in my graduate career. Thank you to Dr. Sarah Bass, Dr.

Tara Carpenter, and Frank Tyminski for your mentorship, trust, and forthright conversation. Thank you Dr. Seley-Radtke for your individual mentorship and facilitation of the Chemistry-Biology Interface program which has been pivotal to my perspective of multidisciplinary research. Thank you Tony Baney, Dennis Cuddy, Patricia Gagne, Brian Moravec, Michele Mullins, Ramona Patel, and Creighton Smith for being approachable and helping me navigate the various duties and responsibilities involved in chemical education. Thank you Josh Wilhide, Maggie LaCourse, Ian Shaffer and the other UMBC Molecular Characterization and Analysis Complex associates who have trained and assisted me. Thank you Dr. Viknesh Sivanathan and the HHMI Science Education group for training me and allowing me to share your microbiology facilities. Thank you peer graduate students who have sat in on my practice talks, studied with me through courses, and been available for conversation and collaboration.

I very much appreciate the PROMISE community, the UMBC graduate school, Erika Aparaka, Denise Atkinson, Dr. Wendy Carter-Veale, Shawnisha Hester, Sunji Jangha, Hector Medina, Yarazeth Medina, and Dr. Renetta Tull. I also very much appreciate the Meyerhoff Graduate Fellows and Dr. Rachel Brewster, Sharon Graves, Dr. Lisa Jones, Justine Johnson, Dr. Mike Summers who facilitate the program. These networks have often been the people and spaces that I have looked to for inspiration and to relate to as I have navigated higher education and research environments.

I gratefully acknowledge Dr. Christy Haynes, Miriam Krause, Dr. Karen Lienkamp, Dr. Sunipa Pramanik, Michael Schwarts, and the other scientists that I

have had to opportunity to interact with due to collaborative research activities through the Center for Sustainable Nanotechnology (CSN).

I also had the pleasure of being trained by and conversing with Dr. Alline Myers at the National Institute of Standards and Technology (NIST) during microscopic imaging training sessions.

Finally, I'd like to acknowledge the sources of my grit—my family, my friends, and God. To my mom, dad, sisters, and extensive family for relentlessly cheering me on. To my husband for supporting my career pursuit. To Ashley Mitchell and Miji Jeon for growing from peer mentors and friends into family. To my church family, for reaching out and for getting mementos to mark my achievements even before they had been attained. And to God, for listening even when I pretended not to need to talk.

# Table of Contents

Dedication .....	ii
Acknowledgements .....	iii
Table of Contents .....	vi
List of Tables .....	ix
List of Figures .....	x
List of Schemes .....	xiv
Abbreviations .....	xv
Chapter 1: Introduction to the study of molecular interactions between luminescent quantum dots and bacterial cells .....	1
1.1 Luminescent Semiconductor Quantum Dots .....	1
1.2 Account of Traditional Antibacterials: Metals and Small Molecule Antibiotics .....	3
1.2.1 Interactions between Bacteria and Metals .....	3
1.2.2 Interactions between Bacteria and Small Molecule Antibiotics .....	6
1.2.3 Antibiotic Resistance .....	8
1.3 Account of Nontraditional Antibacterials: Peptides, Polymers, and Nanoparticles .....	11
1.3.1 Interactions between Bacteria and Antimicrobial Peptides .....	13
1.3.2 Interactions between Bacteria and Antimicrobial Polymers .....	15
1.3.3 Interactions between Bacteria and Nanoparticles .....	17
1.3.4 Interactions between Bacteria and QD Conjugates .....	20
1.4 Project Goals: Understanding the Interactions between Luminescent Semiconductor QDs and Bacteria at the Molecular Level .....	22
Chapter 2: Synthesis and Characterization of Luminescent Semiconductor Quantum Dots .....	25
2.1 Purpose .....	25
2.2 Introduction .....	25
2.3 Materials and Instrumentation .....	28
2.3.1 Materials and Reagents .....	28
2.3.2 Instrumentation .....	29
2.4 QD Synthesis and Characterization .....	29
2.4.1 CdSe and CdSe/ZnS QDs' Synthesis and Characterization .....	30
2.4.2 Characterization of Purchased CdSe/ZnS QDs .....	34
2.4.3 CdTe QDs' Synthesis and Characterization .....	35
2.4.4 ZnSe, ZnSe/ZnS, and Mn:ZnSe/ZnS QDs' Synthesis and Characterization .....	37
2.5 Conclusion .....	40
Chapter 3: Using liposomes to model mechanisms of interaction between quantum dots and cell membranes .....	41
3.1 Purpose .....	41
3.2 Introduction .....	41
3.3 Materials, Instrumentation, and Methods .....	43
3.3.1 Materials and Reagents .....	43
3.3.2 Instrumentation .....	44

3.3.3 QDs' DHLA-PEG750-OCH <sub>3</sub> Ligand Exchange.....	45
3.3.4 Inductively Coupled Plasma Mass Spectrometry .....	45
3.3.5 Preparation of Calcein-Containing Liposomes.....	46
3.3.6 Preparation of Dye-Free Liposomes .....	47
3.3.7 Liposomes Lysis Assays.....	47
3.3.8 Preparation of Nitrobenzoxadiazole(NBD)-Labeled Liposomes.....	49
3.3.9 Fluorescence Lifetime Assays of NBD-Labeled Liposomes.....	49
3.3.10 Preparation of Rhodamine-Labeled Liposomes.....	49
3.3.11 Liposome Förster Resonance Energy Transfer (FRET) Assay.....	50
3.4 Investigating Varying Anti-Membrane Activity with QDs of Different Semiconductor Material Composition and Structure.....	51
3.4.1 Ligand Exchange of Cadmium-containing and Cadmium-free QDs.....	51
3.4.2 Using Calcein-containing Liposomes to Investigate the Dependence of Membrane Disruption Activity on QD Cores' Material Composition .....	52
3.4.3 Using Calcein-containing Liposomes to Investigate the Dependence of Membrane Disruption Activity on QDs' Core or Core/Shell Structure .....	55
3.4.4 Using Nitrobenzoxadiazole (NBD)-labeled Liposomes to Investigate Changes in Polarity and ROS Activity at the Membrane .....	58
3.5 Investigating Varying QD-Membrane Association Activity with Liposomes of Different Lipid Compositions .....	62
3.5.1 Establishing and Optimizing a Förster Resonance Energy Transfer (FRET) System to Investigate Levels of QD Association with Membranes .....	62
3.5.2 Using Rhodamine-labeled Liposomes of Varying Lipid Composition to Investigate the Impact of Lipid Composition on QD Association.....	66
3.6 Conclusions.....	70
Chapter 4: Investigating the Antibacterial Activity of Cadmium-containing and Cadmium-free QDs against <i>Shewanella oneidensis</i> MR-1, an Environmental Health Model.....	73
4.1 Purpose.....	73
4.2 Introduction.....	73
4.3 Materials, Instrumentation, and Methods .....	74
4.3.1 Materials and Reagents .....	74
4.3.2 Instrumentation .....	75
4.3.3 Bacterial Culture and Colony Counting.....	75
4.3.4 Inductively Coupled Plasma Mass Spectrometry .....	77
4.3.5 Cytoviva Hyperspectral Imaging .....	78
4.3.6 Biological Transmission Electron Microscopy.....	78
4.4 Reference to QDs' Synthesis, Ligand Exchange, and Liposome Interactions	79
4.5 Investigating Cadmium-containing and Cadmium-free QDs' Association with <i>Shewanella oneidensis</i> MR-1.....	80
4.5.1 Using ICP-MS to Investigate QD-Bacteria Association.....	80
4.5.2 Using Hyperspectral Imaging to Investigate QD-Bacteria Association ...	81
4.5.3 Using BioTEM to Investigate QD-Bacteria Association.....	84
4.6 Investigating the Impact of QDs on <i>Shewanella oneidensis</i> MR-1 Viability..	86
4.6.1 Cadmium-free and Cadmium-containing QDs' Impact on Cell Viability	86
4.6.2 Additional Modifications Which Impact QDs' Viability Implications ....	87

4.7 Conclusions.....	90
Chapter 5: Investigating the Activity of Polymer- and Peptide-coated CdTe QDs with Human Health Cell Models. ....	92
5.1 Purpose.....	92
5.2 Introduction.....	92
5.3 Materials, Instrumentation, and Methods .....	96
5.3.1 Materials and Reagents.....	96
5.3.2 Ethics Statement.....	97
5.3.3 Instrumentation .....	97
5.3.4 Coupling LL-37 and PONS to MPA-CdTe QDs .....	98
5.3.5 H <sub>2</sub> DCF Fluorescence Assay for Detection of ROS .....	98
5.3.6 Thermogravimetric Analysis (TGA) of MPA-QDs and QD Conjugates .	99
5.3.7 Minimum Inhibitory Concentration (MIC) Assay with Bacteria .....	99
5.3.8 Hemolysis Assay.....	101
5.4 Investigating the Activity of MPA-coated CdTe Core QDs.....	103
5.4.1 Reactive Oxygen Species Generation of CdTe QDs .....	103
5.4.2 Biological Characterization of MPA-CdTe QDs.....	104
5.5 Investigating the Activity of PONS-coated CdTe QDs.....	105
5.5.1 Characterization of PONS-CdTe QDs.....	105
5.5.2 Antibacterial Activity of the free PONS and PONS-QDs Series .....	108
5.5.3 Hemolytic Activity of the free PONS and PONS-QDs Series.....	111
5.5.4 Therapeutic Indices of free PONS vs PONS-QDs Series .....	113
5.6 Investigating the Activity of LL-37-coated CdTe QDs .....	114
5.6.1 Characterization of LL-37-coated QDs .....	114
5.6.2 Biological Activity of LL-37-coated QDs .....	114
5.7 Conclusions.....	116
Chapter 6: Conclusions.....	118
6.1 Summary .....	118
6.2 Future Directions .....	121
Appendices.....	123
Bibliography .....	139

## List of Tables

### **Chapter 3**

**Table 3.1.** A summary of the fluorescence lifetime and exponential terms used to fit the fluorescence lifetime decay curves for NBD-liposomes prior to and following exposure to CdSe and ZnSe QDs.

## List of Figures

### Chapter 1

- Figure 1.1:** The quantum confinement effect on bulk energy bands.
- Figure 1.2:** Biosorption mechanisms for metal uptake into bacteria.
- Figure 1.3:** General structures of common small molecule antibiotic classes.
- Figure 1.4:**  $\beta$ -lactam antibiotics before and after inactivation by  $\beta$ -lactamases.
- Figure 1.5:** The number of drug candidates in various stages of the clinical pipeline between 2014 and 2019.
- Figure 1.6:** Molecular structures of ceftaroline and ceftolozane, antibiotic analogues of ceftazidime.
- Figure 1.7:** The ‘Shai-Matsuzaki-Huang’ or ‘carpet’ model explanation of antibacterial activity.
- Figure 1.8:** Chemical structure of the poly(oxanorbornene) mimics of AMPs.
- Figure 1.9:** The Van@ZnO-PEP-MPA antimicrobial probe.

### Chapter 2

- Figure 2.1:** Representation of a CdSe core (black) with 1 (red), 3 (blue), and 6 (green) monolayers of a ZnS shell.
- Figure 2.2:** Normalized absorption (A), emission (B), and lifetime decay (C) spectra of CdSe and CdSe/ZnS QDs.
- Figure 2.3:** Normalized absorption (dotted) and emission spectra (solid) (A) and DLS analysis (B) of the Qdots.
- Figure 2.4:** Normalized absorption (dotted) and emission spectra (solid) (A) and DLS analysis (B) of the CdTe QDs.
- Figure 2.5:** Normalized absorption (A), emission (B), and lifetime (C) spectra of ZnSe, ZnSe/ZnS, and Mn:ZnSe/ZnS QDs.
- Figure 2.6:** Representative image summary of QDs in this dissertation, by chapter.

### Chapter 3

- Figure 3.1:** Representative normalized emission traces compare the membrane disruption activity of CdSe and CdSe/ZnS QDs (A) and ZnSe and ZnSe/ZnS QDs (B). The negative control curves follow the exposures of calcein-free liposomes to the shelled QDs. Liposome lysis efficiency is concentration dependent for the cadmium-containing (C) and cadmium-free (D) QDs. (N = 3).
- Figure 3.2:** Normalized emission traces from calcein-filled liposomes exposed to CdSe QDs with 0 to 6 monolayers (ML) of a ZnS shell. (While measurements were done in triplicate, only one representative trace is shown.)
- Figure 3.3:** ICP-MS measured intensities of zinc, cadmium, and selenium ions resulting from the dissolution of CdSe QDs of varying ZnS shell size. Only significant zinc ion dissolution is observed, indicating degradation of the ZnS shell in the timespan of our assays. (N = 3; Error bars are omitted for figure clarity. Published as Figure 3B in Williams et al. Applied Nano Materials. 2018, 1 (9), 4788-4800.)

- Figure 3.4:** Fluorescence intensity of NBD-labeled liposomes (black), QDs (blue), and following a 4 hr incubation of NBD-labeled liposomes with QDs (red) show significant NBD fluorescence increase for both CdSe (A) and ZnSe (B) QDs ( $\lambda_{\text{ex}} = 470 \text{ nm}$ ). Time-resolved photoluminescence decay curves of NBD-liposomes (black) and following a 4 hr incubation with QDs (red) for CdSe QDs (C) and ZnSe QDs (D) show a decrease in fluorescence lifetime ( $\lambda_{\text{ex}} = 470 \text{ nm}$ ,  $\lambda_{\text{em}} = 515 \text{ nm}$ ).
- Figure 3.5:** Spectra showing the spectral overlap and potential for FRET between the Qdot donors (black) and rhod-liposome acceptors (red). ( $\lambda_{\text{ex}} = 450 \text{ nm}$ )
- Figure 3.6:** Optical properties of rhod-liposomes with varying rhod-POPE content. The absorbance intensity of the liposomes increases with increasing rhod-POPE mol% (A). With direct rhod-liposome excitation ( $\lambda_{\text{ex}} = 570 \text{ nm}$ ), the emission intensity increases up to the 3 mol% rhod-POPE formulation and decreases after 6 mol% rhod-POPE, with concentration dependence (B). With indirect rhod-liposome excitation ( $\lambda_{\text{ex}} = 450 \text{ nm}$ ), the emission intensity increases up to the 6 mol% rhod-POPE formulation and decreases immediately after, with concentration dependence (C).
- Figure 3.7:** Emission from Qdot-rhodamine FRET system with increasing concentrations of Qdots show concentration dependent emission intensities. ( $\lambda_{\text{ex}} = 450 \text{ nm}$ )
- Figure 3.8:** Emission spectra after observing FRET between Qdots and 3 mol% rhod-POPE:POPC liposomes. Amino Qdots (red) have a smaller emission intensity at time 0 of FRET than the carboxyl Qdots (black) (A). Over time the trend remains that the carboxyl Qdots (B, red) have greater emission intensity with FRET than the amino Qdots (C, red). However, there is no significant difference in the amount of emission detected from the rhod-liposomes (B & C, black) between the two Qdots. (N = 2)
- Figure 3.9:** Emission spectra after observing FRET between Qdots and 3 mol% rhod-POPE liposome formulations that are either more negatively (blue), neutrally (black), or positively (red) charged due to the different lipid components. Carboxyl Qdots had more significantly decreased emissions (A) and induced more rhodamine emissions (C) in the presence of more positively charge liposomes compared to other formulations. The amino Qdots compounding negative charge and surface amine characteristics resulted in more significant interaction with both the positively and negatively charge liposome formulations (B and D). (N = 2)

#### **Chapter 4**

- Figure 4.1:** ICP-MS of QD-incubated bacterial exposures. (N = 3; Error bars are omitted for figure clarity.)
- Figure 4.2:** Hyperspectral reflectance microscopy library images of *S. oneidensis* (A), CdSe QDs (B), and CdSe/ZnS(3ML) QDs (C). The QDs are false-colored red. The spectral reference libraries are shown to the right of each image. (Published as Figure 6 in Williams et al. Applied Nano Materials. 2018, 1 (9), 4788-4800.)

- Figure 4.3:** Images of QD-incubated bacteria which were analyzed using the reference spectral libraries in Figure 4.2. *S. oneidensis* (gray) were exposed to CdSe core (A) and CdSe/ZnS (B) QDs (red). In many cases, QDs are in the vicinity of bacteria, which is indicative of QD-membrane association. (Published as Figure 7 in Williams *et al.* Applied Nano Materials. 2018, 1 (9), 4788-4800.)
- Figure 4.4:** Representative BioTEM micrographs of *S. oneidensis* treated with ZnSe/ZnS QDs (A-B) and CdSe/ZnS QDs (C-D). Images A-B show ZnSe/ZnS QD-associated bacteria with expected cell shape and integrity. Images C-D show CdSe/ZnS QD-associated bacteria with significant cell malformations, membrane disintegration, and release of cell organelles.
- Figure 4.5:** *S. oneidensis* colony growth after exposure to increasing concentrations of ZnSe (A), ZnSe/ZnS (B), CdSe (C), and CdSe/ZnS(3ML) (D) QDs compared to negative controls (NC, QD free bacteria) on each plate. The QD concentration increases counterclockwise around the plates.
- Figure 4.6:** Normalized *S. oneidensis* viability as a function of ZnSe and ZnSe/ZnS QDs' (A) and CdSe and CdSe/ZnS(3ML) QDs' (B) concentration. (N=4; Note the different x-axis scales.)
- Figure 4.7:** Normalized *S. oneidensis* viability after exposure to CdSe/ZnS QDs of increasing shell thickness. (N=4)
- Figure 4.8:** Normalized *S. oneidensis* viability after exposure to Mn:ZnSe/ZnS QDs. (N=3)

## **Chapter 5**

- Figure 5.1:** The solution structure of human LL-37 shown as an ensemble of 28 out of 200 backbone residues (A), a ribbon representation with the hydrophobic side chains labeled (B), and a potential energy surface (C).<sup>1</sup>
- Figure 5.2:** Structure of the BOC-protected butyl amine (B) and diamine (D) oxanorbornene monomers.
- Figure 5.3:** Fluorescence emission profile of H<sub>2</sub>DCF (t = 0, black) compared to the air-oxidation derived DCF (t = 6 hr, red) ( $\lambda_{\text{ex}} = 495 \text{ nm}$ ) (A). The rate of the oxidative ROS generation with increasing MPA-QDs concentration is faster than air oxidation of H<sub>2</sub>DCF samples ( $\lambda_{\text{ex}} = 495 \text{ nm}$ ,  $\lambda_{\text{em}} = 525 \text{ nm}$ , N = 3) (B).
- Figure 5.4:** MPA-QDs cause a concentration dependent decrease in *E. coli* cell growth with (red) and without (black) irradiation, but do not affect *S. aureus* cell growth (blue) at tested concentrations(A). The MPA-QDs had no significant hemolytic activity at tested concentrations (B). (N $\geq$ 3 biological replicates.)
- Figure 5.5:** Zeta potential measurements show the MPA-QDs to be negatively charged and the PONs-QDs to be positively charged (A). TGA analysis show similar mass losses due to desorption of 55% (red), 75% (black), 95% (green), and 100% (blue) amine PONs from the surface of MPA-CdTe QDs (purple) with weak dependence on the amine/alkyl ratio in the conjugated PONs (B). Cell-free H<sub>2</sub>DCF ROS measurements with 6.25

$\mu\text{g/mL}$  PONs/ $12.5 \text{ nM}$  QDs equivalents demonstrate higher ROS generation levels for free MPA-QDs with 2 hr of irradiation, but not for PONs-QDs (C). Further, the ROS levels of PONs-QDs depend on the PONs molecular structure. (N = 3 for panels A and B; N = 2 for panel C.)

**Figure 5.6:** *S. aureus* growth after incubation with  $6.25\text{--}100 \mu\text{g/mL}$  of free 55% (red), 75% (black), 95% (green), and 100% (blue) amine content PONs show that lower amine content PONs are more active than the higher amine content PONs (A). *S. aureus* growth when incubated with  $6.25\text{--}100 \mu\text{g/mL}$  PONs equivalents (corresponding to  $12.5\text{--}160 \text{ nM}$  QD equivalents, as determined by TGA) of PONs-QDs without irradiation show that these cells are not sensitive to PONs-QD conjugates (B). (N  $\geq$  3 biological replicates.)

**Figure 5.7:** *E. coli* growth after incubation with  $6.25\text{--}100 \mu\text{g/mL}$  of free 55% (red), 75% (black), 95% (green), and 100% (blue) amine content PONs show that lower amine content PONs are more active than the higher amine content PONs (A). *E. coli* growth when incubated with  $6.25\text{--}100 \mu\text{g/mL}$  PONs equivalents (corresponding to  $12.5\text{--}160 \text{ nM}$  QD equivalents, as determined by TGA) of PONs-QDs without (B) and with 2 hr irradiation (C) show that higher amine PONs-QDs have increased antibacterial activity compared to their respective free PONs. Lower amine content PONs have decreased activity once conjugated to QDs. (N  $\geq$  3 biological replicates.)

**Figure 5.8:** RBCs exposed to  $0.1\text{--}8000 \mu\text{g/mL}$  PONs equivalents of free PONs and PONs-QDs, the PONs-QDs (red) were found to have lower hemolytic activity than free PONs molecules (black). (N = 3 biological replicates.). \*Note:  $\text{HC}_{50}$  values for 95% and 100% amine PONs-CdTe QDs were not found within the tested concentration range, and are thus represented as bars to the highest tested concentration.

**Figure 5.9:** TGA analysis show that  $57 \pm 2\%$  of the peptide-QDs' mass was LL-37 peptides. (N=3)

**Figure 5.10:** Without irradiation, *E. coli* cells exposed to  $1.25\text{--}20 \mu\text{g/mL}$  LL-37 equivalents of the free LL-37 peptide (black) and peptide-QDs (red) show a concentration dependent decrease in growth (A). With 2 hr irradiation at the beginning of incubation, the peptide-QDs have irradiation enhanced activity, while the free peptides activity is maintained (B). The free LL-37 peptide and peptide-QDs had similar concentration dependent hemolytic activity at tested concentrations, with and without light activation (C). (N=3 biological replicates.)

## List of Schemes

### **Chapter 2**

**Scheme 2.1:** Hot injection synthesis of CdSe and CdSe/ZnS quantum dots.

**Scheme 2.2:** Microwave synthesis of CdTe quantum dots.

**Scheme 2.3:** Hot injection synthesis of ZnSe, ZnSe/ZnS, and Mn:ZnSe/ZnS quantum dots.

### **Chapter 3**

**Scheme 3.1:** Process of liposome lysis assay.

**Scheme 3.2:** Ligand exchange from TOP to DHLA-PEG750-OCH<sub>3</sub> coated QDs.

### **Chapter 4**

**Scheme 4.1:** Liquid culture and drop plate colony counting assay for *S. oneidensis* MR-1.

### **Chapter 5**

**Scheme 5.1:** Conjugation of poly(oxanorbornenes) and LL-37 peptides to CdTe quantum dots.

**Scheme 5.2:** Example 96 well plate layout for one biological replicate of the bacterial MIC assay. Note: Empty wells were filled with 200 uL of sterile water.

**Scheme 5.3:** Example 96 well plate layouts for one biological replicate of the hemolysis assay.

## Abbreviations

× g	Times gravity
° C	Degrees <u>C</u> elsius
λ	Wavelength
λ <sub>em</sub>	<u>E</u> mission wavelength
λ <sub>ex</sub>	<u>E</u> xcitation wavelength
τ	Average lifetime
τ <sub>x</sub>	Lifetime component <u>x</u>
μL	<u>M</u> icroliter
μM	<u>M</u> icromolar
μmol	<u>M</u> icromole(s)
aka	<u>A</u> lso <u>k</u> nown <u>a</u> s
AMP(s)	<u>A</u> nti <u>m</u> icrobial <u>p</u> eptide(s)
B.C.E.	<u>B</u> efore the <u>c</u> ommon <u>e</u> ra
BioTEM	<u>B</u> iological <u>t</u> ransmission <u>e</u> lectron <u>m</u> icroscopy
CdSe	<u>C</u> admium <u>s</u> elenide
CdTe	<u>C</u> admium <u>t</u> elluride
CFU(s)	<u>C</u> olony <u>f</u> orming <u>u</u> nit(s)
cm	<u>C</u> enti <u>m</u> eter(s)
DHLA-PEG	<u>D</u> i <u>h</u> ydro <u>l</u> ipoic <u>a</u> cid <u>p</u> oly <u>e</u> thylene glycol
DHLA-PEG-OCH <sub>3</sub>	<u>D</u> i <u>h</u> ydro <u>l</u> ipoic <u>a</u> cid <u>p</u> oly <u>e</u> thylene glycol methoxy
DLS	<u>D</u> ynamic <u>l</u> ight <u>s</u> cattering
<i>E. coli</i>	<u>E</u> sch <u>e</u> richia <u>c</u> oli
ESKAPE	<u>E</u> nterococcus <u>f</u> aecium, <u>S</u> taphylococcus <u>a</u> ureus, <u>K</u> lebsiella <u>p</u> neumoniae, <u>A</u> cinetobacter <u>b</u> aumannii, <u>P</u> seudomonas <u>a</u> eruginosa, and the <u>E</u> nterobacter species
eV(s)	<u>E</u> lectron <u>v</u> olt(s)
FRET	<u>F</u> örster <u>r</u> esonance <u>e</u> nergy <u>t</u> ransfer
FWHM	<u>F</u> ull <u>w</u> idth at <u>h</u> alf the <u>m</u> aximum
HC	<u>H</u> emolytic <u>c</u> oncentration
HEPES	4-(2- <u>h</u> ydroxy <u>e</u> thyl)-1- <u>p</u> iperazine <u>e</u> thane <u>s</u> ulfonic acid
hr	<u>H</u> our(s)
HRTEM	<u>H</u> igh <u>r</u> esolution <u>t</u> ransmission <u>e</u> lectron <u>m</u> icroscopy
kV	<u>K</u> ilo <u>v</u> olt(s)
ICP-MS	<u>I</u> nductively <u>c</u> oupled <u>p</u> lasma <u>m</u> ass <u>s</u> pectrometry

LL-37	A 37 amino acid cationic segment of the Cathelicidin peptide
M	<u>M</u> olar (g/mol)
MDR	<u>M</u> ulti <u>d</u> rug- <u>r</u> esistant
mg	<u>M</u> illigram(s)
MIC	<u>M</u> inimum <u>i</u> nhibitory <u>c</u> oncentration
min	<u>M</u> inute(s)
mL	<u>M</u> illi <u>l</u> iter(s)
ML	<u>M</u> ono <u>l</u> ayer(s)
mm	<u>M</u> illim <u>e</u> ter(s)
mM	<u>M</u> illimolar
mmol	<u>M</u> illimole(s)
Mn:	<u>M</u> anganese doped-
mol	<u>M</u> ole(s)
MPA	3- <u>m</u> ercap <u>t</u> rop <u>r</u> opionic <u>a</u> cid
MR-1	<i>S. oneidensis</i> 's <u>m</u> anganese <u>r</u> educing strain
MW	<u>M</u> olecular <u>w</u> eight
MWCO	<u>M</u> olecular <u>w</u> eight <u>c</u> ut <u>o</u> ff
NBD	<u>N</u> itro <u>b</u> enzoxa <u>d</u> iazole
ng	<u>N</u> anogram(s)
NIR	<u>N</u> ear <u>i</u> nfr <u>r</u> ed
nm	<u>N</u> ano <u>m</u> eter(s)
nM	<u>N</u> ano <u>m</u> olar
nsec	<u>N</u> ano <u>s</u> econd(s)
OD	<u>O</u> ptical <u>d</u> ensity
PEG	<u>P</u> oly <u>e</u> thylene glycol
Peptide	LL-37 <u>p</u> eptid <u>e</u> s
Peptide-QDs	LL-37 <u>p</u> eptid <u>e</u> -coated <u>Q</u> uantum <u>d</u> ots
pH	<u>P</u> otential of <u>h</u> ydrogen
PONs	<u>P</u> oly( <u>o</u> xan <u>o</u> rbornene)s
PONs-QDs	<u>P</u> oly( <u>o</u> xan <u>o</u> rbornene)s-coated <u>Q</u> uantum <u>d</u> ots
POPC	1- <u>p</u> almitoyl-2- <u>o</u> leoyl-glycero-3- <u>p</u> hos <u>h</u> ocholine
POPE	1- <u>p</u> almitoyl-2- <u>o</u> leoyl-sn-glycero-3- <u>p</u> hos <u>h</u> o <u>e</u> thanolamine
POPG	1- <u>p</u> almitoyl-2- <u>o</u> leoyl-sn-glycero-3- <u>p</u> hos <u>h</u> o-(1'-rac-glycerol)
ppb	<u>P</u> arts <u>p</u> er <u>b</u> illion
ppm	<u>P</u> arts <u>p</u> er <u>m</u> illion
psi	<u>P</u> ound per <u>s</u> quare <u>i</u> nc <u>h</u>

QD(s)	<u>Q</u> uantum <u>d</u> ot(s)
Qdot(s)	Purchased <u>q</u> uantum <u>d</u> ot(s)
RBC(s)	<u>R</u> ed <u>b</u> lood <u>c</u> ell(s)
Rhod	<u>R</u> hoda <u>m</u> ine
ROS	<u>R</u> eactive <u>o</u> xygen <u>s</u> pecies
rpm	<u>R</u> evolutions <u>p</u> er <u>m</u> inute
<i>S. aureus</i>	<u>S</u> taphylococcus <u>a</u> ureus
<i>S. oneidensis</i>	<u>S</u> hewanella <u>o</u> neidensis MR-1
sec	<u>S</u> econd(s)
S/TEM	<u>S</u> canning/ <u>t</u> ransmission <u>e</u> lectron <u>m</u> icroscopy
TEM	<u>T</u> ransmission <u>e</u> lectron <u>m</u> icroscopy
UV	<u>U</u> ltraviolet
UV/Vis	<u>U</u> ltraviolet- <u>v</u> isible
W	<u>W</u> att
wt	<u>W</u> eight/ <u>M</u> ass
ZnO	<u>Z</u> inc <u>o</u> xide
ZnS	<u>Z</u> inc <u>s</u> ulfide
ZnSe	<u>Z</u> inc <u>s</u> elenide

# Chapter 1: Introduction to the study of molecular interactions

between luminescent quantum dots and bacterial cells.

## 1.1 Luminescent Semiconductor Quantum Dots

Fundamental studies on luminescent semiconductor quantum dots (QDs) have continued since the initial discovery of QDs approximately 40 years ago.<sup>2</sup> These studies have been sustained by interest in QDs' unique photophysical properties, and the ability to manipulate these properties—with great precision—using relatively simple synthetic methods. The photophysical properties of QDs—including narrow size distribution, high quantum yield, and high absorptivity<sup>3-5</sup>—are the result of the quantum confinement effect. In quantum confinement, a material's excitons have their spatial motion restricted to discrete energy levels within the valence and conduction energy bands, rather than being free to move throughout the continuous energy bands that

are present in bulk materials (Figure 1.1). This effect is observed in QDs since their diameter—typically between 1-10 nm—is within the same size order

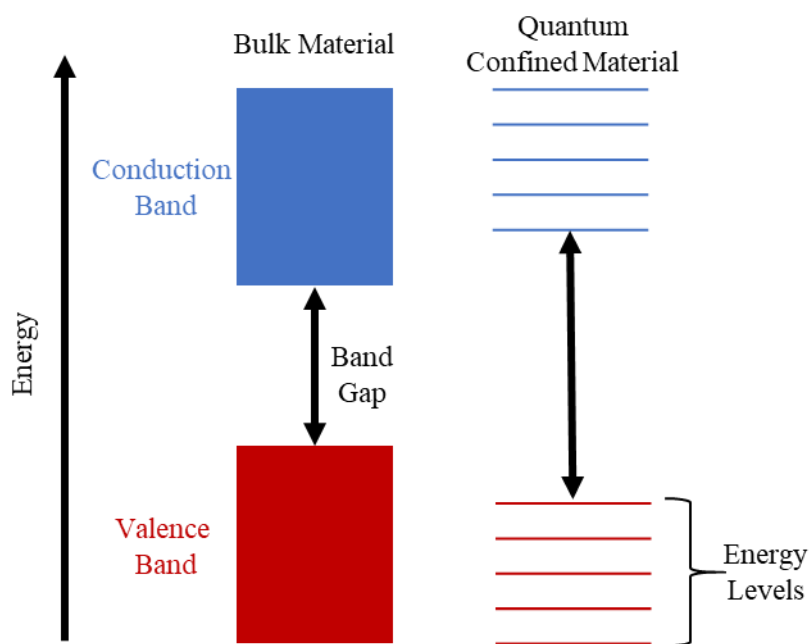


**Figure 1.1:** The quantum confinement effect on bulk energy bands.

as the distance between their conduction and valence bands (aka their energy band gap or Bohr exciton radius). The manipulation of QDs' photophysical properties starts by tightly controlling the synthesis conditions of the QD core to affect its material composition, band gap size, and wavelengths of absorption and emission.<sup>6-8</sup> Then, QD cores are often coated with higher energy band gap shells which can enhance their emission quantum yield and brightness due to improved surface-passivation, and with other surface modifying ligands that affect the QDs' miscibility and stability.

The unique, tunable photophysical properties of QDs have enabled their use in a broad array of technologies for computing<sup>9-11</sup>, energy harvesting<sup>12, 13</sup>, bioimaging<sup>14-16</sup>, cancer therapeutics<sup>17, 18</sup>, antimicrobial therapeutics<sup>19, 20</sup>, and other applications<sup>21-24</sup>. Each applied QD technology requires characterization of the QDs' photophysical properties and the potential interactions that the QDs may have with organisms relevant to the intended technology. Hence, there are several published investigations on how QDs interact with organisms when they are alone and when they are incorporated into specific technologies.<sup>15-17, 25-59</sup> These studies differ in their perspective of QD interactions depending on whether they find intended and/or unintended interactions between the QDs and organisms. Unfortunately, even though there is a plethora of these studies, there is a lack of harmonization between them which would allow scientists to consider and compare the available literature in order to broadly apply the findings to all QD technologies.

This dissertation is composed of molecular level studies on QD interactions with multiple cell models, which were systematically conducted in order that the

findings could be extrapolated to explain the potential environmental and human health implications of antibacterial QD technologies, specifically. Antibacterial QD technologies are under development as potential nontraditional antibacterial entities which may address the concerning rise in prevalence of drug-resistant bacteria. The literature on antibacterial QD technologies has demonstrated the clinical potential of these entities, but lacks a molecular level understanding of how these antibacterial QDs will interact with their targeted bacteria and the essential cells that they will encounter once applied as treatments or flushed from treated persons into the environment. This dissertation investigates the interactions between antibacterially-active QDs with potential bacterial targets, essential bacterial and human cells, and liposome models of these cells. Since these QDs are being investigated alone and conjugated to other antibacterial entities, what immediately follows is a brief discussion of the several antibacterial entities relevant to the scope of this work.

## **1.2 Account of Traditional Antibacterials: Metals and Small Molecule Antibiotics**

### 1.2.1 Interactions between Bacteria and Metals

The interactions between bacteria and metals are relevant to this dissertation since metal ion dissolution is one of the primary mechanisms of QD interactions.<sup>27, 32, 60-63</sup> Metals and bacteria have a complex relationship as some metals are essential for cellular functions, some metals are non-essential and non-cytotoxic, and other metals are non-essential and cytotoxic. Further, high concentrations of any metal, even if essential, can be harmful to bacterial cell homeostasis.<sup>64</sup> The essential metals for most bacteria include sodium (Na), magnesium (Mg), potassium (K), calcium (Ca), vanadium (V), chromium (Cr), manganese (Mn), iron (Fe), cobalt (Co), nickel (Ni),

copper (Cu), zinc (Zn), selenium (Se), and molybdenum (Mo).<sup>65-67</sup> They are deemed essential as they are required for regular physiological and functional processes—such as Mg’s role stabilizing the cell membrane through neutralizing phospholipid head groups outside the cytoplasm and the nucleotides in the cytoplasm<sup>68</sup>; Mn’s role in catalytic detoxification of reactive oxygen species (ROS) and lipid, protein, and carbohydrate metabolism<sup>67, 69</sup>; Fe’s role in electron transport chain reactions, DNA biosynthesis and hemoglobin’s ability to carry oxygen<sup>64, 69</sup>; Zn’s role in cell metabolism, virulence, gene expression, and general cellular metabolism<sup>67, 69</sup>; and Se’s role in anaerobic cellular respiration<sup>70, 71</sup>. The intercellular concentrations of essential metals are regulated by

dedicated transport proteins linked to intracellular sensing machinery, such as ATPases.<sup>66, 72</sup>

Non-essential metal uptake typically occurs via the same transport proteins, but can also occur through various passive biosorption mechanisms (Figure 1.2).<sup>66, 73, 74</sup> These routes of metal

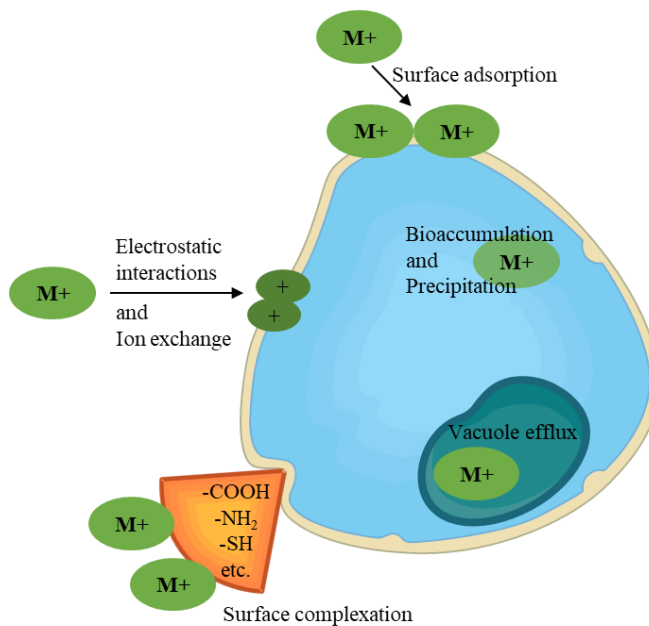


**Figure 1.2:** Biosorption mechanisms for metal uptake into bacteria.

metals to be used as homeostasis-disrupting antibacterial agents.

Metals with antibacterial activity have been found to act through several different mechanisms, which do not necessarily act exclusively. These mechanisms

include metals leading to protein dysfunction, antioxidant depletion, membrane impairment, nutrient uptake interference, and genotoxicity.<sup>66, 75-78</sup> Protein dysfunction and loss of enzyme activity has been observed with metals binding to inappropriate catalytic or structural binding sites, with improper metal binding in binding clusters, and with metal oxidation of any binding sites.<sup>66, 75</sup> The generation of ROS from metals has been linked to intercellular Fe and copper (Cu) Fenton chemistry leading to antioxidant depletion, and linked to the reduction of various metals which leads to thiol depletion.<sup>66, 76</sup> Metals have been proven to disrupt membrane potentials and cause membrane damage which leads to the interference of appropriate metal and nutrient transport across the membrane.<sup>66, 77</sup> And finally, genotoxicity is a downstream result of all of the above mechanisms' effect on the nucleic acid function and mutation rates of the cytotoxic metal-exposed bacterial cells.<sup>66, 78</sup> Further, the level of metal toxicity through these aforementioned mechanisms is dictated by the metals' donor atom selectivity, reduction potential, and speciation.<sup>66</sup> Donor atom selectivity dictates which molecules the metals interact with intracellularly, and to what degree. The reduction potential of metals speaks to their potential to affect the intracellular redox balance. The speciation of metals primarily influences their donor atom selectivity and reduction potential, but also affects metals' solubility and bioavailability.

The use of metals as antibacterial agents has been documented since antiquity and is undergoing a modern resurgence. Silver (Ag) and Cu have been used to preserve food and water, to sterilize wounds, and to treat ailments by Aztecs, Persians, Phoenicians, Greeks, Romans, and Egyptians since B.C.E times.<sup>66, 79-81</sup>

Additionally, Zn has been found in the medicinal storages of B.C.E. Roman ruins.<sup>82</sup> In modern times, other metals that have been investigated for their specific antibacterial activity include titanium (Ti), zirconium (Zr), tin (Sn), lead (Pb), bismuth (Bi), cadmium (Cd), tellurium (Te), Ni, and Mo.<sup>77, 82, 83</sup> Society now incorporates some proven antibacterial metals into clothing, foodware, plastics, ceramics, surgical steel, and other technologies in which it is important to prevent the growth of invasive bacterium and other microbes.<sup>66, 77, 83</sup> These technologies have been found to be especially important for the clinical, research, food preservation, and hospital industries. However, between the historical and the recent resurgent use of metal antibacterials, synthetic small molecule antibiotic developments decreased the focus on metals' antibacterial activity. The next section discusses the development and activity of these small molecules.

### 1.2.2 Interactions between Bacteria and Small Molecule Antibiotics

The interactions between bacteria and small molecule antibiotics are relevant to this dissertation since the nontraditional antibacterial agents used in this work were pursued due to antibiotics' ineffectiveness against resistant bacterial infections and were designed to act via similar antibacterial mechanisms. Like metals, small molecules have also been used to treat bacterial infections since antiquity; however, the use of the term 'antibiotic' and the onset of the modern era of small molecule antibiotic treatment is not marked until the 20<sup>th</sup> century. Antoine Béchamp (a late 19<sup>th</sup> century French scientist), Paul Ehrlich (a late 19<sup>th</sup> century German physician), the aforementioned ancient civilizations that used metal antibacterials, and several others are all known for using mold extracts, plant extracts, and other chemicals composed

of small molecules to treat bacterial infections.<sup>84</sup> The term ‘antibiotic’ was first used by Selman Waksman in 1941 to describe ‘small molecules with antimicrobial activity, which were isolated from other microbes’.<sup>85</sup> The term is now used to describe ‘any small molecule that antagonizes bacterial growth, no matter if the molecule was biologically or synthetically made’. The modern antibiotic era began with the discovery of the fungus-derived penicillin compound by Alexander Fleming in 1928. The development of and clinical research on penicillin—before its worldwide distribution started in 1945<sup>84</sup>—occurred during the “golden age” of antibiotic discovery, between the 1940s-1960s.<sup>86</sup> Most antibiotic classes still in use today were discovered during this time period. These antibiotics are primarily produced by and isolated from the actinomycetes family of soil bacteria.<sup>85</sup>

Small molecule antibiotics have varying synthetic routes, structures, and mechanisms of antibacterial action. Their synthesis typically involves enzymatically-driven (and post-translationally modified) modular biosynthesis from amino acids, fatty acids, and sugar building blocks.<sup>85</sup> However, some antibiotics have more unique building blocks that may also undergo modular biosynthesis, or be modified synthetically.<sup>85</sup> The microbial genes responsible for the biosynthesis of antibiotic molecules have evolved overtime, primarily, via horizontal gene transfer (definition: the movement of genetic material which is not from parent to offspring, but instead non-sexually between genomes).<sup>85</sup> This fact makes it difficult to track a clear lineage from the various antibiotic producing microbes to common ancestors, unless they were modified intentionally in a lab. Regardless—and depending on their molecular structure—historically and presently used antibiotics have all mostly targeted cell

membrane synthesis, nucleic acid metabolism, or ribosomes to combat bacterial growth.<sup>84, 86</sup> The common structures of antibiotics are used to divide them into classes. The most common classes include penicillins, cephalosporins, quinolones, sulfonamides, tetracyclines, and glycopeptides (Figure 1.3).

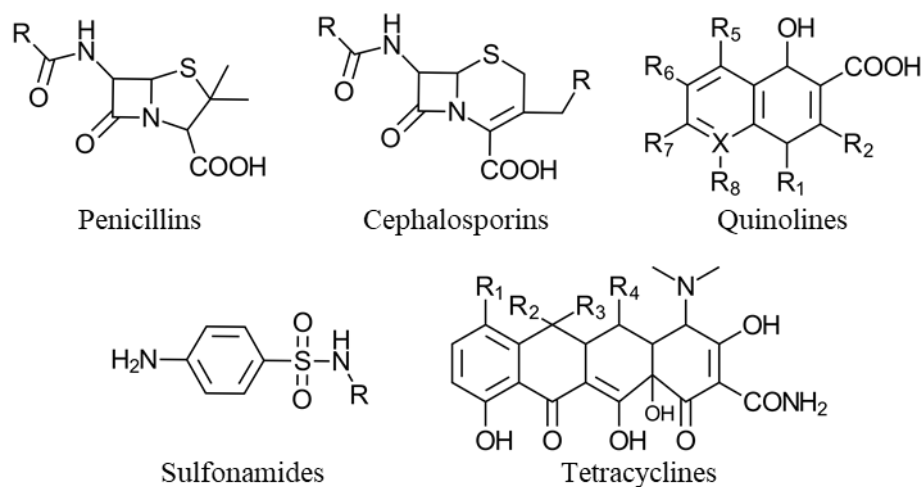


**Figure 1.3:** General structures of common small molecule antibiotic classes.

### 1.2.3 Antibiotic Resistance

Antibiotic resistance refers to a pathogenic bacterium's adaptation into a bacterium that can overcome the efforts of an antibiotic's mechanisms of action following initial, susceptible exposures to the antibiotic.<sup>19, 87, 88</sup> Bacteria have gained resistance by undergoing nucleic acid mutations, modifying their enzymes, modifying incoming drugs, pumping drugs out with efflux pumps, and undergoing horizontal gene transfer.<sup>84, 89</sup> For examples: 1) Nucleic amino acid substitutions in the gyrase enzymes and the 23S rRNA have resulted in bacterial resistance to fluoroquinolones and oxazolidinones, respectively.<sup>90, 91</sup> 2) Several *Enterobacter* species, *Pseudomonas aeruginosa*, and *Neisseria gonorrhoeae* infections produce extended-spectrum  $\beta$ -lactamases which open the  $\beta$ -lactam ring of the antibiotics that contain one (Figure

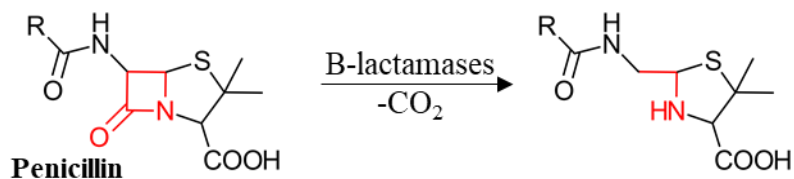


**Figure 1.4:**  $\beta$ -lactam antibiotics before and after inactivation by  $\beta$ -lactamases.

1.4), rendering the antibiotic inactive.<sup>19, 92, 93</sup> 3) Bacteria's N-acetyltransferases are their most common modifying enzymes, which can acetylate multiple sites on aminoglycoside antibiotics and prevent them from binding to target sites in bacteria.<sup>94</sup> 4) The small multidrug resistance family and the multidrug and toxic compound extrusion family of efflux transporters, in both gram-positive and gram-negative bacteria, use proton motive forces to rid of internalized antibiotics.<sup>95</sup> 5) Lastly, horizontal gene transfer is often considered the most important cause of resistance since it allows bacteria which have gained resistance by any of the aforementioned mechanisms to spread the adaptation information to other species.<sup>96, 97</sup>

Unfortunately, while scientists have noted resistance throughout the modern antibiotic era, they are now observing accelerating resistance rates and more multidrug-resistant (MDR) infections which are severely challenging the limited number of available antibiotics and the development of new ones.<sup>98</sup> The rate of small molecule antibiotic discovery significantly dropped in the 1970s.<sup>84, 86, 99</sup> And while society is still considered to be in the modern antibiotic era, no new classes of small molecule antibiotics—which are effective against the growing population of bacteria that are resistant to the currently available drugs—have been discovered or produced since the 1980s. Additionally concerning is the prevalence of hospital-acquired drug-resistant ESKAPE (*Enterococcus faecium*, *Staphylococcus aureus*, *Klebsiella pneumoniae*, *Acinetobacter baumannii*, *Pseudomonas aeruginosa*, and the

*Enterobacter* species) infections, which account for the majority of hospital-acquired infections in general.<sup>100, 101</sup> More than 15% of ESKAPE infections are MDR, which has owed hospital-acquired bacterial infections an estimated 6-10% death rate every year since 2002, globally.<sup>98, 101-104</sup>

As of December 2019, there were only 41 traditional small molecule antibiotics in the clinical development pipeline designed to target the top MDR bacterial threats to human health.<sup>105-107</sup> Current trends show that only 1 in 5 of these drug candidates will make it to market after clinical testing (Figure 1.5).<sup>86, 106, 107</sup> This small conversion rate is largely due to the high cost (about \$200 million per drug) associated with the clinical development and commercialization of these drugs, the occurrence of significant off-target toxicity discovered during clinical testing, and the development of bacterial drug resistance realized during and after clinical testing.<sup>86</sup> This conversion rate has only translated to 1 new antibiotic per year between 2004 and 2009, 2 antibiotics per year for 2011 to 2014, 5 in 2015, 2 in 2017, 3 in 2018, and 4 in 2019 being Food and Drug

Administration (FDA) approved for clinical treatment.<sup>86, 107, 108</sup> Most of these drugs target gram-positive bacteria since developing drugs against gram-negative bacteria has less commercial lucrativeness and more difficult technical challenges to overcome.<sup>98, 108</sup> The clinical testing-to-

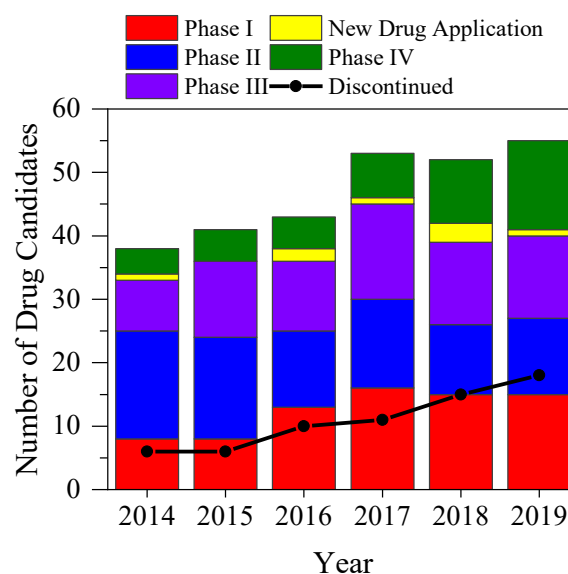


**Figure 1.5:** The number of drug candidates in various stages of the clinical pipeline between 2014 and 2019.<sup>84, 105</sup>

pipeline conversion rate and the number of available drug candidates are not competitive with the accelerating rate of bacteria's resistance development.<sup>98</sup> Further, some of the drug candidates that do make it to market are rendered obsolete very quickly; such as Daptomycin and Ceftazidime-avibactam which both had documented cases of drug-resistant bacteria within a year of their release for clinical use.<sup>88, 89</sup> The high cost, low rate of success, and possibility of a quick remission of success makes the development of antibacterial agents unappealing to drug-developing companies, which further limits the development of critical antibacterial agents.<sup>106</sup> There are last resort drugs available to treat most resistant bacterial infections. However, most last resort drugs are older, more toxic drugs that may resort in other patient health and compliance issues to overcome.<sup>98</sup> Further, scientists are increasingly observing MDR infections which are also resistant to the last resort drugs; such as with Colistin-resistant *Pseudomonas aeruginosa*, *Acinetobacter baumannii*, and *Enterobacter* species.<sup>98, 106, 109</sup> Overall, it appears that traditional antibiotic development and the current clinically-used drugs will not be able to keep up with the accelerating rates of bacterial drug resistance. Therefore, there is serious need to not only continue to improve upon the robustness of traditional antibacterial treatments' development, but to also research nontraditional antibacterial treatments.

### **1.3 Account of Nontraditional Antibacterials: Peptides, Polymers, and Nanoparticles**

The research, clinical, and political communities that are seeking to address the growing prevalence of MDR bacteria have recognized that fully understanding the mechanisms of action for effective natural and synthetic antibacterial treatments will improve on and inform the design of the next generation of antibacterial agents. To

this end, teams of researchers and clinicians are taking several approaches to define the specific mechanisms of action for different traditional antibacterial agents. With this information, the first move to combat the onset of MDR was to make antibiotic analogues (definition: compounds with modified structures of existing antibiotics, with components that bacteria had not yet evolved resistance for). For example, ceftaroline and ceftolozane are analogues of the ceftazidime antibiotic that, when paired with  $\beta$ -lactamase inhibitors, extends the effectiveness of cephalosporin antibiotics to drug-resistant ESKAPE bacteria (Figure 1.6).<sup>98, 110</sup> Now, scientists are also finding or designing nontraditional antibacterials that either 1) mimic the mechanisms of action of traditional antibacterials—while lacking the components that bacteria have developed resistance to—or that 2) work by completely different mechanisms. These nontraditional alternatives include bacteriophage, antibody, antimicrobial peptide, antimicrobial polymer, and nanoparticle formulations.<sup>84, 86</sup> This dissertation specifically elucidates interactions between bacteria and the latter three antibacterial agents—alone and as conjugates.

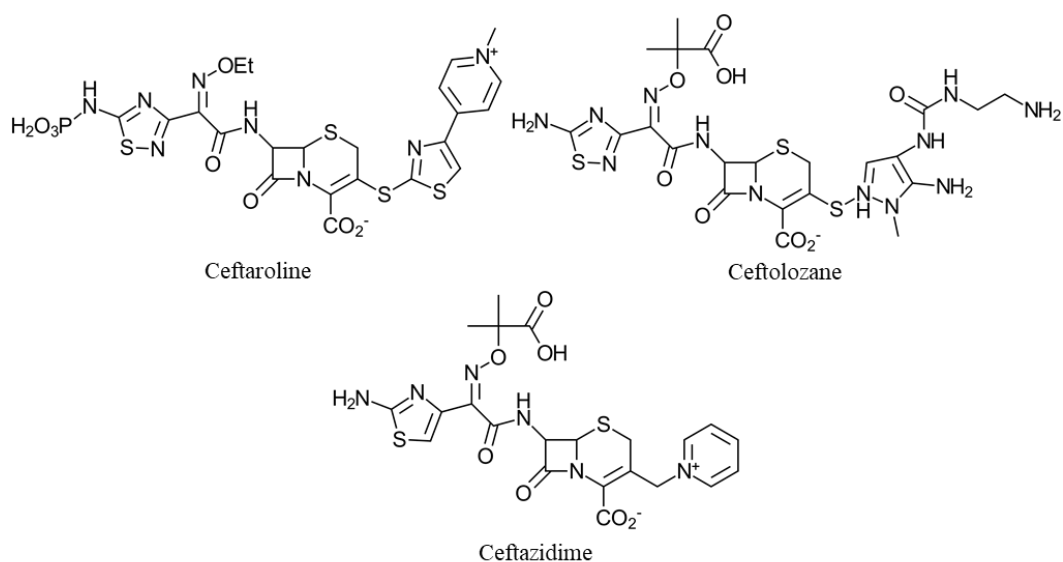


**Figure 1.6:** Molecular structures of ceftaroline and ceftolozane, antibiotic analogues of ceftazidime.

### 1.3.1 Interactions between Bacteria and Antimicrobial Peptides

The nearly 3,000 identified naturally-occurring antimicrobial peptides (AMPs) are nature's evolutionary combatants against bacterial, fungal, and protozoan pathogens.<sup>111-115</sup> Although there is great diversity in the genetic sequences of these AMPs, over 2,000 have been found to have antibacterial activity. The overall cationic nature of these antibacterial AMPs enables their binding to all bacterial membranes—since these membranes are negatively charged—through nonspecific electrostatic interactions.<sup>30, 113-115</sup> However, compositional differences between gram-negative and gram-positive bacterial membranes do require different AMP characteristics for maximum efficacy. AMPs with higher hydrophobicity and stronger pore-forming mechanisms are most effective against the more rigid, multilayer membranes of gram-positive bacteria. More hydrophilic AMPs that act through membrane-coating mechanisms are most effective against gram-negative bacteria. An additional benefit of antibacterial AMPs' cationic nature is that it prevents them from interacting with the predominately zwitterionic lipid-containing mammalian cell membranes.<sup>30, 113-118</sup> Additionally, mammalian membranes' cholesterols and other lipids result in membrane curvatures that inhibit antibacterial AMPs' binding. Under the right conditions, the lack of interaction between mammalian membranes and antibacterial AMPs minimizes the off-target toxicity of these AMPs and enables their use for treating bacterial infections in humans and animals.<sup>115</sup> Furthermore, another important fact is that bacterial adaptation and resistance development against AMPs is significantly lower compared to the rate of bacterial resistance development towards small molecule antibiotics.<sup>114</sup> This is likely due to the fact that the

interactions between AMPs and bacteria are nonspecific, but strong. The bacterial membrane would likely have to change its charge and structure in order to combat antibacterial AMPs' activity.<sup>30, 115</sup>

Several studies have aimed to elucidate the mechanisms of AMPs' antibacterial selectivity and activity. Summatively, it has been found that hydrophobic and electrostatic effects are responsible for orienting antibacterial AMPs amongst the phospholipids in bacterial membranes.<sup>118</sup> Once the affinity between specific AMP residues and bacterial phospholipids has led to binding, the membrane-bound AMPs enact numerous antibacterial interactions. These interactions have been described by several mechanistic models, of which the 'Shai-Matsuzaki-Huang' or 'carpet' model is the most prominent (Figure 1.7).<sup>113, 114</sup> In this model, electrostatic interactions lead to concentrated coatings of AMPs on bacteria's outer membrane (A).<sup>113, 114</sup> After binding to the membrane in high local concentration, the AMPs destabilize the membrane curvature by inserting their hydrophobic residues into the phospholipid layers (B).<sup>30, 113, 114, 118, 119</sup> Depending upon the AMPs' concentration and binding orientation and the lipid composition of the targeted membrane, the AMPs will then

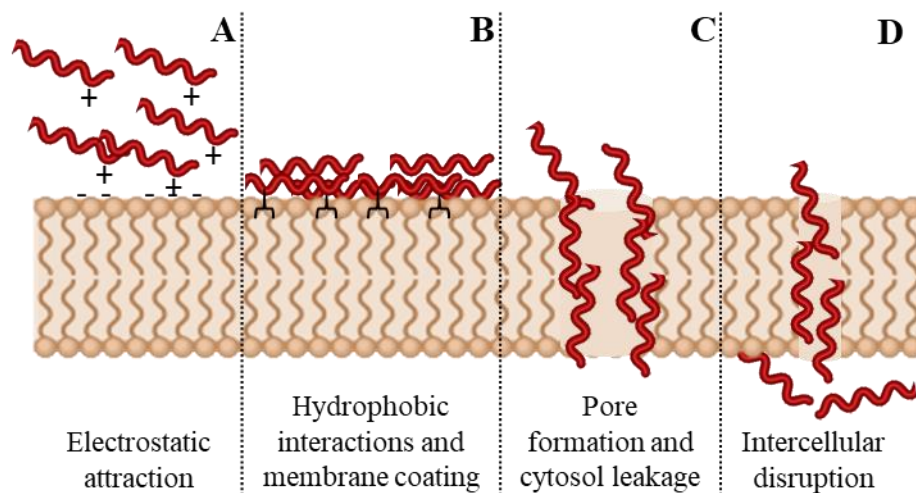


**Figure 1.7:** The 'Shai-Matsuzaki-Huang' or 'carpet' model explanation of antibacterial activity.

either form pores and cause cytosol leakage (C), and/or move to the inner membrane and cause intercellular damage (D).<sup>114, 118, 119</sup> Higher AMP concentrations often lead to the formation of stable pores.<sup>119</sup> Higher charge density AMPs stabilize the pores by forming anionic lipid domains, while more neutral AMPs stabilize the pores through hydrophobic residue insertion.<sup>118, 120</sup> The LL-37 peptide used in this research is a human-derived, cationic antibacterial AMP which uses the described carpet model to cause bacterial lysis.<sup>121</sup> It is commonly used in antimicrobial technologies designed to enhance wound healing or cancer treatments due to its selective membrane disruption activity against microbial organisms.<sup>122-126</sup> However, the limitations of LL-37 and several other AMPs—including their low natural potency, limited availability, and their susceptibility to enzymatic degradation by bacterial proteases<sup>111, 115</sup>—have led a number of research groups to develop synthetic mimics of AMPs in order to overcome these limitations. Synthetic polymer mimics of AMPs, specifically, are described in the following section.

### 1.3.2 Interactions between Bacteria and Antimicrobial Polymers

Synthetic polymer mimics of AMPs were developed to have the same bacterial cell selectivity and low human cell toxicity of AMPs, but even lower susceptibility to bacterial resistance development.<sup>115, 127</sup> One such mimic, a copolymer produced through the ring opening polymerization of two  $\beta$ -lactams, was found to have broad spectrum activity which: at low concentrations, binds to anionic phospholipid heads and creates anionic lipid domains which result in phase-boundary defects and bacterial membrane leaks; and at high concentrations, blocks the transport of essential solutes into bacteria's intermembrane space which effectively 'starves'

the bacteria.<sup>120, 128, 129</sup> This  $\beta$ -lactam copolymer binds selectively to lipopolysaccharides in the outer wall of gram-negative bacteria, and to lipoteichoic acids in the peptidoglycan layer of gram-positive bacteria.

This project uses the unique class of synthetic polymer mimics of AMPs derived from poly(oxanorbornenes) (PONs) which, like the LL-37 peptide, disrupt bacterial cell membranes following the carpet model (Figure 1.8). These poly(oxanorbornene)-

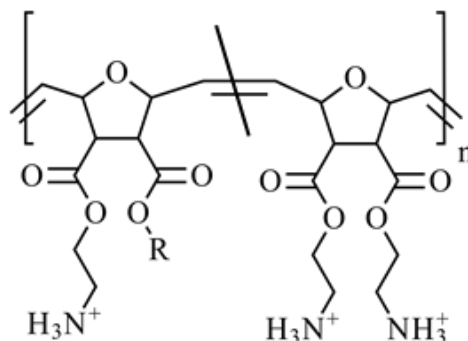


**figure 1.8:** Chemical structure of the poly(oxanorbornene) mimics of AMPs.<sup>115</sup>

derivatives show clear advantages over other polymer AMP mimics because of their unique monomer-level amphiphilicity, and the ability to further functionalize their backbone to affect their selectivity.<sup>115</sup> PONs often show an inverse relationship between their molecular weight and their antimicrobial activity, as larger-sized PONs have smaller membrane permeation ability.<sup>127</sup> This is important considering that gram-negative bacteria have a thin peptidoglycan layer between two fluid plasma membranes, while gram-positive bacteria have a thick peptidoglycan layer outside of a single plasma membrane which results in increased cell rigidity.<sup>120</sup> The increased rigidity of the membrane of gram-positive bacteria requires PONs to be of smaller molecular weights to be effective. Fortunately, the broad range of structural modifications that can be conducted on PONs—which the laboratory of Dr. Karen Lienkamp of the University of Freiburg has developed—has allowed tuning of the size, hydrophilicity, activity, and selectivity of the polymers. One class of PONs variations, the butyl PONs (R = butyl in Figure 1.8), has demonstrated effectiveness

against seven different strands of bacteria including *E. coli* and *S. aureus*, which are a part of the urgent threat ESKAPE list.<sup>115</sup>

Recently, there has been the development of polymer AMP mimics which exist at the intersection of polymer and nanoparticle antibacterial agents. One such mimic is the star-shaped structurally engineered antimicrobial peptide polymers (SNAPPs).<sup>130</sup> Unlike PONs, SNAPPs show inherent selectivity for MDR gram-negative over gram-positive bacterial cells.<sup>130</sup> The bactericidal mechanism of SNAPPs does not involve stabilized pore formation or aggregation. Rather, it involves disruption of bacterial membranes' ion influx/efflux pumps and charge potentials, which leads to “apoptotic-like” cell death. SNAPPs are structured in a star-shape in order to increase the local concentration of effective charges on their surfaces. This shape enhancing phenomenon has been documented in several polymer and nanoparticle antibacterial agents, and has been demonstrated to overcome the activity limitations of polymer AMP mimics.<sup>61, 131, 132</sup> A discussion of other antibacterial nanoparticles is in the following section.

### 1.3.3 Interactions between Bacteria and Nanoparticles

Antibacterial nanoparticles have been under development due to the inherent toxicity of some nanoparticle formulations, which can be tuned towards bacterial cell selectivity.<sup>19, 44, 133</sup> Metal nanoparticles have been shown to have tunable cytotoxic activity through ion interactions.<sup>61, 133</sup> For example, dissolved cationic silver nanoparticles have been found to have enhanced affinity towards negatively charged bacterial membranes—rather than zwitterionic, mammalian membranes—due to electrostatic forces, which allows them to more readily adhere to bacterial membranes

and then dissolve into  $\text{Ag}^+$  ions that disrupt intercellular structures and homeostasis, triggering bactericidal cell signaling.<sup>134-136</sup> Semiconducting nanoparticles have shown high inherent bioactivity through heavy metal interaction, free radical and oxidative damage, and membrane disruption mechanisms.<sup>26, 31, 61, 133</sup> Further, these mechanisms have proven to undergo light-activated enhancement in luminescent semiconductor QDs such as CdTe and CdSe.<sup>26, 137-139</sup> And to reiterate, nanoparticles that are composed of smaller antibacterial components—such as the SNAPP particles described above—have been shown to have enhanced antibacterial activity than their non-particle counterparts. Another example of this phenomenon is the self-assembled polymer nanoparticles of oxanorbornene-derivatives which have shown significant activity and increased therapeutic indexes against MDR bacteria.<sup>132</sup>

One of the most compelling arguments for utilizing nanoparticles in antibacterial treatments is the potential to use them as carriers for other antibacterial entities, allowing for the realization of possibly combinatory antibacterials. One advantage of using antibacterial nanoparticles as carriers is that the surface antibacterial could be a biomolecule, like an antibody or ligand, which is selective to specific bacterial receptors and would enhance treatment selectivity and activity for the intended target.<sup>31, 44, 140</sup> For example, functionalized thiol ligand mixtures—which were known to target bacterial membranes—have been coated around the surface of gold nanoparticles.<sup>140</sup> These thiol-gold nanoparticle conjugates reached bacterial membranes with increased selectivity and efficiency before they dissolved into antibacterial-active ions, resulting in more potent antibacterial nanoparticles at the location of the intended targets. A similar enhancement has been observed with

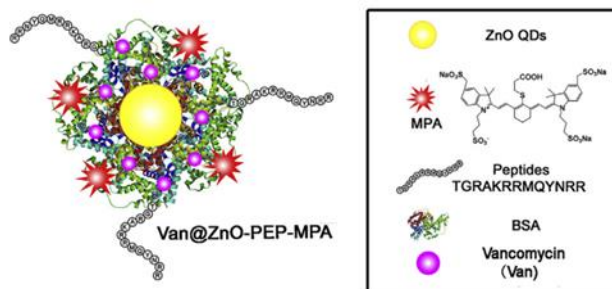
polyacrylate nanoparticles which were modified to carry penicillin.<sup>141</sup> The polyacrylate core increased penicillin's activity by enhancing the antibiotic's water solubility and improving its distribution to even penicillin-resistant bacteria in infected tissues. A second advantage of using nanoparticles as carriers is the increased local concentration of the surface antibacterial at the bacterial membrane, if several molecules of it are conjugated to and delivered via a nanoparticle carrier. For example, studies of cationic, cell-penetrating transactivator of transcription (TAT) peptides conjugated to cholesterol nanoparticles found an increase in the effective local charge density due to the presence of multiple TAT peptides around each nanoparticle.<sup>131</sup> This increased charge density was responsible for increased interactions between the peptides and bacterial membranes, compared to similar concentrations of free TAT peptides, thus resulting in higher bactericidal activity. A third advantage of nanoparticles as antibacterial carriers is the possibility to conjugate different types of antibacterials to each nanoparticle, and enhance their activity and lower their resistance development due to the possible targeting of multiple membrane functions. This concept was demonstrated in studies of Ag nanoparticles modified with multiple antibiotics.<sup>134</sup> These nanoparticles showed synergistic antibacterial activity against gram-negative and gram-positive bacteria, which was likely due to the surface antibiotics' membrane penetrating activity allowing an increase in the Ag nanoparticles' cell penetration and intercellular cytotoxic metal ion activity.

#### 1.3.4 Interactions between Bacteria and QD Conjugates

This dissertation specifically relates to the literature established potential of luminescent QD carriers, aka QD conjugates, to be used for enhanced activity against bacterial targets.<sup>25, 30, 31, 34, 38, 50, 52, 142</sup> Cadmium-based semiconductor materials are typically used in these QD technologies since they have superior optical properties in the visible to near-infrared wavelengths of light, which enables efficient light activation and *in vivo* tracking of antibacterial QD conjugate treatments.<sup>63, 143</sup> However, studies on the inherent activity of metals that may dissolve from these QDs and induce off-target activity have resulted in the development of both cadmium-containing and cadmium-free QD conjugate technologies.<sup>14, 17, 18, 144</sup> Regardless of the material, these QD conjugate technologies have been found to enhance the antibacterial activity of conjugated agents through the same nanoparticle-induced phenomena described in the previous section and through QDs' light enhancement capabilities, and to allow antibacterial treatments to be tracked via optical techniques.

Light-activated enhancement of antibacterial agents has been realized with several photosensitive agents, such as QDs, since light irradiation can be used to induce increased formations of homeostasis-disrupting ROS from the photosensitive agent.<sup>26, 37, 138, 145-147</sup> For example, studies investigating the light-activated enhancement of QDs' antibacterial activity have quantified multiple fold increases in the amount of superoxide and hydroxide (specific ROS) molecules uptaken by receptors on targeted bacteria after their incubation with irradiated QDs.<sup>26, 138</sup> While the work did find that the tested QDs were inherently toxic without irradiation—since their small size allowed them to move across membranes and disturb both sides of the

bacterial membrane—it further concluded that increased ROS generation, due to light irradiation, compounded the disruptions to bacterial cell homeostasis and the induced cell toxicity. Additionally, while such light enhancement has been realized with QDs alone, QDs conjugated to other antibacterial agents have shown a greater potential for significant light-enhanced activity. The polymyxin B-coated CdTe QDs are an antibiotic-QD conjugate example which has demonstrated light-exposure dependent, additive bactericide activity against gram-negative bacteria.<sup>50</sup> Only an irradiated 4.8 nM CdTe QDs dose of these conjugates, at a polymyxin-B:CdTe QDs conjugation ratio of 30:1, was necessary to invoke antibacterial effects. This is significantly smaller than the 300 nM of CdTe QD equivalents necessary for the QDs alone to have any antibacterial effects. The indolicidin-coated QDs are an AMP-QD conjugate example with demonstrated greater antibacterial activity (MIC = 5  $\mu$ M) than either entity alone (MICs = 10-25  $\mu$ M), and with broad spectrum efficacy.<sup>44</sup> The ZnO QDs conjugated to Ubiquicidin<sub>29-41</sub> (UBI<sub>29-41</sub>), vancomycin, and indocyanine green derivative (MPA) molecules are an example of a multifunctional antibacterial QD conjugate (Figure 1.9).<sup>25</sup> UBI<sub>29-41</sub> is an antibacterial AMP that allowed the QD conjugate to specifically target bacterial cells over mammalian cells. Vancomycin, a highly potent gram-positive selective antibiotic drug, was conjugated to the QDs in order to include multiple antibacterial entities into the conjugate, and gram-positive bacteria selectivity. MPA, an NIR-light emitting organic dye, **Figure 1.9:** The Van@ZnO-PEP-MPA antimicrobial probe.<sup>25</sup>



was conjugated to the QDs to enable *in vivo* imaging within the NIR I window. All of these components together resulted in a probe that could be specifically targeted to gram-positive bacterial cells, be excited to show real-time location of the probe through deep tissue, and enhance the treatment efficacy of Vancomycin alone by 22%.

Tracking QD conjugates has been realized by adding dyes—as exemplified in the ZnO QD conjugate—or by monitoring the inherent luminescent properties of the QDs.<sup>34, 40, 49, 52</sup> Monitoring the antibacterial QD conjugates allows scientists to locate them in infected tissues, to study their interactions with bacterial cell membranes, and to quantitatively assess their activity and selectivity.<sup>44</sup> Being able to monitor QD conjugates allows for accurate determination of where an antibacterial treatment is being delivered and how much of it to administer to a patient to completely eradicate an infection.

#### **1.4 Project Goals: Understanding the Interactions between Luminescent Semiconductor QDs and Bacteria at the Molecular Level**

The last few examples of antibacterial QD conjugates have illustrated the scientific community's recent approaches of conjugating multiple antibacterial agents into a single antibacterial entity, in efforts to develop promising solutions to combat the increasing occurrences of bacterial drug resistance. Due to the success of these and other works, there is continued interests in this potential. As was for the previous work, the future work behind these efforts will be supported by an understanding of the interactions between these antibacterial agents and their target and off-target organisms. Thus, investigations on these interactions will need to become more

robust and harmonize so that the clinical community can synthesize the information into reasoning for the next generation of antibacterial entities.

The main goal of this dissertation is to develop a molecular level understanding of the interactions between luminescent semiconductor QDs and cells that are relevant to human and environmental health. Human health cell models are necessary since this body of work is specifically investigating interactions that will inform the design of antibacterial agents, which will operate in systems filled with both pathogenic and essential cells. Environmental health cell models are necessary since antibacterial waste not only goes into the controlled containments of research and clinical facilities, but—after being flushed out of the body of a person who has used it—also ends up in wastewater and, ultimately, the environment. The differences between how human and environmental health bacteria interact with QDs of different material, size, surface ligand, and structure compositions are investigated since the proposed antibacterial QD conjugates of the literature have varying QD compositions. This project further aims to propose and investigate unique peptide- and polymer-coated luminescent QD conjugates with the potential to be potent antibacterials. We hypothesized that PONs-coated and LL-37-coated luminescent CdTe QDs would have synergistic activity from the combination of the light-enhanceable antibacterial activity of CdTe QDs with the antibacterial activity of the PONs and LL-37 coatings. Such a realization would result in highly potent antibacterial agents with the potential to be nontraditional treatments against drug-resistant pathogenic bacteria. Overall, this research provides fundamental information on how QDs' compositions affect their interactions with cells. This information supports the scientific community's

potential to develop new antibacterial agents and to reduce the number of urgent threat bacteria plaguing society.

## Chapter 2: Synthesis and Characterization of Luminescent Semiconductor Quantum Dots.

### 2.1 Purpose

This chapter discusses the preparation and characterization of the luminescent quantum dots—of varying semiconductor material and structural compositions—that were used in this dissertation and the publications it recapitulates.<sup>148, 149</sup> Additionally, this chapter begins to convey why the anti-membrane and anti-cellular activity of these specific quantum dot compositions were investigated in the remaining chapters.

### 2.2 Introduction

Cadmium-containing QDs, especially CdSe and CdTe QDs, are amongst the most widely used QDs due to their superb photophysical properties, the relatively simple synthetic methods used to make them (compared to synthetic methods for other QDs), and the ability to achieve a series of same material QDs which emit at different visible to near infrared wavelengths.<sup>63, 143</sup> These specifications have enabled the incorporation of cadmium-containing QDs into technologies for several applications; including in photocatalytic hydrogen production technology for enhanced photodriven charge separation<sup>150, 151</sup>, solar cell technology for increased energy harvesting efficiency<sup>12, 152, 153</sup>, light emitting and liquid optical display technology for enhanced visualization<sup>154, 155</sup>, and biosensing and bioimaging technology for improved stability and signaling<sup>15, 156, 157</sup>. However, concerns about the broad use of heavy metal-containing nanomaterials have limited the large-scale

development and use of QD technologies, and have led to investigations on the implications of these technologies.<sup>5, 145, 158</sup>

Studies that have specifically investigated the adverse effects of cadmium-containing QDs have attributed their toxicity to a combination of factors including QDs' ion dissolution, membrane association, and reactive oxygen species (ROS) generation (particularly when the QDs are irradiated with a UV light).<sup>61, 145</sup> Cadmium ion dissolution is often indicated as the main contributor to cadmium-containing QDs' toxicity.<sup>27, 32, 63, 159</sup> This is concerning considering that acute and chronic exposures to cadmium ions are known to have cytotoxic child and fetal development, neurological, hematological, gastrointestinal, and renal consequences.<sup>160</sup> Thus, cadmium-containing materials—including QD technologies—are regulated by government agencies worldwide. QD-membrane association, ROS generation, and other mechanisms of QD interaction have also been proven to negatively impact model membranes and living organisms.

The concerns about heavy metal-containing QDs have also stimulated efforts aimed to replace and/or contain these materials with alternative, biocompatible materials. Studies focused on material replacement have found that forming QDs from inert semiconductors results in QDs which are less toxic than their cadmium-containing counterparts.<sup>11, 39, 42, 43, 130, 161-164</sup> A few of these studies have specifically identified ZnSe QDs to be interchangeable, nontoxic alternatives to the widely-used CdSe QDs since they are structurally similar and prepared using similar synthetic methodologies.<sup>11, 43, 164</sup> Alternatively, several other studies have focused on coating heavy metal-containing QDs with surface passivating shells, such as an inert ZnS

shell<sup>41</sup>, or with ligands, such as polymers<sup>53</sup>, that can mitigate adverse interactions between the heavy metal-containing QDs and cells. Several of these studies have found that shells and ligands are capable of decreasing QD toxicity toward cells and living organisms by inhibiting ROS generation and ion dissolution.<sup>27, 29, 51, 53, 161</sup> However, other studies have revealed that coating QDs with passivating shells or mitigating ligands only delays adverse interactions between them and living organisms.<sup>17, 27, 41, 45, 47, 62, 63</sup> Summatively, while QD structural and compositional changes that may increase the biocompatibility of cadmium-containing QDs have been identified, the aforementioned studies have not fully determined which QD interactions change with these interventions.

This work uses a broad array of analytical techniques to investigate how material replacement, ZnS shelling, and surface ligand alteration affect the interactions between QDs and model organisms. Before the analytical techniques were used to study interactions, they were used to characterize each QDs' composition and photophysical properties. This chapter discusses the preparation and characterization of QDs with varying material and structural compositions. CdSe and CdTe QDs were investigated since they are commonly used QDs, and understanding their interactions with organisms is essential to the use of QD technologies. ZnSe QDs were investigated as they are often used as CdSe QD alternatives. ZnS-shelled CdSe and ZnSe core QDs are investigated to determine how shelling affects QD interactions. Later chapters will also include discussions on preparing and characterizing CdSe/ZnS and CdTe QDs with varying surface ligand compositions in order to investigate the affect that ligand composition has on QD interactions.

## 2.3 Materials and Instrumentation

### 2.3.1 Materials and Reagents

1-hexadecylamine (HDA, 90%), oleylamine (C18 content 80–90%), selenium powder (Se, 99.5%), and sodium hydroxide were purchased from Acros Organic. 1-dodecylphosphonic acid (DPA, 95%), manganese (II) chloride (MnSt, ultra dry), sodium tellurite, stearic acid (98%), zinc acetate, zinc formate (98%), and zinc stearate (ZnSt) were purchased from Alfa Aesar. Instrument Calibration Standard 2 (5% HNO<sub>3</sub>/ Tr. Tart. Acid/Tr. HF) for inductively coupled plasma mass spectrometry (ICP-MS) was purchased from Claritas PPT SPEX CertiPrep. 4-(2-hydroxyethyl)-1-piperazineethanesulfonic acid (HEPES) buffer (1 M), chloroform, methanol, nitric acid (Trace Metal grade), and toluene were purchased from Fisher Scientific. 1-Octadecene (ODE), 3-mercaptopropionic acid (MPA), cadmium acetylacetonate (CdAcAc, 99.9%), diphenyl phosphine (DPP), cadmium chloride (CdCl<sub>2</sub>), hexamethyldisilathiane ((TMS)<sub>2</sub>S, synthesis grade), LUDOX TMA colloidal silica (34 wt % suspension in H<sub>2</sub>O), sodium chloride, sodium citrate dihydrate sodium borohydride (Na<sub>2</sub>BH<sub>4</sub>), sodium phosphate monohydrate, sulfur powder, tetradecylphosphonic acid (97%), tetramethylammonium hydroxide solution (TMAH, 25 wt % in methanol), and trioctylphosphine (TOP, 97%) were purchased from Sigma-Aldrich. Qdot545 ITKTM carboxyl and amino (PEG) quantum dots were purchased from Invitrogen (a brand of Thermo Fisher Scientific corporation). Dihydro lipoic acid polyethylene glycol methoxy (DHLA-PEG750-OCH<sub>3</sub>) was prepared with slight modifications to a previously reported protocol.<sup>165, 166</sup>

### 2.3.2 Instrumentation

Characterizations were conducted in 1 cm pathlength cuvettes and chloroform, unless otherwise stated. Absorption spectra were obtained using a Thermo Scientific Evolution 201 UV/Vis spectrophotometer. Fluorescence spectroscopy measurements were performed using a PTI-Horiba QuantaMaster 400 fluorimeter, equipped with an integration sphere for emission quantum yield measurements and with a PicoMaster TCSPC detector for fluorescence lifetime measurements. A Molecular Devices SpectraMax M5 Microplate reader was used, in specific instances, to measure changes in fluorescence emission over time in 96 well plates. Hydrodynamic size and zeta potential were measured using the Malvern Zetasizer Nano ZS instrument. High-resolution transmission electron microscopy (HRTEM) images of QDs were obtained using a Titan 80–300 S/TEM, operating at 300 kV with a Gatan OneView imaging camera. For HRTEM imaging, QD samples were drop-coated onto mesh copper grids with ultrathin carbon film on holey carbon support film (Ted Pella, Inc.).

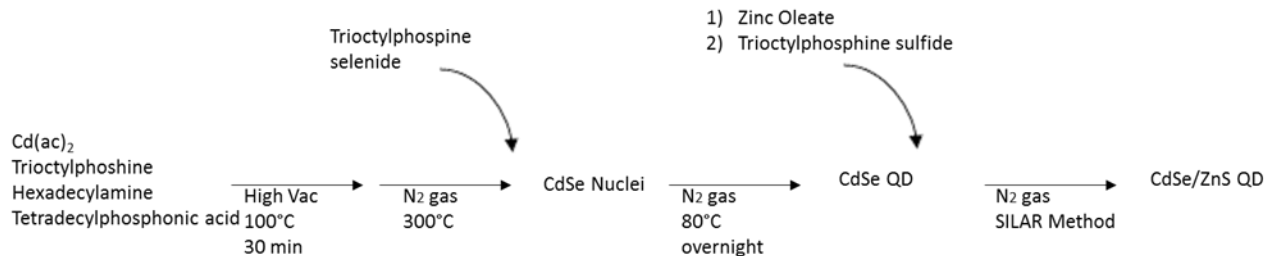
## **2.4 QD Synthesis and Characterization**

Cadmium-free and cadmium-containing QDs were either prepared in-house via the commonly used hot injection or microwave methods, or were purchased from Invitrogen. The hot injection method, which is widely used to produce organic colloids, typically involves a syringe injection of the anionic metal precursor into a round bottom flask containing the heated cationic metal precursor in surfactants (Appendix Figure 2.1A).<sup>167, 168</sup> The hot injection procedures used to produce the cadmium-containing and cadmium-free QDs varied only to accommodate the difference in the metal precursors' reactivities. The microwave method, widely used

to produce aqueous or gaseous colloids, uses dielectric heating (definition: heating as a result of the oscillation of electric and magnetic fields) to transform metal precursors into the desired QDs (Appendix Figure 2.1B).<sup>163, 167</sup> When conducted correctly, both methods of QD synthesis allow advantageous control of reaction time, temperature, and heat dispersion which results in the desired high crystallinity, narrow size distributions, high reproducibility, and high yields.<sup>167</sup>

#### 2.4.1 CdSe and CdSe/ZnS QDs' Synthesis and Characterization

CdSe QDs were synthesized using hot injection methods similar to a previously reported procedure (Scheme 2.1).<sup>2</sup> The cadmium precursor was prepared in a 50 mL three-neck round-bottom flask by stirring 1.0 mmol of CdAcAc into a solution containing 21 mmol of HDA, 2.1 mmol of tetradecylphosphonic acid, and 10 mL of TOP. This precursor was heated to 100 °C under inert nitrogen gas to fully dissolve the reactants, and then put under vacuum for 30 min to remove oxygen and water from the flask. The flask was backfilled with inert nitrogen gas, heated to 250 °C, cooled to 100 °C, and then put under vacuum again for at least 30 min (to ensure the complete removal of oxidants). Following this, the vessel was backfilled with nitrogen and then heated to 300 °C. Concurrent to the preparation of the cadmium precursor, a 5 mL selenium precursor solution of 0.84 M selenium powder in TOP was prepared under inert nitrogen gas. Once the cadmium precursor reached 300 °C, the selenium precursor was rapidly injected into the flask. The CdSe cores nucleated and grew instantly. Immediately after the hot injection, the reaction mixture was quickly cooled to 80 °C for overnight annealing. The resulting CdSe QDs were stored in the reaction mixture at room temperature and away from light until use.



**Scheme 2.1:** Hot injection synthesis of CdSe and CdSe/ZnS quantum dots.

CdSe/ZnS QDs with varying ZnS shell sizes were synthesized from these cores using successive ionic layer adsorption and reaction (SILAR) methods. SILAR calculation and shelling was performed following a previously described protocol, where 0.3 nm radius monolayers of a ZnS shell are added one at a time.<sup>3</sup> First, the CdSe cores were washed from their reaction mixture via centrifugation. Washing involved: 1) adding an equal amount of hexane to a portion of the cores' reaction mixture in a glass vial, 2) adding enough acetone to cause the mixture to go turbid, 3) centrifuging the cores into a pellet at  $2000 \times g$  for 5 minutes, 4) discarding the supernatant, 5) suspending the QD pellet in minimal hexane, and finally repeating steps 2-5 for at least 3 total cycles. The final QD pellet was suspended in chloroform, and analyzed via UV/Vis in order to determine the core size and concentration via published equations which relate the QDs' first excitonic peak location and intensity to their size and concentration in colloidal solutions.<sup>169</sup>

$$1.) \text{ CdSe Cores' Size: } D = (1.6122 \times 10^{-9})\lambda^4 - (2.6575 \times 10^{-6})\lambda^3 + (1.6242 \times 10^{-3})\lambda^2 - (0.4277)\lambda + 41.57$$

$$2.) \text{ CdSe Cores' Extinction Coefficient: } \varepsilon = 1600 \Delta E(D)^3$$

$$3.) \text{ Beers-Lambert Law for Molar Concentration: } C = A/\varepsilon L$$

In these equations:  $D$  is the calculated diameter (nm),  $\lambda$  is the measured location of the first exciton peak (nm),  $\varepsilon$  is the calculated extinction coefficient ( $M^{-1} \text{ cm}^{-1}$ ),  $\Delta E$  is

the measured location of the first exciton peak (eV), C is the calculated concentration (M), A is the measured absorbance intensity, and L is the known path length (cm). The washed CdSe cores were added to a solution containing 6 mL of ODE, 4 mL of TOP, 6 mL of oleylamine, and 40  $\mu$ moles of dodecylphosphonic acid in a 50 mL round-bottom flask under nitrogen gas. The solution was heated and kept at 100 °C under high vacuum for 30 minutes, to remove oxidants, before backfilling with nitrogen gas. Then, the first aliquot of zinc precursor (0.05 M zinc formate in oleylamine), which was calculated to add a 0.3 nm radius monolayer of a ZnS shell, was injected over 15 min. The reaction mixture was heated to 160 °C for the injection of a sulfur precursor (0.25 M (TMS)<sub>2</sub>S in TOP) aliquot over 15 min to form the first monolayer of ZnS shell. The QDs were then annealed at 160 °C for 20 min. If more ZnS shells were added, the reaction mixture was heated and kept at 180 °C, while the process of adding zinc and sulfur precursors over 15 min and annealing over 20 min was repeated until the desired ZnS shell thickness was realized. Once all shell

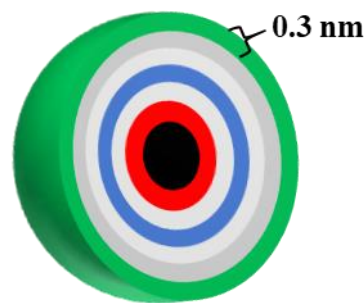


**Figure 2.1:** Representation of a CdSe core (black) with 1 (red), 3 (blue), and 6 (green) monolayers of a ZnS shell.

monolayers were added, the reaction mixture was heated to 200 °C while 0.5 mL of oleic acid was added dropwise. The core/shell QDs annealed at 200 °C for an hour. The reaction mixture was slowly cooled to room temperature, before storage at room temperature and away from light until use. CdSe with 1, 3, and 6 monolayers (ML) of ZnS shell were studied (Figure 2.1).

CdSe and CdSe/ZnS QDs' structural and photophysical properties were characterized while they were surrounded by organic ligands. Normalized absorption and emission spectra of CdSe and CdSe/ZnS QDs are shown in Figure 2.2. The absorption spectra show excitation peaks at 505 nm for CdSe core QDs and a red-shifted excitation peak about 564 nm for all CdSe/ZnS QDs. The emission spectra show corresponding emission peaks at 522 nm for CdSe core QDs and 594 nm for all CdSe/ZnS QDs, with full peak width at half-maximum (FWHM) values of 27, 31, 39, and 42 nm, respectively in order of increasing shell size. The FWHM gives an idea of the size distribution, and increases with increased polydispersity. HRTEM images, which also demonstrate the narrow size distributions of these QDs, can be found in Appendix Figure 2.2. The CdSe cores were  $3.9 \pm 0.5$  nm, CdSe/ZnS (1 ML) were  $4.2 \pm 0.8$  nm, CdSe/ZnS (3 ML) were  $5.0 \pm 0.9$  nm, and CdSe/ZnS (6 ML) were  $5.9 \pm 0.8$  nm in diameter. The emission quantum yields of the CdSe and CdSe/ZnS QDs were 13%,

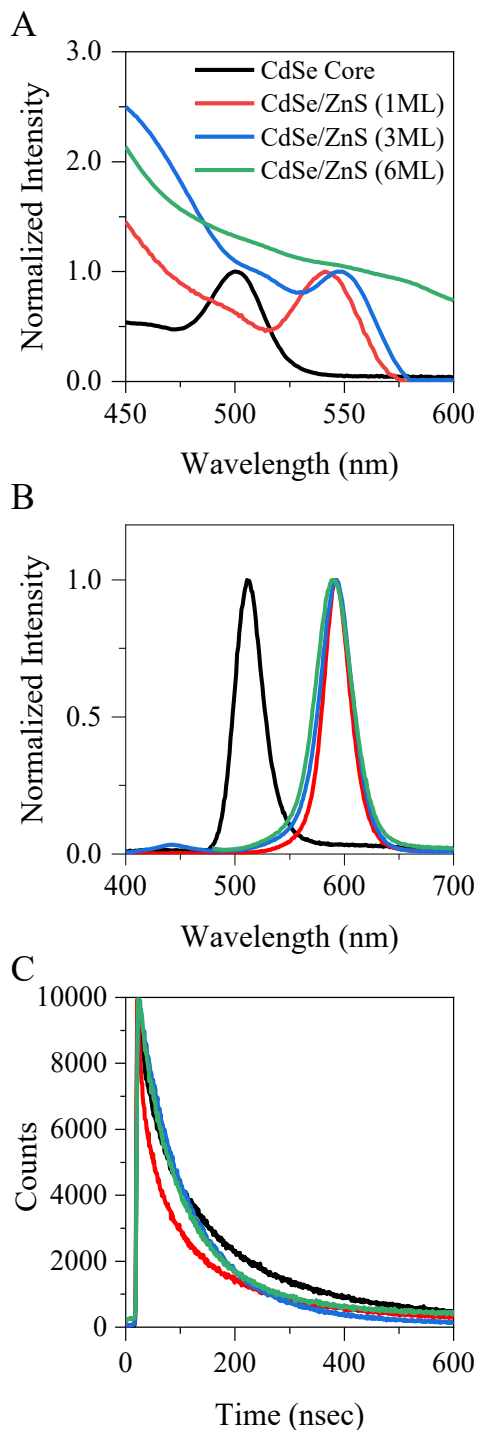


**Figure 2.2:** Normalized absorption (A), emission (B), and lifetime decay (C) spectra of CdSe and CdSe/ZnS QDs.

33%, 43%, and 70%, respectively; which demonstrates improved surface passivation and exciton recombination as the shell size increases. Time-resolved photoluminescence measurements were conducted and used to determine the impact of the ZnS shell on the cadmium-containing and cadmium-free QDs (Figure 2.2C). The fluorescence lifetime of the CdSe QDs was  $29.6 \pm 0.4$  nsec. As the CdSe cores were coated, the lifetime decreased to  $18.1 \pm 0.4$  nsec with 1 ML ZnS,  $23.8 \pm 0.3$  nsec with 3 ML ZnS, and  $22.4 \pm 0.2$  nsec with 6 ML ZnS. The decrease in fluorescence lifetime when core QDs are passivated with a higher-energy bandgap ZnS shell is attributed to increased exciton confinement to the QDs' core, and is consistent with previous studies.<sup>170</sup>

#### 2.4.2 Characterization of Purchased CdSe/ZnS QDs

Qdot545 ITK™ carboxyl- and amino-terminated polyethylene glycol coated CdSe/ZnS QDs (Qdots) were purchased from Invitrogen. Absorption, emission, and size spectra of the Qdots are shown in Figure 2.3. Figure 2.3A shows an excitation peak at 529 nm and an emission peak at 548 nm for both Qdots. DLS-measured number size distribution determined the hydrodynamic diameters to be  $14.05 \pm 3.9$

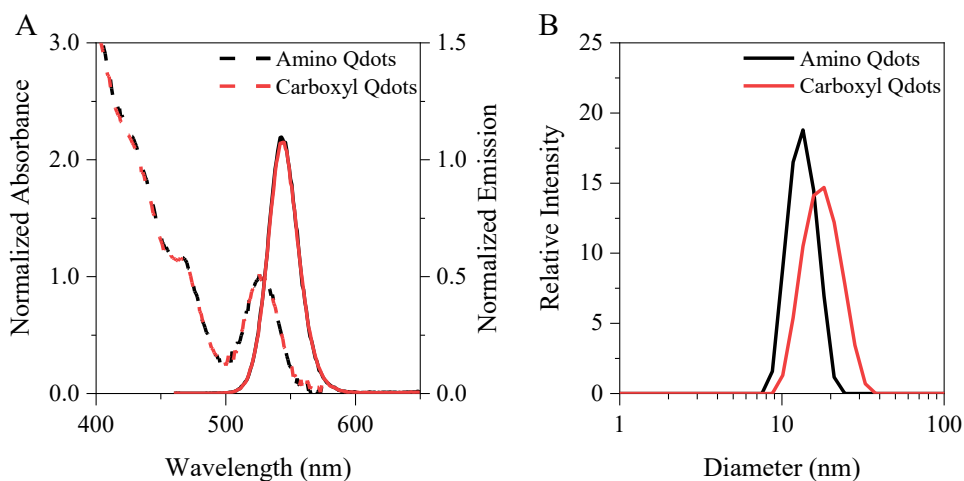
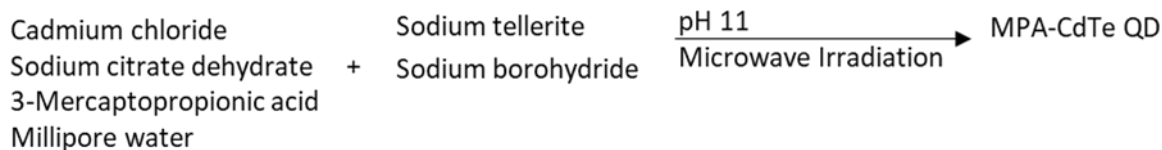


**Figure 2.3:** Normalized absorption (dotted) and emission spectra (solid)(A) and DLS analysis (B) of the Qdots.

nm for the amino-Qdots and  $11.38 \pm 1.8$  nm for the carboxyl-Qdots (Figure 2.3B). Zeta potential measurements revealed that the carboxyl Qdots had a  $-9.89 \pm 7.71$  mV potential and the amino Qdots had a  $-7.43 \pm 9.64$  mV potential in 2 mM HEPES buffer (pH = 7.4).



**Scheme 2.2:** Microwave synthesis of CdTe quantum dots.

### 2.4.3 CdTe QDs' Synthesis and Characterization

CdTe QDs were synthesized, using microwave methods similar to a previously reported procedure (Scheme 2.2).<sup>171</sup> In a 35 mL microwave vessel with a stir bar, 265  $\mu\text{mol}$   $\text{CdCl}_2$ , 340  $\mu\text{mol}$  sodium citrate dehydrate, 26  $\mu\text{L}$  of MPA, and 25 mL Millipore water were combined. The pH of this mixture was brought to 11 using 1 M NaOH. Then 50  $\mu\text{mol}$  of sodium tellurite and 500  $\mu\text{mol}$  of sodium borohydride were added. The vessel was capped and placed in a CEM Discover SP microwave synthesizer. The mixture was microwaved in Dynamic Mode at 100  $^\circ\text{C}$ , 250 psi, 300 W power, and high stirring for 10 min. The aqueous QDs were purified three times via centrifugation through a 30K MWCO centrifuge filter at  $2000 \times g$  for 5 min, and finally dispersed in pH 11 Millipore water. UV/Vis was used to determine the core size and concentration via the following literature reported equations which relate the QDs' first excitonic peak location and intensity to their size and concentration in colloidal solutions.<sup>169</sup>

- 1.) CdTe Cores' Size:  $D = (9.8127 \times 10^{-7})\lambda^3 - (1.7147 \times 10^{-3})\lambda^2 + (1.0064)\lambda - 194.84$

2.) CdTe Cores' Extinction Coefficient:  $\epsilon = 3450 \Delta E(D)^{2.4}$

3.) Beers-Lambert Law for Molar Concentration:  $C = A/\epsilon L$

In these equations:  $D$  is the calculated diameter (nm),  $\lambda$  is the measured location of the first exciton peak (nm),  $\epsilon$  is the calculated extinction coefficient ( $M^{-1} \text{ cm}^{-1}$ ),  $\Delta E$  is the measured location of the first exciton peak (eV),  $C$  is the calculated concentration (M),  $A$  is the measured absorbance intensity, and  $L$  is the known path length (cm).

The CdTe cores' structural and photophysical properties were characterized in pH 11 Millipore water. DLS, normalized UV/Vis absorption, and normalized emission spectra of the QDs are shown in Figure 2.4. Figure 2.4A illustrates the CdTe cores' excitation peak at 510 nm and the corresponding emission peak at 578 nm. Figure 2.4B shows the DLS-measured hydrodynamic number size distribution of the CdTe QDs to be  $5.0 \pm 1.5$  nm in diameter. Additionally, HRTEM and DLS size characterization of these QDs can be found in Appendix Figure 2.3.

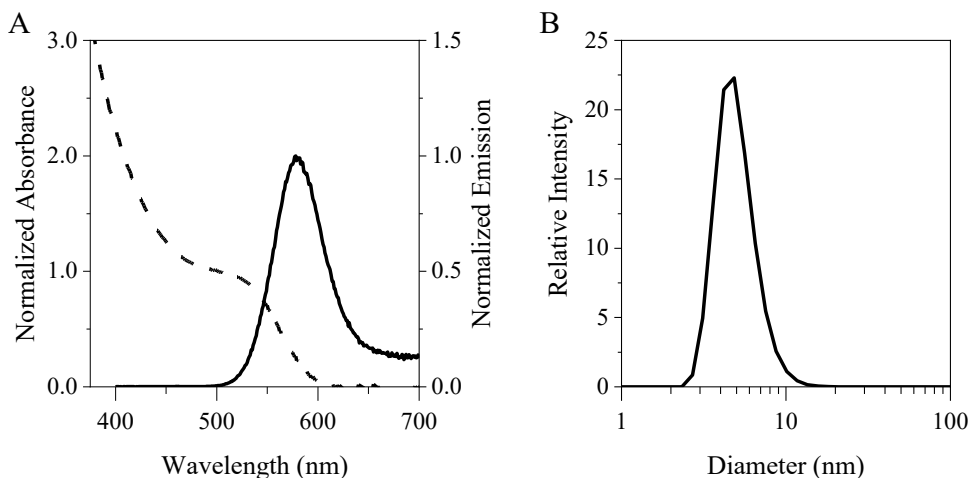
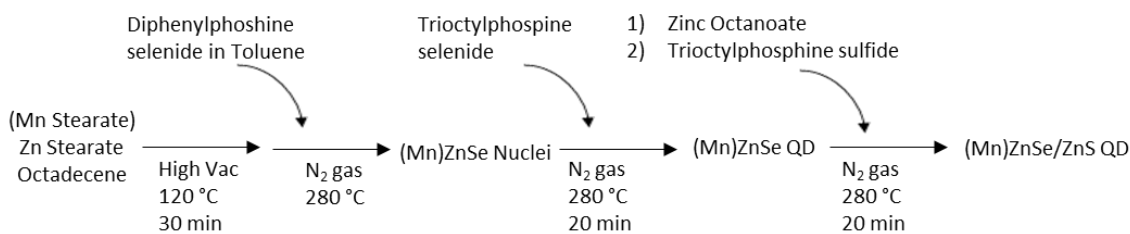


**Figure 2.4:** Normalized absorption (dotted) and emission spectra (solid) (A) and DLS analysis (B) of the CdTe QDs.

#### 2.4.4 ZnSe, ZnSe/ZnS, and Mn:ZnSe/ZnS QDs' Synthesis and Characterization

ZnSe and ZnSe/ZnS QDs were synthesized according to a previously reported procedure<sup>164</sup>, which was modified to also produce manganese-doped ZnSe/ZnS (Mn:ZnSe/ZnS) (Scheme 2.3). The reaction was performed in a 25 mL three-neck round-bottom flask under stirring. The zinc precursor solution was prepared in the round bottom flask by dissolving 1 mmol ZnSt powder in 5.0 mL of ODE at 120 °C under inert nitrogen gas. The three-neck flask was under vacuum for 30 minutes, and then backfilled with nitrogen gas while heating the solution to 280 °C. A selenium precursor solution was prepared by dissolving 100 μmol of selenium powder in a solution containing 17 μL of DPP and 670 μL of toluene. This selenium solution was injected rapidly into the zinc precursor solution and allowed to react for 5 min at 280 °C in order to nucleate ZnSe QDs. Then the flask was cooled to room temperature. A second selenium precursor solution was prepared by dissolving 1 mmol of selenium powder in 800 μL of TOP. This selenium precursor solution was injected into the reaction mixture at room temperature. The reaction mixture was heated and kept at 280 °C for 20 min to further grow the ZnSe cores, then cooled to room temperature. The formed ZnSe cores were immediately coated with a ZnS shell or stored in their reaction mixture at room temperature and away from light. To perform the ZnS



**Scheme 2.3:** Hot injection synthesis of ZnSe, ZnSe/ZnS, and Mn:ZnSe/ZnS quantum dots.

shelling, two precursor solutions were prepared: (1) 1 mmol of sulfur powder in 1 mL of TOP, and (2) 1.0 mmol of zinc stearate dissolved in 8 mL of ODE. The ZnS shell precursor solutions were injected into the reaction mixture at room temperature. The reaction mixture was then heated, kept at 280 °C for 20 min, and finally cooled to room temperature. The resulting ZnSe/ZnS QDs were stored in the reaction mixture at room temperature and away from light. Prior to their immediate future use, QDs were washed multiple times using the same purification methods for the synthesized cadmium-containing QDs, to remove excess reactants.

Manganese-doped ZnSe/ZnS (Mn:ZnSe/ZnS) were made since the bacterium used in Chapter 4 is known to reduce and metabolize Mn ions<sup>172</sup>, and Mn doping is often used to red shift the optical properties of ZnSe QDs.<sup>43, 173, 174</sup> These QDs were synthesized by adding manganese stearate to the reaction flask with the initial mass of zinc stearate. The total moles of zinc stearate and manganese stearate were equal to 1 mmol. Manganese stearate was made according to a previously reported procedure.<sup>173</sup> In a 50 mL flask, 10 mmol manganese chloride was dissolved in 20 mL methanol under nitrogen. In a 500 mL flask, 20 mmol stearic acid, 1.8 mL TMAH, and 100 mL methanol were stirred at 50 °C under nitrogen until dissolved. The manganese chloride solution is added to the stearic acid solution dropwise and allowed to stir for 20 minutes after all was added. The reaction forms a white precipitate which was filtered and washed with methanol at least 3 times, then dried overnight.

ZnSe, ZnSe/ZnS, and Mn:ZnSe/ZnS QDs' structural and photophysical properties were characterized while they were surrounded by organic ligands. Figure 2.5 shows the UV/Vis absorption, emission, and lifetime spectra of these QDs. The

UV/Vis absorption spectra show excitation peaks at 410, 402, and 402 nm for ZnSe, ZnSe/ZnS, and Mn:ZnSe/ZnS QDs respectively (Figure 2.5A). The emission spectra show corresponding emission peaks at 418 nm for ZnSe QDs, 423 nm for ZnSe/ZnS QDs, and 506 nm for Mn:ZnSe/ZnS QDs (Figure 2.5B). The emission quantum yields at the emission maxima were 5%, 10%, and 16%, respectively. The FWHM at the emission maxima were 17, 15, and 125 nm, respectively. The fluorescence lifetime of the Mn:ZnSe/ZnS QDs was  $15.1 \pm 1.4$  nsec (Figure 2.5C). The fluorescence lifetime of the ZnSe core QDs was  $7.4 \pm 0.3$  nsec. This value decreased to  $6.4 \pm 0.1$  nsec when the ZnSe cores were coated with a ZnS shell to form ZnSe/ZnS QDs, as expected from previous studies.<sup>170</sup> HRTEM images showing the narrow size distributions of these QDs can be found in Appendix Figures 2.4. The ZnSe core QDs were  $3.5 \pm 0.4$  nm in diameter, similar to the CdSe core QDs. The ZnSe/ZnS QDs were  $5.0 \pm 1.2$  nm in diameter, similar to the CdSe/ZnS(3 ML) QDs.

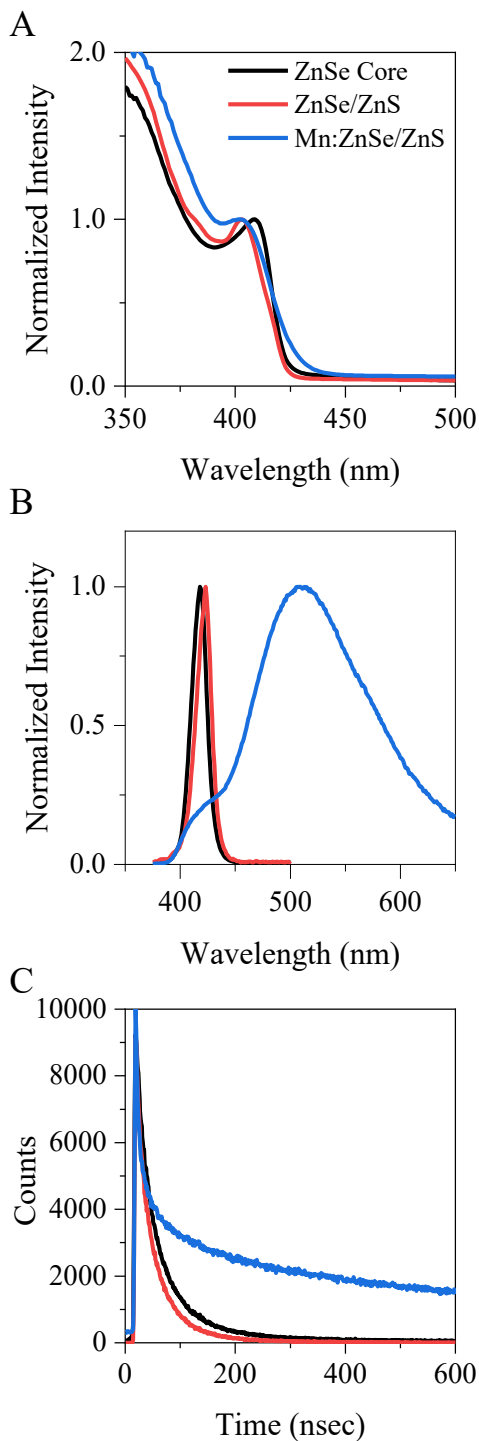


**Figure 2.5:** Normalized absorption (A), emission (B), and lifetime (C) spectra of ZnSe, ZnSe/ZnS, and Mn:ZnSe/ZnS QDs.

## 2.5 Conclusion

Not accounting for surface ligand variations, there are 9 different QD compositions used in this work (Figure 2.6). In Chapter 3, the activities of ZnSe and ZnSe/ZnS QDs are compared to that of the CdSe and CdSe/ZnS QDs, and the activities of Qdots with varying surface chemistries are compared using model liposome systems. In Chapter 4, the activities of ZnSe, ZnSe/ZnS and Mn:ZnSe/ZnS QDs are compared to that of CdSe and CdSe/ZnS QDs against an environmental health bacterial cell model. In Chapter 5, the activities of CdTe QDs with varying surface chemistry are investigated with human health-relevant bacterial and mammalian cell models. To reiterate, these QD compositions were chosen because of their current technological relevance and likelihood of interacting with the model systems being investigated.

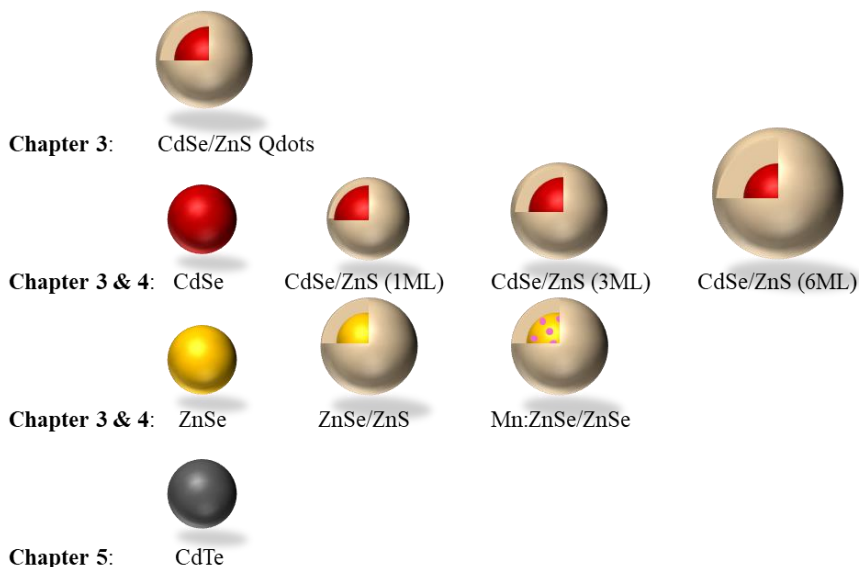


**Figure 2.6:** Representative image summary of QDs in this dissertation, by chapter.

## Chapter 3: Using liposomes to model mechanisms of interaction between quantum dots and cell membranes.

### 3.1 Purpose

This chapter discusses the preparation of liposomes (aka ‘lipid bilayer vesicles’ and ‘model membranes’), and investigates the interactions between them and QDs of different compositions. The goal was to use these model membranes to infer potential interactions between QDs and naturally occurring cell membranes. The liposomes were modified with free and lipid-tagged dyes in order that spectroscopic methods could be used to observe changes in the liposomes upon their interactions with QDs. Changes in the dyes’ fluorescent properties indicated specific interactions such as QD-liposome association, QD-induced lysis of the membranes, and ROS generation from the QDs. The QDs monitored for these interactions differed in semiconductor material, core or core/shell structure, ligand type, and surface charge.

### 3.2 Introduction

Several fluorescence techniques—including steady-state spectroscopy, time-resolved spectroscopy, confocal microscopy, epifluorescence microscopy, and single-molecule imaging—are used to study the interactions between nanomaterials and biological membranes. These techniques allow investigators to use the inherent environment-sensitivity of the fluorescence phenomenon and the wide availability of fluorophores to monitor membranes with superior spatiotemporal resolution.<sup>175, 176</sup> Hence, naturally occurring and synthetic lipid membranes are often labeled with fluorophores in order to study the interactions between them and nanomaterials.

This work uses fluorescently labeled liposomes—designed to be simple mimics of naturally occurring lipid membranes—to study QD-membrane interactions. Unlike naturally occurring membranes, these simple synthetic liposomes do not perform active mechanisms that may complicate the analysis of how a nanomaterial inherently acts with a biological membrane. Therefore, differences in the observed fluorescence-indicated interactions between the QDs and liposomes can only be attributed to differences in the QD and liposome compositions used in our assays. The QDs used differed in size, shape, and surface chemistry; which resulted in dissimilar rates of ion dissolution, reactive oxygen species (ROS) generation, and other key mechanisms of QD interactions with liposomal membranes. The liposomes used differed in bilayer components (Appendix Figure 3.1) and in which of the following fluorescent molecules were added to probe the mechanisms of QD interactions: calcein, nitrobenzoxadiazole (NBD), or rhodamine (rhod). Self-quenching calcein molecules were encapsulated in the internal hydrophilic space of liposomes to probe levels of membrane disruption. Lipid-tagged NBD molecules were used to probe changes in polarity and levels of ROS activity at the membrane. Lipid-tagged rhod molecules were used to probe rates of association between QDs and liposomes. Importantly, using liposomes with only one type of fluorescent molecule at a time allowed us to investigate each mechanism independent of the others, so that conclusions may be drawn relating variations in QD compositions to specific changes in their mechanisms of interaction with membranes.

We hypothesized that different levels of interaction would occur between the varying QD compositions and varying liposome compositions. Cadmium-containing

and cadmium-free core QDs were expected to demonstrate similar levels of membrane disruption activity, since the liposomes used to test this were simple models lacking metal specific receptors. ZnS-shelled QDs were expected to have less membrane disruption activity than the bare core QDs, since shelling has been proven to enhance QD stability and to prevent the ion dissolution which enhances QDs' membrane disruption activity. Considering electrostatic forces, the QDs with positively charged surface ligands were expected to have significant association with negatively charged membrane models; while the negatively charged QDs were expected to be repulsed. Also, we expected moderate attraction between QD-liposome systems where one entity had neutral/zwitterionic-terminations and the other was charged. Finally, due to the lack of direct QD irradiation in these studies, insignificant amounts of QD ROS generation was expected from all QD compositions.

### **3.3 Materials, Instrumentation, and Methods**

#### 3.3.1 Materials and Reagents

Sodium hydroxide was purchased from Acros Organic 1,2-dioleoyl-sn-glycero-3-ethylphosphocholine (chloride salt) (EPC), 1,2-dioleoyl-sn-glycero-3-phosphoethanolamine-N-(7-nitro-2-1,3-benzoxadiazol-4-yl) (ammonium salt) (NBD-POPE), 1,2-dioleoyl-sn-glycero-3-phosphoethanolamine-N-(lissamine rhodamine B sulfonyl) (ammonium salt) (rhod-POPE), 1-palmitoyl-2-oleoyl-sn-glycero-3-phosphocholine (POPC), and 1-palmitoyl-2-oleoyl-sn-glycero-3-phospho-(1'-rac-glycerol)(sodium salt) (POPG) were purchased from Avanti Polar Lipids. Instrument Calibration Standard 2 (5% HNO<sub>3</sub>/ Tr. Tart. Acid/Tr. HF) for inductively coupled

plasma mass spectrometry (ICP-MS) was purchased from Claritas PPT SPEX CertiPrep. 4-(2-hydroxyethyl)-1-piperazineethanesulfonic acid (HEPES) buffer (1 M), borate buffer (20X), chloroform, methanol, nitric acid (Trace Metal grade), toluene, and zinc chloride (97%) were purchased from Fisher Scientific. 0.45  $\mu\text{m}$  surfactant-free cellulose acetate (SFCA) membrane syringe filters, cadmium chloride, calcein disodium salt (calcein) was purchased from Fluka. LUDOX TMA colloidal silica (34 wt% suspension in  $\text{H}_2\text{O}$ ), Sepharose® CL-4B, sodium chloride, sodium selenite, and Triton X-100 were purchased from Sigma-Aldrich. Dihydro lipoic acid polyethylene glycol methoxy (DHLLA-PEG750-OCH<sub>3</sub>) was prepared and purified with slight modifications to a previously reported protocol.<sup>165, 166</sup>

### 3.3.2 Instrumentation

An Avanti Mini Extruder was used to extrude all liposomes. UV/Vis absorption spectra were obtained using a Thermo Scientific Evolution 201 UV/Vis spectrophotometer. Fluorescence spectroscopy measurements were performed using a PTI-Horiba QuantaMaster 400 fluorimeter, equipped with an integration sphere for emission quantum yield measurements and with a PicoMaster Time-correlated Single Photon Counting (TCSPC) detector for fluorescence lifetime measurements. A Molecular Devices SpectraMax M5 Microplate reader was also used, in certain instances, to measure changes in absorbance and fluorescence intensity over time. QD concentration in mass/volume units was measured using a PerkinElmer NexION 300D single quadrupole mass spectrometer. Hydrodynamic size and zeta potential were measured using the Malvern Zetasizer Nano ZS instrument. High-resolution transmission electron microscopy (HRTEM) images of QDs were obtained using a

Titan 80–300 S/TEM, operating at 300 kV with a Gatan OneView imaging camera. QD samples were drop-coated onto mesh copper grids with ultrathin carbon film on holey carbon support film (Ted Pella, Inc.) at least a day before analysis.

### 3.3.3 QDs' DHLA-PEG750-OCH<sub>3</sub> Ligand Exchange

Cadmium-containing and cadmium-free QDs, synthesized as described in Chapter 2, underwent a ligand exchange process to coat them with DHLA-PEG750-OCH<sub>3</sub> (MW = 927 g/mol) ligands according to a previously reported procedure.<sup>8</sup> The DHLA-PEG750-OCH<sub>3</sub> ligand (0.25 mmol), 0.5 mmol of sodium hydroxide, 0.13 mmol of zinc acetate, and 1 mL of methanol were sonicated together in a septum-closed vial filled under nitrogen gas. Purified QDs (10 nmol) were suspended in a minimal amount of chloroform, dried under vacuum, and put under a flow of nitrogen. The DHLA ligand solution was added to the QD solution and then left overnight at 50 °C under nitrogen gas. On the next day, 1 mL of ethyl acetate and enough hexane to separate the solvents into two distinct layers were added to the QDs, stirred, and allowed to separate. The hexane layer was removed to waste. QDs in the ethyl acetate layer were dried under vacuum and then dispersed in Millipore water. The QD solution was passed through a 0.45 μm SFCA syringe filter into a 30,000 molecular weight cutoff (MWCO) spin filtration device. In the filtration device, the QDs were washed using centrifugation cycles at 2,000 × g for 5 min at room temperature.

### 3.3.4 Inductively Coupled Plasma Mass Spectrometry

Inductively coupled plasma mass spectrometry (ICP-MS) measurements of QD samples were performed using a PerkinElmer NexION 300D single quadrupole

mass spectrometer. Instrument Calibration Standard 2 was used to prepare calibration curves from 0.1 ppb to 1 ppm for the different ion analytes—cadmium, selenium, zinc—which could be generated if the QDs dissolved. (Sulfur could not be detected by the instrument used.) There were 3 different sample types relevant to this chapter, and their preparation for ICP-MS analysis was as follows. Sample Type 1-QDs in organic solvents: QD samples at predetermined molar concentrations in chloroform were put into scintillation vials containing acetone and centrifuged to precipitate out the QDs. After allowing the QDs to dry, nitric acid was added to dissolve the samples, and then Millipore water was added to the QD-nitric acid mixtures to dilute the nitric acid concentration to 2% by volume and a total sample volume of at least 5 mL. Sample Type 2-QDs in aqueous solution: QD samples of predetermined concentrations were dissolved by adding nitric acid to the solutions. These aqueous QD solutions were kept at room temperature overnight. The next day, Millipore water was added to the QD-nitric acid mixtures to dilute the nitric acid concentration to 2% by volume and a total sample volume of at least 5 mL. Sample Type 3-QDs in dissolution investigations: QD solutions of known concentrations were centrifuged through 30,000 MWCO spin filtration devices at  $2,000 \times g$ . Large QD particles were trapped by the filter and the supernatants were analyzed for dissolved ion content.

### 3.3.5 Preparation of Calcein-Containing Liposomes

10:1 molar POPC:POPG liposomes, a phospholipid composition that models cell membranes of some gram-negative bacteria, filled with calcein dye were prepared via a dehydration/rehydration method.<sup>177</sup> These calcein-containing liposomes were prepared by stirring 65  $\mu\text{mol}$  of POPC and 6.5  $\mu\text{mol}$  of POPG in

chloroform together in a 500 mL round-bottom flask, under nitrogen gas, to create a dry phospholipid film. The flask was vacuumed overnight to remove all organic solvent. A stock solution containing 5 mM calcein disodium salt in 2 mM HEPES and 25 mM sodium chloride at pH 7.4 was prepared. A 3 mL aliquot of the calcein solution was added to the dried lipid film to self-assemble liposomes through hydration. The flask was immersed in a dry ice/acetone bath, until the solid film began to dissociate from the bottom of the flask. The flask was then placed in a water bath at room temperature to re-form the liposomes. This process was repeated 10 times to ensure dye encapsulation in the liposomes. One mL at a time, the liposome solution was extruded 15 times through an Avanti Polar Lipids mini extruder with a 50 nm pore polycarbonate membrane. The liposome sample was then run through a Sepharose CL-4B silica column (10 mm × 100 mm) with free HEPES buffer to remove free fluorophore molecules from the dye-containing liposomes.

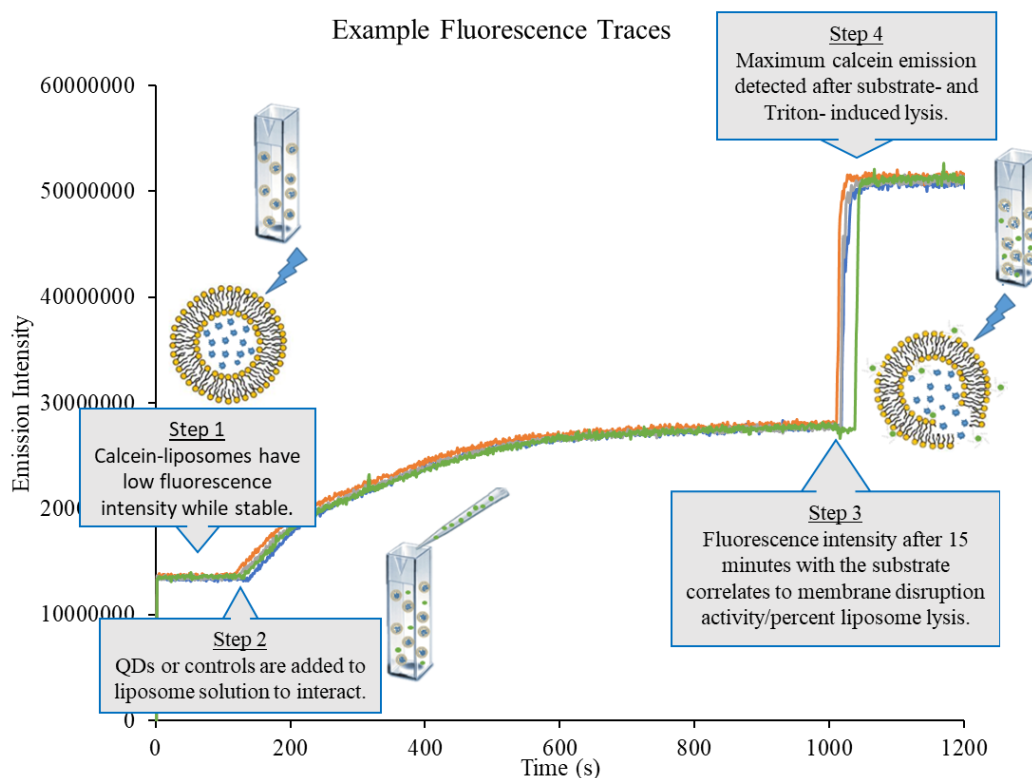
### 3.3.6 Preparation of Dye-Free Liposomes

10:1 molar POPC:POPG dye-free liposomes were prepared via the same methods, with the exception that phospholipids dried overnight were hydrated with 3 mL of 2 mM HEPES and 25 mM sodium chloride solution (with no calcein dye) at pH 7.4, followed by dehydration/ rehydration and extrusion. These were used as dye-free controls in the liposome lysis assays.

### 3.3.7 Liposomes Lysis Assays

Liposome lysis studies were observed using the ‘Timebased’ function of the FelixGX software used with the PTI-Horiba QuantaMaster 400 fluorimeter. Using this function, the fluorescence of the calcein-containing liposomes was continuously

measured for 20 minutes total with each test sample (Scheme 3.1): 1–2 min to determine the background fluorescence of liposomes (Step 1), 15 min for the substrate to interact with liposomes (Steps 2-3), 2–3 min for maximum liposome lysis to be determined after a 40  $\mu$ L injection of 1% Triton X-100 in Millipore water (Step 4). The excitation wavelength was set to 480 nm, the absorbance maximum of the dye. The emission of calcein was observed at 515 nm, the emission maximum of the dye. Within the window of background fluorescence observation, we see minimal fluorescence intensity since loading the liposomes with 10 mM calcein resulted in the self-quenching of the calcein molecules so long as the membranes remained stable. Membrane disruption of the liposomes—caused by either the QDs, controls, or Triton X—led to the release and dilution of calcein in the sample solutions, which in turn led to an increase in observed calcein fluorescence.



**Scheme 3.1:** Process of liposome lysis assay.

### 3.3.8 Preparation of Nitrobenzoxadiazole(NBD)-Labeled Liposomes

10:1:0.1 molar POPC:POPG:NBD-POPE liposomes were prepared for an approximately 1% mol ratio of labeled to unlabeled lipids, using methods similar to previously published procedures.<sup>178</sup> In a 250 mL round-bottom flask, 13  $\mu$ mol of POPC, 1.3  $\mu$ mol of POPG, and 0.11  $\mu$ mol of NBD-POPE in chloroform were stirred together under nitrogen gas to create a dry phospholipid film. The flask was vacuumed overnight to remove all organic solvent. The next day, 7.5 mL of 2 mM HEPES buffer (with 25 mM sodium chloride at pH 7.4) was used to hydrate the lipids to a 2 mM lipid concentration. The flask was taken through 10 freeze/thaw cycles. Finally, 1 mL at a time, the liposome solution was extruded 15 times through an Avanti Polar Lipids mini extruder with a 50 nm pore polycarbonate membrane.

### 3.3.9 Fluorescence Lifetime Assays of NBD-Labeled Liposomes

NBD-labeled liposomes' steady-state fluorescence was observed between 495 to 650 nm, with the excitation wavelength set to 470 nm. The fluorescence lifetime of NBD was observed at 515 nm using the TCSPC detector.<sup>175</sup> Steady-state fluorescence and fluorescence lifetime measurements were conducted on the NBD-labeled liposomes alone, immediately after the addition of 0.5 nM QDs, and at 4 hr and 8 hr following the addition of the QDs to the samples. Only data collected at 4 hr following the QD addition is shown.

### 3.3.10 Preparation of Rhodamine-Labeled Liposomes

Rhodamine-labeled liposomes were prepared with varying rhodamine content and zeta potentials. Initially, a series of POPC-based liposomes with rhod-POPE content varying from 0-30 mol% were prepared to optimize the emission from these

liposomes, as too high a concentration of rhodamine leads to aggregation-induced self-quenching.<sup>179</sup> The lipids for these formulations were self-assembled into liposomes via methods similar to the aforementioned methods—overnight drying, hydration in 2 mM HEPES buffer with 25 mM NaCl (pH = 7.4), 10 freeze/thaw cycles, and extrusions through 50 nm pore membranes. After determining the optimal rhod-POPE content, liposomes of varying zeta potential were prepared by varying the concentration of zwitterionic lipids (POPC and rhod-POPE) to negatively charged lipids (POPG) to positively charged lipids (EPC) in the liposomes. These liposomes were similarly self-assembled. Absorbance, emission, DLS, and zeta potential measurements were performed on the liposomes before experimentation.

#### 3.3.11 Liposome Förster Resonance Energy Transfer (FRET) Assay

Liposome FRET studies were observed using the ‘Emission Scan’ function of the PTI-Horiba QuantaMaster 400 fluorimeter. Prior to combining the components for FRET studies, emission due to direct excitation of the QDs ( $\lambda_{\text{ex}} = 450$  nm) and the rhod-liposomes ( $\lambda_{\text{ex}} = 575$  nm) at relevant and varying concentrations was observed. For the FRET studies, the excitation wavelength was set to 450 nm to directly excite the QDs with minimal indirect excitation of the rhod-liposomes. Fluorescence emission was monitored between 460-700 nm. Within this window the emission maximum of the QDs (545 nm) and of the rhod-liposomes (595 nm) were observed concurrently, via the following steps. First, the emission of the cuvettes with just rhod-liposomes in buffer was detected. Then, QDs were added to one cuvette at a time so that a ‘time = 0’ reading could be taken immediately. These two steps were conducted for each sample to be tested, with a timed record. The samples were

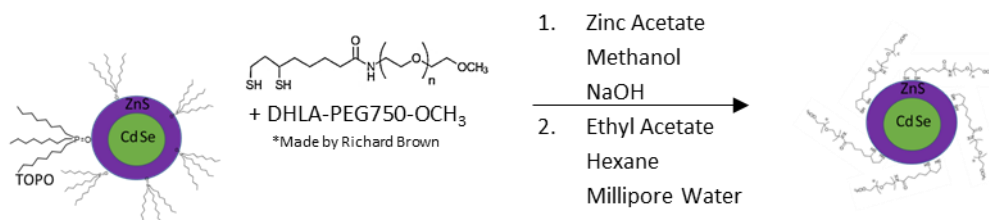
measured over time to monitor changes in FRET/QD-liposome association. Samples were protected from light when not being measured.

### 3.4 Investigating Varying Anti-Membrane Activity with QDs of Different Semiconductor Material Composition and Structure

*Section 3.4 is a modified reproduction of work published in Williams et al. Adverse Interaction of Luminescent Semiconductor Quantum Dots with Liposomes and Shewanella oneidensis. ACS Appl. Nano Mater. 2018, 1 (9).<sup>148</sup>*

#### 3.4.1 Ligand Exchange of Cadmium-containing and Cadmium-free QDs

Luminescent cadmium-containing and cadmium-free QDs, synthesized as organic colloids via hot injection methods as described in Chapter 2, were capped with DHLA-PEG750-OCH<sub>3</sub> ligands to enable their miscibility in aqueous solutions and suitability for the liposome assays in aqueous buffer. The use of the same capping ligand on all QDs enabled direct comparisons to be drawn between the membrane disruption activity of cadmium-containing and cadmium-free QDs. Equally important, the ligand exchange process removed some trioctylphosphine oxide (TOPO) ligands from the QDs' surface and shielded the remaining ones from interacting with liposome membranes (and bacterial cells in Chapter 4).<sup>180</sup> This is an imperative step to minimize the ligands' contribution to QD toxicity, since TOPO has been shown to be highly oxidative.<sup>174</sup> The ligand exchange process was performed following a previously reported procedure (Scheme 3.2).<sup>8</sup>



**Scheme 3.2:** Ligand exchange from TOP to DHLA-PEG750-OCH<sub>3</sub> coated QDs.

### 3.4.2 Using Calcein-containing Liposomes to Investigate the Dependence of Membrane Disruption Activity on QD Cores' Material Composition

Liposome lysis assays (described in Scheme 3.1) with calcein-containing and calcein-free POPC:POPG liposomes were conducted to compare the levels of membrane disruption activity for the cadmium-containing CdSe and CdSe/ZnS QDs to that of the cadmium-free ZnSe and ZnSe/ZnS QDs. Calcein was chosen as the fluorophore for this lysis assay because of its high encapsulation efficiency and the high stability of calcein-containing liposomes in aqueous solutions.<sup>181</sup> Additionally, the QDs used in these membrane disruption assays have minimal absorbance at 480 nm and minimal emission at 515 nm—which lends to minimal spectral overlap with calcein's absorption and emission maxima.

The calcein-containing liposomes were exposed to increasing concentrations (up to 0.5 mg/mL selenium ion equivalents as measured by ICP-MS) of cadmium-containing and cadmium-free QDs. As discussed in Chapter 2, the CdSe core QDs were measured to be a similar size as the ZnSe core QDs and the CdSe cores with 3 monolayers (ML) of a ZnS shell (CdSe/ZnS(3 ML) QDs) were measured to be a similar size as the ZnSe/ZnS QDs (Appendix Figures 2.2 and 2.4). So, these are the QDs directly compared in Figure 3.1. This figure describes the liposome lysis efficiency of the varying QD compositions and demonstrates that all tested QD types have some level of membrane disruption activity. Figures 3.1A and B specifically illustrate the normalized temporal dependence of calcein's fluorescence intensity prior to and after the liposomes' exposure to the cadmium-containing QDs and cadmium-free QDs which contain 0.5 mg/L selenium ion equivalents in their core.

The blue curve in these panels follows the fluorescence intensity ( $\lambda_{em} = 515 \text{ nm}$ ) of systems containing calcein-free liposome controls with CdSe/ZnS(3 ML) QDs (Figure 3.1A) and ZnSe/ZnS QDs (Figure 3.1B) at 0.5 mg/L selenium ion equivalents. The slight increase in fluorescence due to direct excitation of these QDs once added to these dye-free liposome controls represents the highest level of optical interference observed in these experiments. The level of optical interference is significantly lower when CdSe and ZnSe core QDs of the greatest concentration are tested. Therefore, the contribution of the QDs' emission due to their indirect

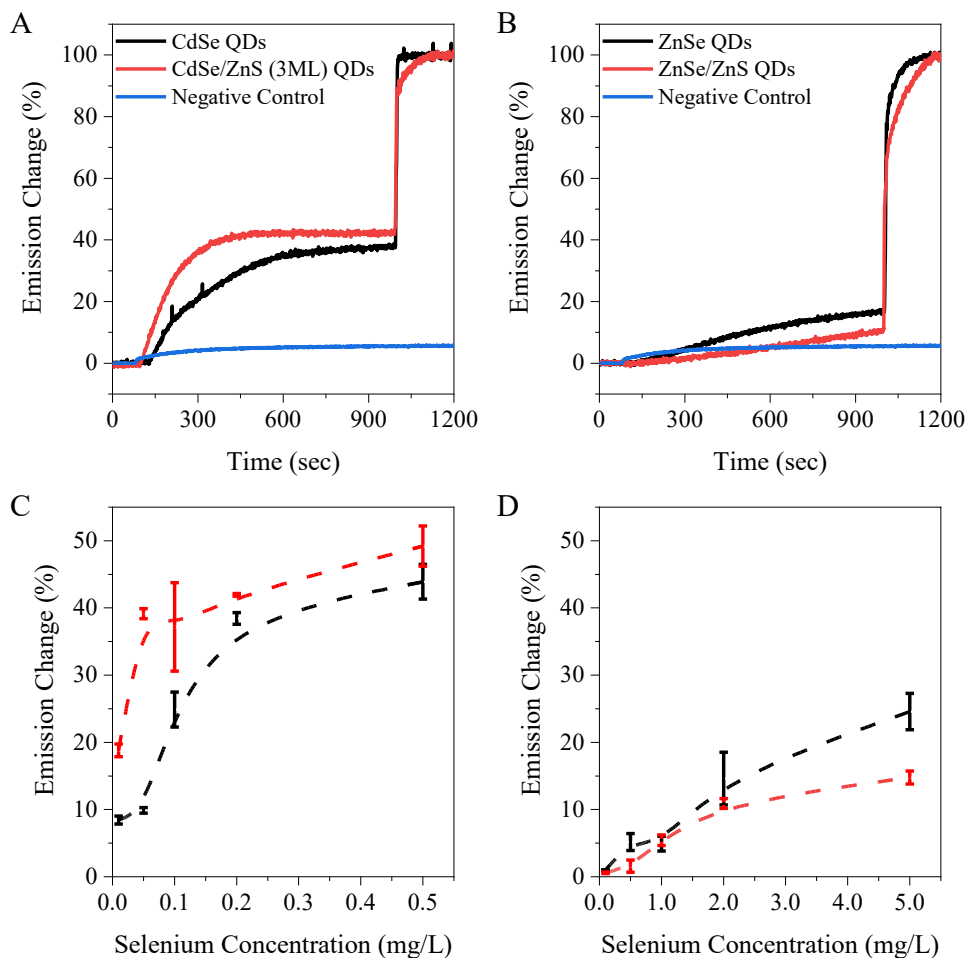


**Figure 3.1:** Representative normalized emission traces compare the membrane disruption activity of CdSe and CdSe/ZnS QDs (A) and ZnSe and ZnSe/ZnS QDs (B). The negative control curves follow the exposure of calcein-free liposomes to the shelled QDs. Liposome lysis efficiency is concentration dependent for the cadmium-containing (C) and cadmium-free (D) QDs. (N = 3).

excitation is considered negligible based on these control measurements. Figure 3.1A shows that CdSe/ZnS(3 ML) QDs cause more liposome lysis than non-shelled CdSe QDs. In contrast, Figure 3.1B shows that ZnSe/ZnS QDs cause less liposome lysis than non-shelled ZnSe QDs. These trends of core vs. core/shells dependence remained regardless of the QD concentration that the liposomes were exposed to, as demonstrated in Figures 3.1C and 3.1D. These figures show the concentration dependence of the liposome lysis (membrane disruption) efficiency when the calcein-containing liposomes were exposed to increasing concentrations of CdSe QDs and CdSe/ZnS(3 ML) QDs (Figures 3.1C), and ZnSe and ZnSe/ZnS QDs (Figures 3.1D). The percent liposome lysis was calculated based on the following equation:

$$\text{Liposome Lysis (\%)} = [(I_{\text{eq}} - I_{\text{b}}) / (I_{\text{tri}} - I_{\text{b}})] \times 100$$

where  $I_{\text{eq}}$  is the equilibrated fluorescence intensity detected from the calcein molecules following the exposure of the calcein-containing liposomes to QDs;  $I_{\text{b}}$  is the background fluorescence intensity of the calcein-containing liposomes prior to QD exposure; and  $I_{\text{tri}}$  is the fluorescence intensity of the sample following the complete disruption and release of calcein molecules due to the rupture of the calcein-containing liposomes by the 1% Triton solution. The level of membrane disruption is concentration dependent for all QD types. Cadmium-containing CdSe and CdSe/ZnS(3ML) QDs exhibit higher levels of membrane disruption activity compared to cadmium-free ZnSe and ZnSe/ZnS QDs. For example, exposure of the calcein-containing liposomes to CdSe and CdSe/ZnS(3ML) QDs with 0.5 mg/L selenium ion equivalents in their core resulted in  $38 \pm 1\%$  and  $42 \pm 1\%$  liposome lysis efficiency, respectively. In contrast, exposure of the calcein-containing liposomes to

ZnSe and ZnSe/ZnS QDs at 10-fold higher selenium ion equivalents (5 mg/L) in their cores resulted in  $15 \pm 4\%$ , and  $10 \pm 1\%$  liposome lysis efficiency, respectively.

Coating the ZnSe QDs with a ZnS shell decreased their membrane disruption activity almost to the level of liposome lysis that was observed when the calcein-containing liposomes were exposed to the DHLA-PEG ligands at ppb levels (the levels anticipated if all ligand molecules would be desorbed from the QD surface, Appendix Figure 3.2). In contrast, coating the CdSe QDs with a ZnS shell slightly increased, rather than decreased, their membrane disruption activity. Both the differences in lysis efficiency between CdSe and ZnSe QDs and the opposite effect that coating them with a ZnS shell has on their membrane disruption activity were unexpected since the synthesis methods used to prepare the CdSe and ZnSe QDs and modify their surface chemistry were nearly identical. The source of these unexpected results is explored in the next two subsections.

#### 3.4.3 Using Calcein-containing Liposomes to Investigate the Dependence of Membrane Disruption Activity on QDs' Core or Core/Shell Structure

Having observed an increase in membrane disruption activity when the CdSe QDs are coated with a ZnS shell, we investigated how the shell thickness affects the liposome lysis efficiency of CdSe/ZnS QDs. (TEM measurements were used to confirm an increase in QD size when CdSe QDs were coated with ZnS shells of increasing thickness (Appendix Figure 2.2).) Figure 3.2 shows the temporal dependence of the calcein's fluorescence intensity prior to and after the calcein-containing liposomes were exposed to 0.5 mg/L Se equivalents of CdSe core QDs (black) and CdSe/ZnS QDs with shell thicknesses of one ML (green), three ML (red),

and six ML (blue). (For the ZnS semiconductor, 1 ML is equal to a 3 nm radius shell<sup>182</sup>, as discussed in Chapter 2.) Liposome lysis efficiencies were calculated from the Figure 3.2 curves using the ‘Liposome Lysis (%)’ equation above. The efficiencies were  $44 \pm 3\%$  for CdSe QDs (no shell),  $42 \pm 1\%$  for CdSe/ZnS QDs with one ML,  $49 \pm 3\%$  for CdSe/ZnS QDs with three ML, and  $70 \pm 1\%$  for CdSe/ZnS QDs with six ML of ZnS shell thickness. A lower membrane disruption efficiency was observed when the liposomes were exposed to CdSe/ZnS QDs(1 ML)

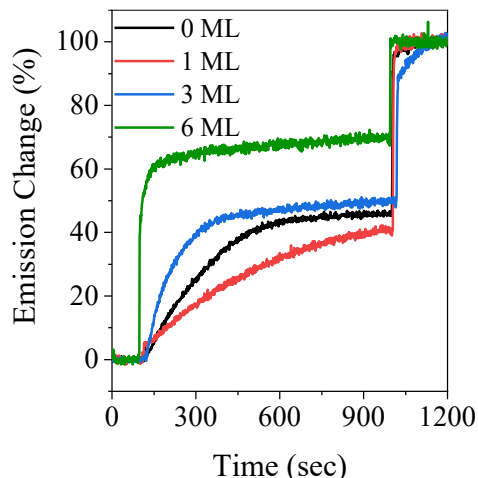


**Figure 3.2:** Normalized emission traces from calcein-filled liposomes exposed to CdSe QDs with 0 to 6 monolayers (ML) of a ZnS shell(A). (While measurements were done in triplicate, only one representative trace is shown.)

rather than the bare CdSe cores. However, overall, adding shell thickness only seems to delay—rather than prevent—liposome lysis, as further increases in shell thickness resulted in increasing membrane disruption activity.

These results led to the conduction of ICP-MS measurements aimed at determining levels of QD ion dissolution, an indication of the QDs’ chemical stability. Cadmium, zinc, and selenium ions were detected from filtered samples after QDs were incubated in water (the QD storage medium) and in HEPES (the liposome assay medium). The cadmium-free ZnSe and ZnSe/ZnS QDs did not demonstrate any significant dissolution in either incubation condition, as indicated by negligible levels of zinc and selenium ions measured in the supernatants of their incubated samples (data not shown). In water, the CdSe and CdSe/ZnS QDs of varying ZnS shell size did not have significant ion dissolution (data not shown). Figure 3.3 plots the levels of

ion dissolution for CdSe and CdSe/ZnS QDs which were incubated in HEPES buffer (pH 7.4), at concentrations ranging from 0 to 0.5 mg/L selenium ion equivalents.

The levels of cadmium and selenium measured in the supernatant for these QDs

were below the detection limits of our method. However, the CdSe/ZnS QDs exhibited significant zinc ion dissolution over 24 hours, which increased with the QDs' concentration and ZnS shell thickness. It should be noted that it is difficult to quantify the amount of released zinc ions from the QDs due to high native levels of zinc in aqueous samples and glassware<sup>183</sup>, so these numbers are reported in signal equivalents, above the baseline, rather than concentrations. Nevertheless, the measured levels' dependence on the QD concentration and ZnS shell thickness strongly suggest a significant level of zinc ion dissolution from the CdSe/ZnS QDs within the time scale of our liposome lysis assays. It is therefore fair to conclude that zinc ion dissolution increases the adverse impact of CdSe/ZnS QDs on the liposome membranes beyond their impact due to membrane association alone. Further, it may seem interesting that ZnSe/ZnS QDs exhibited significantly higher shell stability even though the CdSe and ZnSe cores were coated with the same ZnS shell using

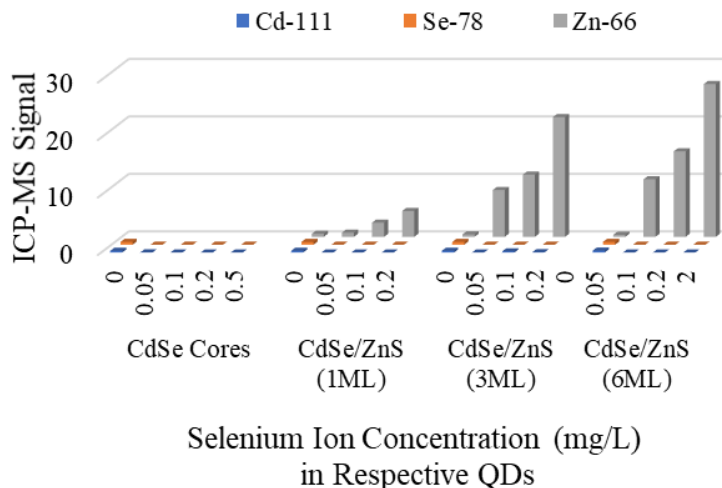


**Figure 3.3:** ICP-MS measured intensities of zinc, cadmium, and selenium ions resulting from the dissolution of CdSe QDs of varying ZnS shell size. Only significant zinc ion dissolution is observed, indicating degradation of the ZnS shell in the timespan of our assays. (N = 3; Error bars are omitted for figure clarity. Published as Figure 3B in Williams et al. Applied Nano Materials. 2018, 1 (9), 4788-4800.<sup>148</sup>)

nearly identical shelling conditions. However, the literature has attributed an increasing ZnS shell size to decreasing CdSe/ZnS QD stability due to significant crystal plane mismatching between the CdSe and ZnS lattices, which would lead to significant lattice strain and QD dissolution.<sup>184-186</sup> Contrarily, there is minimal crystal mismatch between ZnSe and ZnS lattices, so the ZnSe/ZnS QDs would remain stable.

Since ion dissolution was detected with some QD samples, calcein-containing liposomes were exposed to cadmium chloride, zinc chloride, and sodium selenite, which served as Cd<sup>2+</sup>, Zn<sup>2+</sup>, and Se<sup>4+</sup> ion control exposures, respectively (Appendix Figure 3.3). The salts for the metal ion controls were chosen to readily generate the metals' predominate oxidation state once dissolved in water.<sup>187, 188</sup> Even exposed to free ion concentrations that would only exist if the highest concentration of QDs completely dissolved, the calcein-containing liposomes were negligibly lysed by selenium and cadmium ion controls. Significant lysis was observed with zinc ion controls, which supports the notion that the significant ZnS shell dissolution from the CdSe/ZnS QDs may contribute to their liposome lysis. Further the behavior of the zinc ion controls supports the ICP-MS results which show negligible ion dissolution from ZnSe and ZnSe/ZnS QDs.

#### 3.4.4 Using Nitrobenzoxadiazole (NBD)-labeled Liposomes to Investigate Changes in Polarity and ROS Activity at the Membrane

Since the free ion liposome exposures alone cannot fully explain the differences in membrane disruption activity, we further postulated that: 1) the instability of the ZnS shell on our CdSe/ZnS QDs could result in zinc ion dissolution at the membrane after QD association and 2) this leads to an increase in local ion

concentration near the membrane which would allow the ions to contribute to membrane disruption. Literature supporting this hypothesis has linked the association of degraded QDs to increased toxicological effects.<sup>32, 60</sup> Thus, QD-membrane association was next to be investigated. Nitrobenzoxadiazole (NBD)-labeled POPC:POPG liposomes were prepared in order to probe the association of the cadmium-containing and cadmium-free QDs with membranes. NBD was chosen because this dye's fluorescence properties are sensitive to its environment. A fluorescence intensity increase and a fluorescence lifetime decrease are measured when the NBD environment observes a polarity decrease.<sup>175</sup> In contrast, a fluorescence intensity decrease is detected when NBD molecules react with ROS.<sup>178</sup> The trends described below did not depend on QD core or core shell structure, so only QD core data is shown.

Figure 3.4 describes the results of the NBD liposomes' incubation with the cadmium-containing and cadmium-free core QDs. Representative fluorescence spectra of NBD prior to and following exposure of NBD liposomes to CdSe and ZnSe QDs are shown in Figures 3.4A and 3.4B. The fluorescence spectra of NBD liposomes ( $\lambda_{\text{ex}} = 470 \text{ nm}$ ) prior to and following QD exposures are shown in black and red, respectively. The control fluorescence spectra of CdSe and ZnSe QDs, at the exposure concentration, for this unfavorable excitation wavelength are shown in blue. A six-fold increase in the fluorescence intensity from the NBD liposomes is observed following their exposure to CdSe (Figure 3.4A) and ZnSe (Figure 3.4B) QDs. Considering the literature, this can be attributed to decreased polarity in the NBD environment due to the association of the QDs with the liposomes, which effectively

shields the NBD headgroup from the water molecules and ions of the buffer. The lack of fluorescence intensity decrease following the incubation of QDs with the NBD liposomes strongly suggests that ROS are not formed and are therefore not a significant contributor to membrane disruption under these experimental conditions. This is an acceptable conclusion considering this assay was a short exposure under room light conditions, and without direct QD irradiation. The representative lifetime traces ( $\lambda_{em\ max} = 515\ nm$ ), shown in Figure 3.4C for CdSe and Figure 3.4D for ZnSe QDs, provide additional indications that the QDs associate with the liposomes.

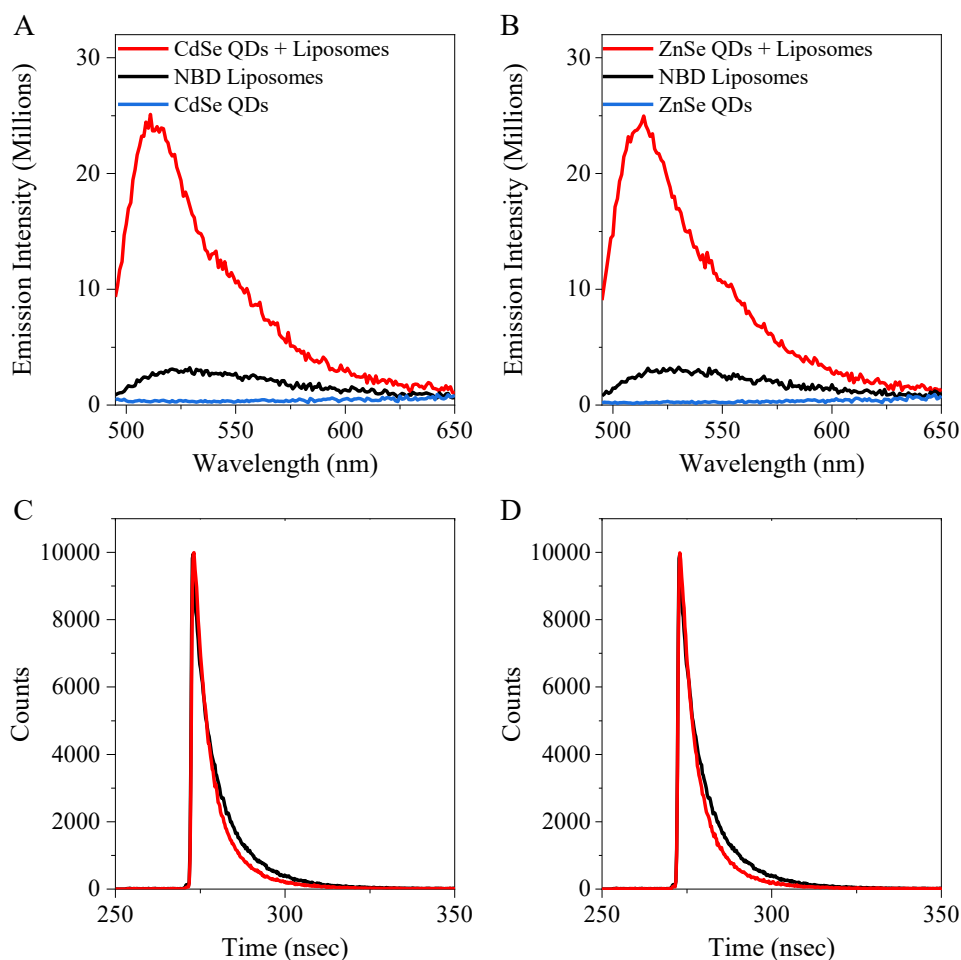


**Figure 3.4:** Fluorescence intensity of NBD-labeled liposomes (black), QDs (blue), and following a 4 hr incubation of NBD-labeled liposomes with QDs (red) show significant NBD fluorescence increases for both CdSe (A) and ZnSe (B) QDs ( $\lambda_{ex} = 470\ nm$ ). Time-resolved photoluminescence decay curves of NBD-liposomes (black) and following a 4 hr incubation with QDs (red) for CdSe QDs (C) and ZnSe QDs (D) show a decrease in fluorescence lifetime ( $\lambda_{ex} = 470\ nm$ ,  $\lambda_{em} = 515\ nm$ ).

**Table 3.1.** A summary of the fluorescence lifetime and exponential terms used to fit the fluorescence lifetime decay curves for NBD-liposomes prior to and following exposure to CdSe and ZnSe QDs. The weighted fluorescence lifetime equation:  $\tau$  (nsec) = ( $\tau_1 \times wt_1$ ) + ( $\tau_2 \times wt_2$ ).

	Weighted Fluorescence Lifetime, $\tau$ (nsec)	$\tau_1$ (nsec)	$wt_1$ (%)	$\tau_2$ (nsec)	$wt_2$ (%)
NBD-Liposomes	$5.87 \pm 0.23$	2.81	54.81	9.58	45.17
ZnSe QD and NBD-Liposomes	$5.23 \pm 0.02$	3.84	72.48	9.43	27.52
CdSe QD and NBD-Liposomes	$5.17 \pm 0.03$	3.78	72.51	9.24	27.49

Table 3.1 summarizes the fluorescence lifetime and the exponential terms which explain the fit of the fluorescence lifetime decay curves of the NBD liposomes prior and following a 4-hour long exposure to CdSe and ZnSe QDs (Figure 3.4C and D). A decrease in the fluorescence lifetime from  $5.87 \pm 0.23$  nanoseconds (nsec) to  $5.17 \pm 0.03$  nsec and to  $5.23 \pm 0.03$  nsec when the NBD liposomes are incubated for 4 hours with CdSe and ZnSe QDs, respectively, is observed. Additionally, the fluorescence lifetime decay curve of NBD liposomes prior to QD exposure is described by two exponential terms,  $\tau_1 = 2.81$  nsec and  $\tau_2 = 9.58$  nsec, with almost equal weights of about 55 and 45%, respectively. These two terms are attributed to the NBD's heterogeneous environment, which include the hydrophobic backbone of the liposome bilayer, the unrestricted movement of the dye on the outer lipid heads, and the aqueous environment of the liposomes.<sup>176</sup> A significantly increase in mono-exponential character is observed when the QDs interacted with the liposomes. The fluorescence lifetime decay curves for exposed NBD liposomes (red) are still described by two exponential terms. However, the terms change to  $\tau_1 = 3.78$  nsec and  $\tau_2 = 9.24$  nsec for CdSe QDs and  $\tau_1 = 3.84$  nsec and  $\tau_2 = 9.43$  nsec for ZnSe QDs. Additionally, the weights of these components change to about 72 and 28% for both

QD types, respectively. The decrease in fluorescence lifetime and the increase in mono-exponential character of the fluorescence lifetime decay curves are consistent with a decrease in the polarity of the NBD environment, which is attributed to association of the QDs to the NBD liposomes. The changes in NBD's fluorescence intensity and lifetime—which are indicative of QD-liposome association—do not significantly depend on the QDs' core composition. However, as QD-liposome association is concurrently occurring while these QDs undergo different levels of ion dissolution, the combination of these two mechanisms have been owed responsibility for the different rates of membrane disruption activity observed in this chapter and the different effects on cell viability to be discussed in Chapter 4.

### **3.5 Investigating Varying QD-Membrane Association Activity with Liposomes of Different Lipid Compositions**

#### 3.5.1 Establishing and Optimizing a Förster Resonance Energy Transfer (FRET) System to Investigate Levels of QD Association with Membranes

Since the NBD liposome incubation studies revealed that the QDs' material and structure did not affect levels of QD-membrane association, we began to investigate QD characteristics that the literature indicates would: QDs' surface ligand composition and charge.<sup>29, 59, 189</sup> There are numerous studies where association between QDs and other entities have been investigated using FRET, since this phenomenon is extremely sensitive to the distance between an energy donor and an energy acceptor.<sup>142, 190-193</sup> Thus, liposome FRET assays with QDs of varying surface chemistry and rhodamine B-labeled liposomes (rhod-liposomes) of varying lipid compositions were conducted to illustrate how surface ligand chemistry affects levels

of QD-membrane association. Rhodamine B was chosen as the FRET acceptor as it 1) has high water solubility, 2) is often used as a FRET pair component in systems that achieve high FRET efficiency, and 3) has optimizable intermolecular quenching.<sup>190, 194, 195</sup> Further, rhod-labeled lipids are readily available and have the desired optical properties for a FRET acceptor component. The Qdot545 ITK™ carboxyl- and amino- terminated polyethylene glycol coated CdSe/ZnS QDs (to be referred to as ‘Qdots’ to distinguish them from the in-house synthesized CdSe/ZnS QDs)—which were characterized in Chapter 2—were chosen as the FRET donor component since this component needed to be QDs 1) with sufficient emission overlap with the absorbance of the rhod-liposomes and 2) that only differed in the surface coverage. These Qdots had the same absorbance and emission intensities and spectra at the same molar concentrations since the distributor was able to modify the surface coverage of their QDs without affecting their optical behaviors. Furthermore, Figure

3.5 shows the normalized absorbance and emission spectra for the Qdots and the rhod-liposomes that were measured in separate cuvettes and overlaid to illustrate an overlap of the Qdots’ emission and the rhod-liposomes’ absorbance that should be sufficient for FRET if the entities are within close proximity of each other.

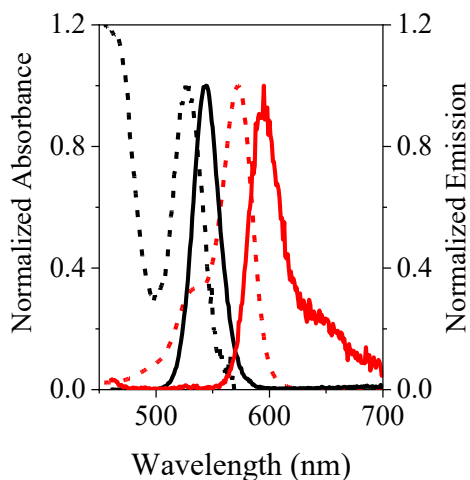


**Figure 3.5:** Spectra showing the spectral overlap and potential for FRET between the Qdot donors (black) and rhod-liposome acceptors (red). ( $\lambda_{ex} = 450 \text{ nm}$ )

Before analyzing levels of QD-membrane association with all the intended QD and liposome variations, the FRET system needed to be optimized. To maximize

the emission intensity of the rhod-liposomes, A the intermolecular quenching of rhodamine B was minimized by varying the rhod-POPE content in POPC-based liposomes. The amount of rhod-POPE that was added to POPC lipids during liposome preparations was varied from 0-30 mole percent (mol%) of the total lipid concentration. DLS and zeta potential characterizations of these liposomes indicate that they are all between 55-85 nm in diameter and negatively charged (Appendix Table 3.1). Figure 3.6 shows the absorption and emission ( $\lambda_{\text{ex}} = 570 \text{ nm}$ ) spectra for the varying rhod-liposome compositions in HEPES (pH 7.4). Figure 3.6A shows that the absorbance intensity of the liposomes continually increases with increasing rhod-POPE mol%. Figure 3.6B shows that 1) the emission intensity of the liposomes increases up to the 3 mol% formulation, 2) the turning

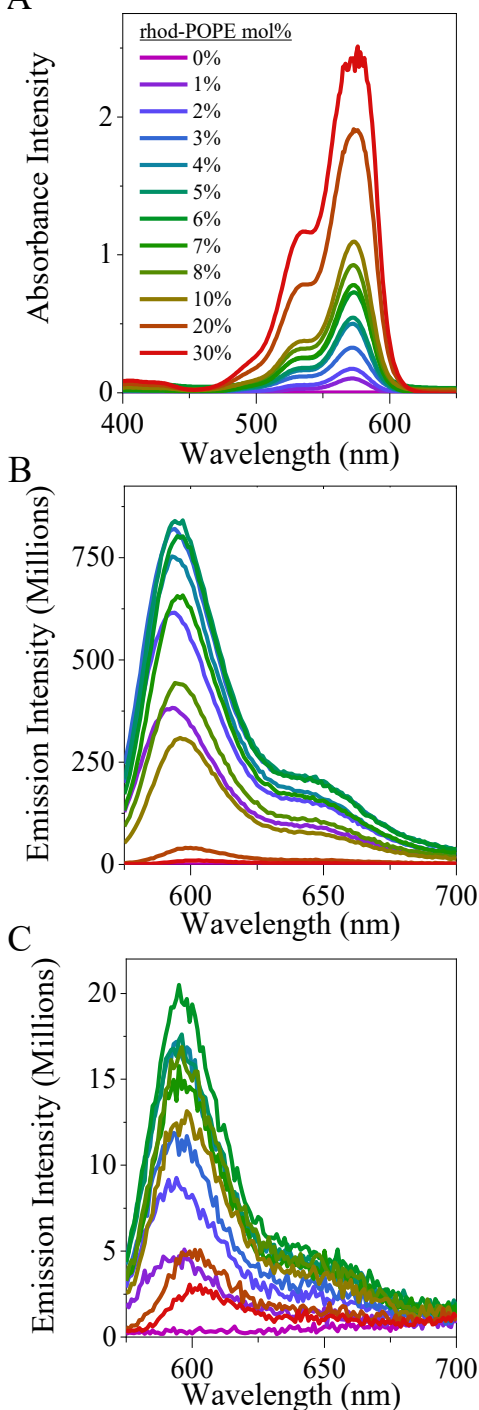


**Figure 3.6:** Optical properties of rhod-liposomes with varying rhod-POPE content. The absorbance intensity of the liposomes increases with increasing rhod-POPE mol% (A). With direct rhod-liposome excitation ( $\lambda_{\text{ex}} = 570 \text{ nm}$ ), the emission intensity increases up to the 3 mol% rhod-POPE formulation and decreases after 6 mol% rhod-POPE, with concentration dependence (B). With indirect rhod-liposome excitation ( $\lambda_{\text{ex}} = 450 \text{ nm}$ ), the emission intensity increases up to the 6 mol% rhod-POPE formulation and decreases immediately after, with concentration dependence (C).

point of emission intensity is within the 3-6 mol% rhod-POPE formulations, and 3) there is a concentration dependent decrease in emission intensity above 6 mol% due to rhodamine's self-quenching behavior. Figure 3.6C shows the emission intensity detected from the liposomes of varying rhod-POPE content after using 450 nm excitation—the wavelength used to excite the Qdots in the FRET studies described below. These experiments were done to detect the background emission that may result from indirect excitation of the rhod-liposomes. Minimal excitation and emission were expected from the rhod-liposomes because the rhodamine B does have minimal absorbance at several wavelengths, including at the near-UV to blue wavelengths that are optimal for exciting the Qdots. With indirect excitation, the background emission intensity from the rhod-liposomes increased with increasing rhod-POPE up to the 6 mol% formulation, and thereafter decreased with increasing concentration. The background emission intensity (Figure 3.6C) detected from all samples was at most 2.5% of their respective direct emission intensity (Figure 3.6B). Since the maximum direct emission intensity was achieved with 3-6 mol% rhod-POPE and the background intensity increases through the 6 mol% formulation, the 3 mol% rhod-POPE formulation had the best signal-to-noise ratio. Thus, 3 mol% rhod-POPE content was used in all further rhod-liposome formulations.

Next, in order to ensure FRET would occur between QD donors and the rhod-liposome acceptors with the expected association and light activation dependency, we varied the amount of carboxyl Qdots that were added to HEPES solutions with 3 mol% rhod-POPE:POPC liposomes. Figure 3.7 shows the level of FRET between the same concentration of rhod-liposomes with varying concentrations of Qdots. As the

rhod-liposomes were exposed to increasing concentrations of Qdots, the emission detected from them increased. Control experiments with just Qdots in HEPES further confirmed the occurrence of FRET as the emission intensities from the Qdots alone were higher than those detected from the Qdots in the presence of rhod-liposomes (data not shown).

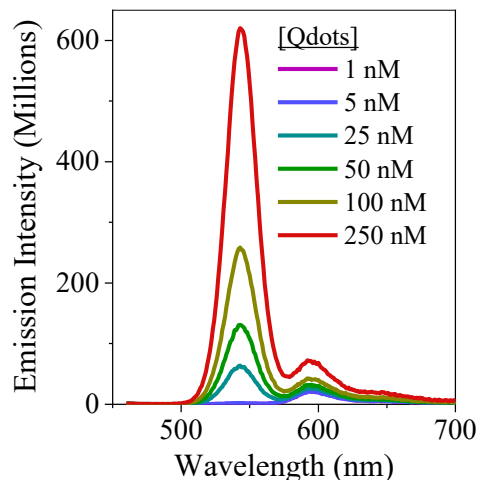


**Figure 3.7:** Emission from Qdot-rhodamine FRET system with increasing concentrations of Qdots show concentration dependent emission intensities. ( $\lambda_{\text{ex}} = 450 \text{ nm}$ )

These experiments confirmed that our FRET

system had direct excitation of the Qdots which emitted energy that was either 1) detected as light or 2) transferred to the rhod-liposomes to excite rhodamine B and allow it to emit detectable energy. We assume that the QDs and rhod-liposomes must be in close proximity for this FRET to be detectable.

### 3.5.2 Using Rhodamine-labeled Liposomes of Varying Lipid Composition to Investigate the Impact of Lipid Composition on QD Association

After proving a working FRET system with the carboxyl Qdots and 3 mol% rhod-POPE:POPC liposomes, investigations into how the levels of FRET may change when using a different QD ligand coatings and varying liposome compositions began. The first experiments probed whether the same 3 mol% rhod-POPE:POPC liposomes would have different levels of association with carboxyl Qdots compared to amino Qdots (Figure 3.8). Figure 3.8A illustrates the FRET observed, at time = 0, when the same concentrations of rhod-liposomes were exposed to 50 nM of carboxyl-terminated (red) and amino-terminated (black) Qdots. Figures 3.8B and C illustrate

the change in emission intensity for the same systems over time; with the emission from the Qdots shown in red and the emission from the rhod-liposomes in black. Figure 3.8 demonstrates that more energy is absorbed from the amino Qdots than the carboxyl Qdots over time, as the emission intensity from these QDs is lower upon first contact with the rhod-liposome solution and continues to decrease over time at a greater rate. This may be indicative of more amino Qdots binding to liposomes than the carboxyl Qdots. However, the emission intensity and rate of intensity change detected from the rhod-liposomes when interacting with both systems does not appear statistically significant. Further experiments focused on studying the efficiency of FRET between the different Qdots and rhodamine B would be necessary to extrapolate more information from these observations.

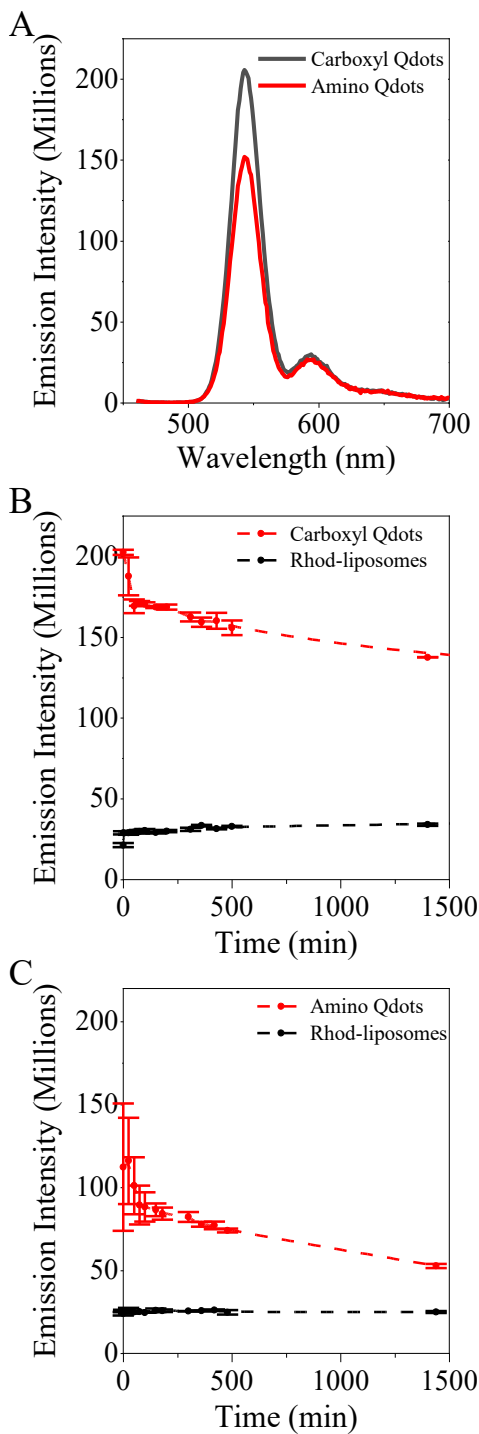


**Figure 3.8:** Emission spectra after observing FRET between Qdots and 3 mol% rhod-POPE:POPC liposomes. Amino Qdots (red) have a smaller emission intensity at time 0 of FRET than the carboxyl Qdots (black) (A). Over time the trend remains that the carboxyl Qdots (B, red) have greater emission intensity with FRET than the amino Qdots (C, red). However, there is no significant difference in the amount of emission detected from the rhod-liposomes (B & C, black) between the two Qdots. (N = 2)

The second set of experiments, with both the carboxyl and amino Qdots, monitored FRET between the Qdots and rhod-liposomes of different lipid composition. Liposome batches made of 1) 3 mol% rhod-POPE lipids, 2) either 10 mol% or 20 mol% of charged lipids, and 3) the remaining moles being the zwitterionic POPC lipids were prepared. The charged lipids were either the positively charged EPC lipids or the negatively charged POPG lipids. Thus, a five-member charge series of 3 mol% rhod-liposomes—including the original rhod-POPE:POPC liposomes with no charged lipids (just POPC liposomes)—with zeta potentials ranging from negative to positive 40 mV was available to study with the two Qdot formulations. The DLS and zeta potential characterizations of this charge series can be found in Appendix Table 3.2. Figure 3.9 illustrates the FRET observed between the two Qdots and three of the five 3 mol% rhod-liposome formulations over time. (Data for the 10 mol% EPC and 10 mol% POPG formulations are omitted for figure clarity, but generally follow the trends respective to liposome charge.) Both the carboxyl (A) and amino (B) Qdots experience their largest decreases in emission over time when put into the same environment as positively charged liposomes (red) compared to when they are with more neutrally (black) and negatively charged (blue) liposomes. While it may be expected that the carboxyl and amino Qdots would have opposite trends—with the carboxyl Qdots being more attracted to (losing more emission with) the positively charged liposomes and the amino Qdots being more attracted to the negatively charged liposomes—recall that in the Chapter 2 zeta potential characterizations, both Qdots were observed to have an overall negative potential in the HEPES buffer system. Collaborators who have worked with similar

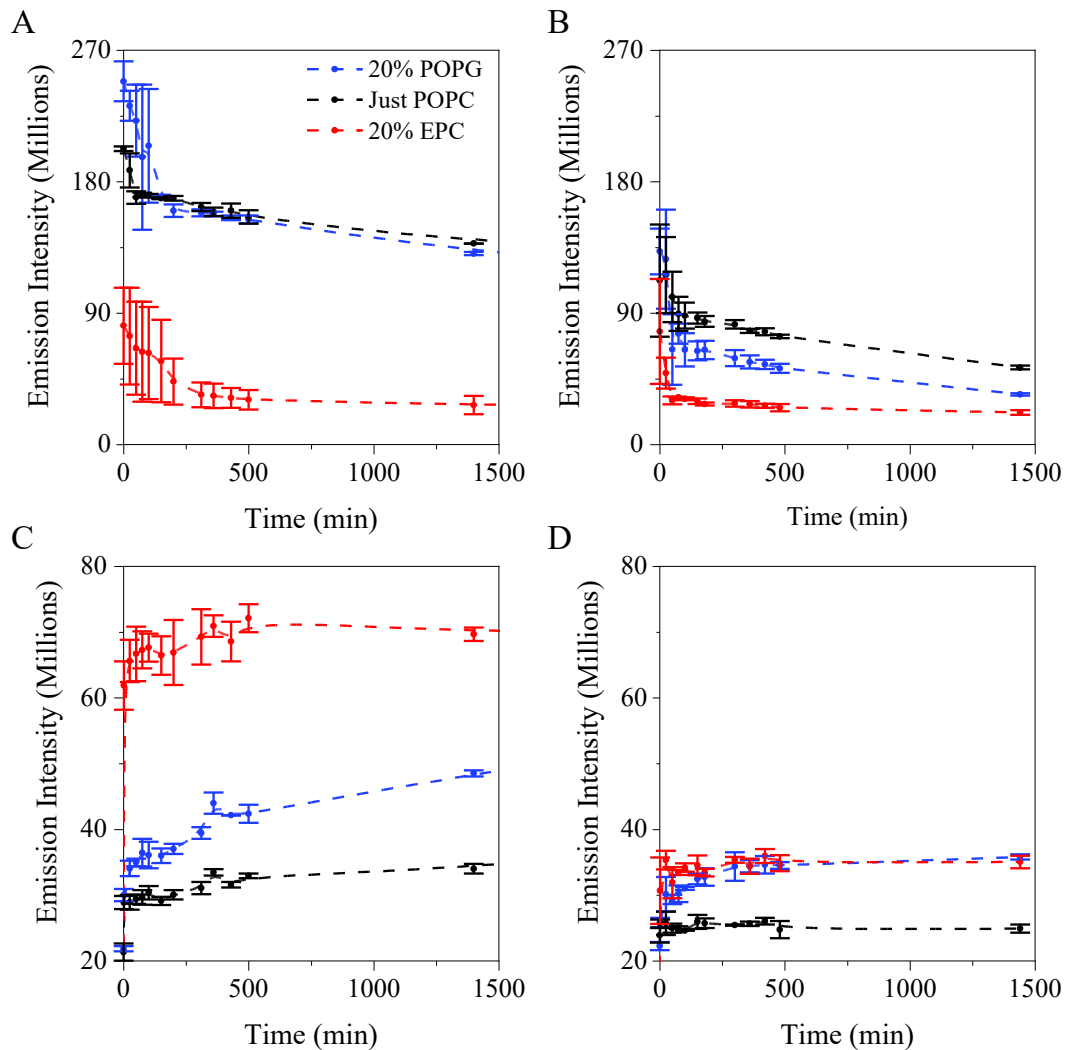


**Figure 3.9:** Emission spectra after observing FRET between Qdots and 3 mol% rhod-POPE liposome formulations that are either more negatively (blue), neutrally (black), or positively (red) charged due to the different lipid components. Carboxyl Qdots had more significantly decreased emissions (A) and induced more rhodamine emissions (C) in the presence of more positively charge liposomes compared to other formulations. The amino Qdots compounding negative charge and surface amine characteristics resulted in more significant interaction with both the positively and negatively charge liposome formulations (B and D). (N = 2)

batches of the amino Qdots have confirmed the presence of primary amines on their surface, and have speculated that there must be other components on the QDs which are 'shielding' their charge.<sup>196</sup> The presence of these surface amines on the amino Qdots may explain why these dots lose their next largest amount of emission capacity to the more negatively charged liposomes rather than the neutral formulations, while

the carboxyl Qdots—which lack surface amines—interact fairly equally with those formulations.

Figures 3.9C and D recapitulate the trends observed in A and B, but from the perspective of how much emission is observed from the rhod-liposomes after interaction with the Qdots. The carboxyl Qdots transfer energy to and allow significantly more emission to be detected from the positively charged liposome formulations (red) rather than the more neutral (black) or negative (blue) formulations (C). The amino Qdots result in statistically similar emission detected from the positive (red) and negative (blue) liposome formulations; which is significantly more than the emission detected from their energy transfer to the more neutrally charged (black) formulations. Conclusively, QD-membrane association can be driven by tuning electrostatic attractions between the two entities.

### **3.6 Conclusions**

This chapter uses model lipid bilayer vesicles, aka liposomes, to elucidate how interactions between QDs and membranes may be affected by differences in QDs' material, structural, and surface ligand compositions and by differences in membranes' lipid compositions. The liposomes used in these studies were imbedded with dyes which emitted optical signals that correlated to specific QD interactions with the membranes.

Membrane disruption assays, with calcein-labeled liposomes, demonstrated that cadmium-containing QDs had more membrane disruption activity than cadmium-free QDs. This difference in membrane disruption was unexpected since the liposomes lacked metal-specific receptors that would distinguish between the QDs'

material composition. Additionally, these membrane disruption assays demonstrated a very unexpected result: ZnS shelling mitigated the membrane disruption activity of the cadmium-free QDs, but not of the cadmium-containing QDs. This was evident even though the QDs' syntheses and ligand exchanges occurred via similar protocols, and both QD core types had improved optical performance upon shelling (which is indicative of effective surface passivation).

Thus, QD incubations with NBD-labeled liposomes were used to test for possible differences in the QDs' association and ROS generation, and ICP-MS was used to measure levels of QD ion dissolution. The NBD-liposome incubations demonstrated that the QDs' membrane disruption activity was not due to ROS generation, but was instead due to membrane depolarization. These incubations did not indicate significant differences in membrane depolarization between the cadmium-free and cadmium-containing core and core/shell QDs. However, the ICP-MS measurements demonstrated that the cadmium-containing QDs were less stable than the cadmium-free QDs in the aqueous HEPES medium used for these liposome assays. Furthermore, it highlighted that the cadmium-containing QDs had increased ion dissolution as their shell size increased, which indicated increasing levels of QD instability with shelling. This lack of QD stability likely resulted in the cadmium-containing QDs dissolving into membrane disrupting ions in high local concentrations upon liposome association.

Rhod-labeled liposomes proved that QDs could associate with membranes and illustrated how QDs' surface ligand chemistry impacted the levels of QD association. QD incubations with rhod-liposomes demonstrated that electrostatic forces play a

large role in QD-membrane association. Further, these incubations also showed that not only surface charge, but also that the molecular structure of all QD surface molecules impact the levels of QD-membrane association. This became evident through negatively charged amino QDs' incubations with liposomes of varying zeta potential. Electrostatic implications were evident due the larger association between these amino QDs and the positively charged liposomes, rather than with the more neutral and negatively charged liposomes. However, the next largest association was with the negatively charged liposomes, rather than the more neutrally charged liposomes, likely due to the presence of the quaternary amines on the amino QDs' surfaces.

Altogether, these QD-liposome studies highlight the importance of controlling QDs' structure, surface ligand chemistry, and chemical stability for tuning the intended and unintended interactions between them and membranal targets.

## Chapter 4: Investigating the Antibacterial Activity of Cadmium-containing and Cadmium-free QDs against *Shewanella oneidensis* MR-1, an Environmental Health Model.

*This chapter is a modified reproduction of work published in Williams et al. Adverse Interaction of Luminescent Semiconductor Quantum Dots with Liposomes and Shewanella oneidensis. ACS Appl. Nano Mater. 2018, 1 (9).<sup>148</sup>*

### 4.1 Purpose

This chapter compares the impact of cadmium-containing and cadmium-free core and core/shell QDs against the viability of *Shewanella oneidensis* MR-1, an environmental health-relevant bacteria model. These studies were conducted parallel to the liposome studies with the same QD types, as described in Chapter 3. The findings of the liposome experiments included that: 1) the CdSe and CdSe/ZnS QDs showed higher membrane disruption activity than the ZnSe and ZnSe/ZnS QDs, 2) shelling did not mitigate the membrane disruption activity of the CdSe cores, and 3) the activity of the QDs was correlated to their association and ion dissolution at the liposomal membrane. This chapter—investigating QDs activity against *S. oneidensis*—continues the investigation of how QDs' material and structure influence their environmental implications. We hypothesized that the interactions between the QDs and the negatively charged bacterial membranes of *S. oneidensis* would be similar to the interactions of these QDs with the negatively charged liposomes.

### 4.2 Introduction

Water- and soil-thriving bacteria are often used to model the environmental implications of naturally- and artificially-occurring entities. When studying the

implications of nanomaterials on the environment, specifically, bacteria in the *Shewanella*, *Pseudomonas*, *Acinetobacter*, *Azotobacter*, *Bacillus*, and *Sinorhizobium* genera are primarily used as the bacterial models.<sup>197-201</sup> Of all the strains within these genera, the *Shewanella oneidensis* MR-1 strain is particularly interesting because of this bacterium's ability to cycle and reduce heavy metal ions for metabolic purposes.<sup>172, 202</sup> Additionally, this bacterium has previously been used in similar nanoparticle implication studies.<sup>33, 172, 202, 203</sup> Thus *S. oneidensis* MR-1 was used to model the potential environmental implications of our heavy metal-containing QDs.

This chapter discusses studies which investigated the hypotheses that 1) the cadmium-containing QDs have greater impacts on *S. oneidensis* viability than the cadmium free QDs and that 2) a ZnS shell mitigates the cadmium-containing QDs' impact on cell viability. To test these hypotheses, we studied the interactions between cadmium-free (ZnSe, ZnSe/ZnS, and Mn:ZnSe/ZnS) QDs and cadmium-containing (CdSe and CdSe/ZnS of varying shell size) QDs with *S. oneidensis* MR-1. ICP-MS, hyperspectral imaging, and biological TEM were used to investigate the association between the QDs and bacterial cells. Additionally, the impact of the QDs on *S. oneidensis* cells' viability was measured using a drop plate assay.

## **4.3 Materials, Instrumentation, and Methods**

### 4.3.1 Materials and Reagents

*Shewanella oneidensis* MR-1 (BAA-1096) were purchased from American Type Culture Collection Inc. Instrument Calibration Standard 2 (5% HNO<sub>3</sub>/ Tr. Tart. Acid/Tr. HF) for inductively coupled plasma mass spectrometry (ICP-MS) was purchased from Claritas PPT SPEX CertiPrep. 4-(2-hydroxyethyl)-1-

piperazineethanesulfonic acid (HEPES) buffer (1 M), acetone, BD Difco Dehydrated Culture Media: Granulated Agar, chloroform, Corning Cellgro DPBS (1X), BD Difco Dehydrated Culture Media: Luria–Bertani (LB) broth, Dulbecco’s Phosphate-Buffered Saline (without calcium and magnesium), ethanol, nitric acid (Trace Metal grade), and zinc chloride were purchased from Fisher Scientific. Amicon Ultra centrifugal filter units, cadmium chloride (CdCl<sub>2</sub>), sodium chloride (NaCl), and sodium selenite were purchased from Sigma-Aldrich. Dihydro lipoic acid polyethylene glycol methoxy (DHLA-PEG750-OCH<sub>3</sub>) was prepared and purified with slight modifications to a previously reported protocol.<sup>165, 166</sup>

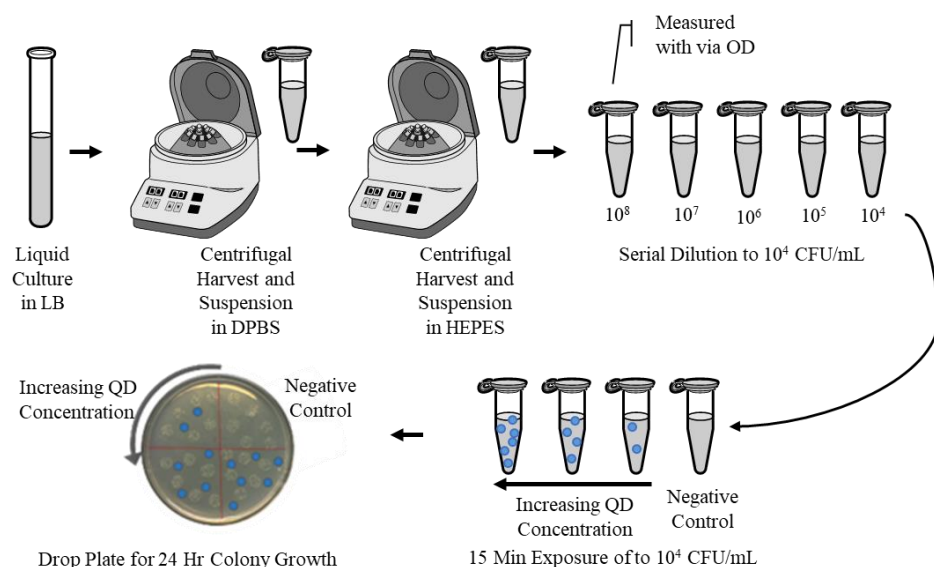
#### 4.3.2 Instrumentation

ICP-MS was conducted on a PerkinElmer NexION 300D single quadrupole mass spectrometer. Cytoviva hyperspectral imaging (Cytoviva) was observed with an Olympus BX-41 microscope fitted with a spectrophotometer and an integrated charge-coupled device (CCD) camera. Biological transmission electron microscopy (BioTEM) images were obtained using a FEI Tecnai T12 TEM.

#### 4.3.3 Bacterial Culture and Colony Counting

Scheme 4.1 illustrates the *Shewanella oneidensis* MR-1 liquid culture and colony counting procedures. Stock *S. oneidensis* cultures were started by streaking an LB-agar plate with cells and then incubating the plate in a 30 °C incubator overnight. Liquid cultures were grown from the stock by transferring colony inoculants from the plate to 10 mL of LB broth, and then incubating the bacterial cell suspensions for 4 hr, or until the cells reach their mid log phase, at 30 °C in an orbital shaker. Cells were then harvested by centrifugation for 10 min at 2,000 × g, washed in Dulbecco’s

phosphate buffered saline (DPBS) buffer, and suspended in HEPES buffer solution (2 mM HEPES with 25 mM NaCl in Millipore water, at pH 7.4). The cultures were then diluted to 0.2 optical density at 600 nm ( $OD_{600}$ ) to achieve a cell density of approximately  $2 \times 10^8$  colony-forming units (CFUs)/mL. Serial 10-fold dilutions of this bacterial suspension were performed to achieve a cell concentration of  $1 \times 10^4$  CFUs/mL in HEPES buffer. In a total volume of 150  $\mu$ L, the resultant diluted bacterial suspension was treated with QDs or ion controls (zinc chloride for zinc, cadmium chloride for cadmium, and sodium selenite for selenium) at varying concentrations. The exposed bacterial cells were incubated on a rotary shaker for 15 min, and then the viability of the cells was determined using the following established drop plate colony-counting protocol.<sup>204</sup> Six 10  $\mu$ L droplets of the exposed bacterial suspensions and untreated negative controls were dropped on an LB-agar plate, which had been pre-sterilized under UV illumination for 20 min. The droplets were dried under air flow in a biological cabinet and then incubated at 30 °C for 20 hr before the colonies were counted using a Bantex Colony Counter 920A.



**Scheme 4.1:** Liquid culture and drop plate colony counting assay for *S. oneidensis* MR-1.

#### 4.3.4 Inductively Coupled Plasma Mass Spectrometry

Inductively coupled plasma mass spectrometry (ICP-MS) measurements of QD, bacterial cell, and QD-exposed bacterial cell samples were performed using a PerkinElmer NexION 300D single quad mass spectrometer. The Instrument Calibration Standard 2 was used to prepare calibration curves from 0.1 ppb to 1 ppm for the different ion analytes (cadmium, selenium, and zinc) which could be generated if the QDs dissolved. (There was no established protocol to measure sulfur on the instrument used.) There were 4 different sample types relevant to this chapter, and their sample preparation for ICP-MS analysis was as follows. Sample Type 1-QDs in organic solvents: QD samples at predetermined molar concentrations in chloroform were put into scintillation vials containing acetone and centrifuged to precipitate out the QDs. After allowing the QDs to dry, nitric acid was added to dissolve the samples, and then Millipore water was added to the QD-nitric acid mixtures to dilute the nitric acid concentration to 2% by volume and a total sample volume of at least 5 mL. Sample Type 2-QDs in aqueous solution: QD samples of predetermined molar concentrations were dissolved by adding concentrated nitric acid to the solutions. These aqueous QD solutions were kept at room temperature overnight. The next day, Millipore water was added to the QD-nitric acid mixtures to dilute the nitric acid concentration to 2% by volume and a total sample volume of at least 5 mL. Sample Type 3-QDs in dissolution investigations: QD solutions of known concentrations were centrifuged through 30,000 MWCO spin filtration devices at  $2,000 \times g$ . Large QD particles were trapped by the filter and the supernatants were analyzed for dissolved ion content. Sample Type 4-QDs in *Shewanella oneidensis* MR-1

association studies: Bacterial cells were cultured and exposed in liquid media as explain above in the ‘Bacterial Culture and Colony Counting’ section. After the 15-minute exposure in HEPES, the bacteria and associated QDs were harvested as pellets by centrifugation at  $2,000 \times g$  for 10 min. At this low speed of centrifugation only QDs associated to the bacterial cells were precipitated, and the free QDs in the supernatant were discarded. The QD-treated bacterial cell pellets were analyzed using ICP-MS to determine the levels of cadmium and zinc, and to confirm QDs’ association with bacterial cells.

#### 4.3.5 Cytoviva Hyperspectral Imaging

Dark-field Cytoviva hyperspectral imaging (HSI) was used to obtain images of *S. oneidensis* and QDs before and after incubations. For imaging, 3–4  $\mu\text{L}$  of sample solutions were drop-casted onto a glass slide, which was then sealed with a coverslip and clear nail polish. Slides were examined at  $100 \times$  magnification with an oil immersion lens under an Olympus BX-41 microscope. Spectral data were acquired with a Cytoviva spectrophotometer and integrated CCD camera in both the visible and near-infrared range (400–1000 nm). Analysis of the HSI spectra was performed by the Environment for Visualization software (ENVI 4.4 version). Spectral libraries of CdSe and CdSe/ZnS QDs and *S. oneidensis* MR-1 cells were used to help analyze HSI spectral angle mapper (SAM) spectral patterns and characterize the association of the QDs with bacterial cells.

#### 4.3.6 Biological Transmission Electron Microscopy

Biological transmission electron microscopy (BioTEM) images of *Shewanella oneidensis* MR-1 cells exposed to QDs were obtained using a FEI Tecnai T12 TEM

after the following preparation. *S. oneidensis* MR-1 cells were cultured in LB broth overnight. The next day, the bacterial cells were washed with DPBS buffer, diluted to an OD<sub>600</sub> of 0.8 in HEPES buffer (pH 7.4), then exposed to 0.1 mg/L selenium equivalents of CdSe/ZnS QDs for 15 min. This bacterial cell suspension was centrifuged down to a pellet, washed three times with 0.1 M sodium cacodylate buffer solution, then resuspended in a fixation buffer of 2.5% glutaraldehyde in 0.1 M sodium cacodylate buffer and fixed for 50 min. The fixed bacterial cells were centrifuged, washed with sodium cacodylate buffer, and dehydrated stepwise with increasing concentrations of ethanol (30, 50, 70, 80, 90, 95, and 100%) in water. After ethanol rinsing, the pellet was washed with propylene oxide three times. The resin infiltration steps were performed in the following manner. The pellet was soaked first in a 2:1 propylene oxide/epoxy resin mixture for 2 hr, and then in a 1:1 propylene oxide/epoxy resin mixture overnight. On the next day, the 1:1 propylene oxide/epoxy resin mixture was removed and replaced with a fresh batch of 1:1 propylene oxide/epoxy resin mixture for 5 hr, and finally incubated in a pure resin mixture and infiltrated overnight. The resin sample was then cured in a 40 °C oven for 1 day and then 60 °C oven for 2 day. A Leica UC6 microtome and a DiATOME diamond knife were used to make ultrathin sections (65 nm) of this resin-embedded bacterial sample, and uranyl acetate and lead citrate were used to stain them. These sections were placed on copper TEM grids (Ted Pella Inc.) for imaging.

#### **4.4 Reference to QDs' Synthesis, Ligand Exchange, and Liposome Interactions**

The cadmium-containing and cadmium-free QDs used in these studies are the DHLA-PEG750-OCH<sub>3</sub>-coated CdSe, ZnSe, CdSe/ZnS, ZnSe/ZnS, and Mn:ZnSe/ZnS

QDs described previously in this dissertation. Chapter 2 describes the hot injection synthesis of the QDs and their optical characteristics. Chapter 3 describes the QDs' ligand exchange which enabled their miscibility in aqueous solvents (Scheme 3.2). This current chapter aims to extrapolate the QD-liposome interactions observed in Chapter 3 to the QDs' effects on *Shewanella oneidensis* MR-1 viability. Further, QD-bacteria association was also probed since the level of QD-induced liposome membrane disruption was correlated to QD association.

#### 4.5 Investigating Cadmium-containing and Cadmium-free QDs' Association with *Shewanella oneidensis* MR-1

##### 4.5.1 Using ICP-MS to Investigate QD-Bacteria Association

Following *S. oneidensis* incubation with QDs, ICP-MS measurements of washed and digested samples were used to provide a quantitative assessment of the QDs' association with bacterial cells (Figure 4.1). Measurements of digested bacteria pellets that were incubated with 0.05 to 0.5 mg/L selenium equivalents of QDs in HEPES buffer show levels of

cadmium (from cadmium-containing QDs) and zinc (from cadmium-free QDs) that were significantly higher than the levels of these ions detected in the QD dissolution samples absent of

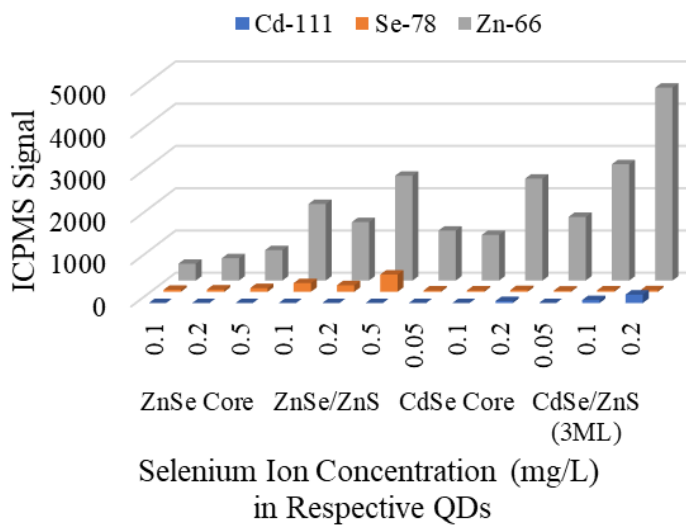


**Figure 4.1:** ICP-MS of QD-incubated bacteria exposures. (N=3; Error bars are omitted for figure clarity.)

bacteria (comparing Figure 4.1 to Figure 3.3). For example, the 0.2 mg/L selenium equivalents of CdSe/ZnS(3ML) QDs' dissolution samples (no bacteria) had a measured cadmium level of 0.01  $\mu\text{g/L}$  (Figure 3.3). However, when bacterial cells were exposed to 0.2 mg/L selenium equivalents of CdSe/ZnS(3ML) QDs the level of cadmium pelleted with the bacteria was 200  $\mu\text{g/L}$ , a 20,000-fold higher (Figure 4.1). Measuring these significantly higher levels of metals indicates that bacteria-associated QDs are being detected, and not just free ions that had dissociated from the QDs. These higher levels of cadmium and zinc in the QD-incubated bacteria provided the initial evidences of QD-bacteria association.

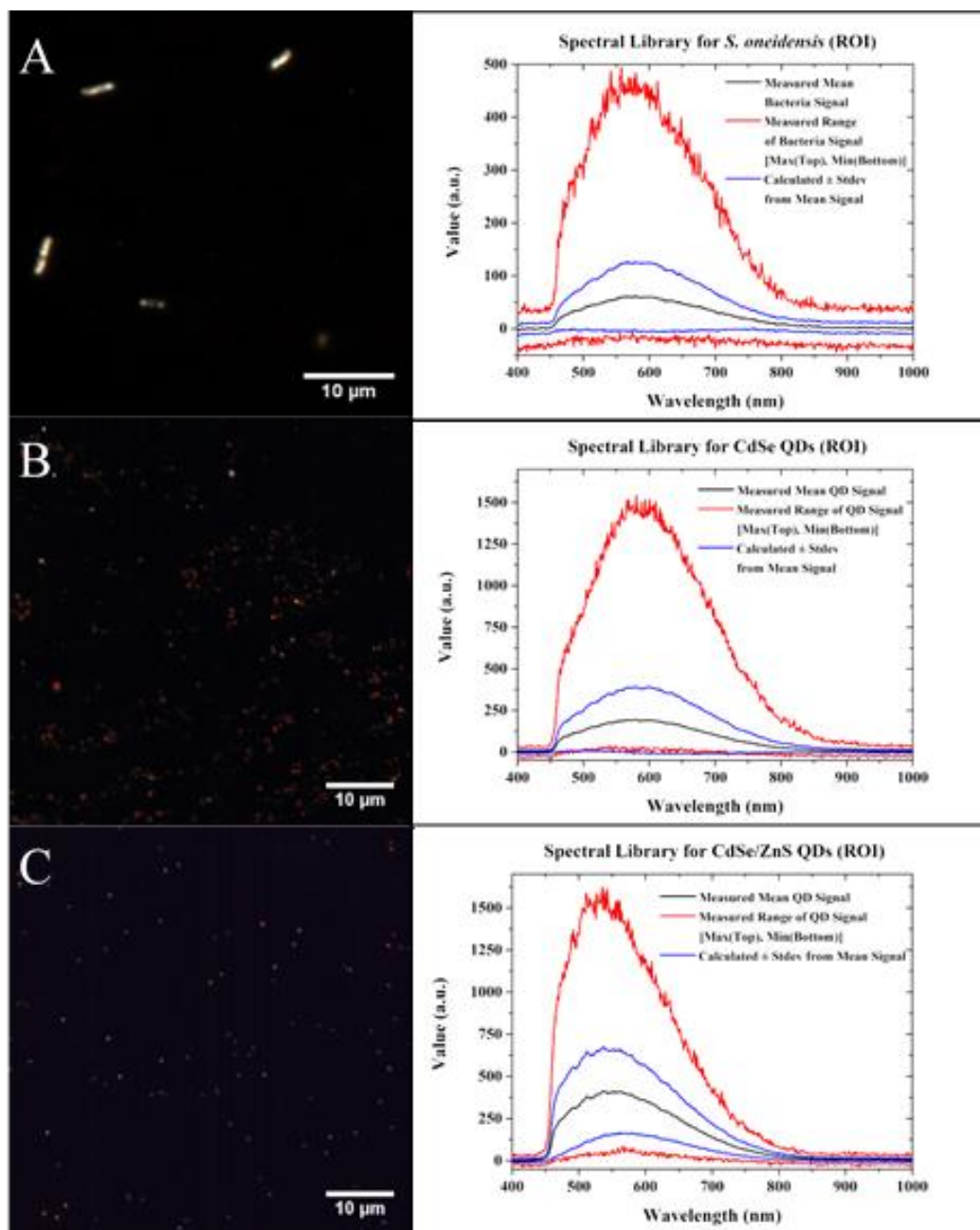
Interestingly, the levels of cadmium and zinc detected in the QD-bacteria samples which were exposed to CdSe/ZnS and ZnSe/ZnS shelled QDs were three-fold higher than the levels of cadmium and zinc in QD-bacteria samples which were exposed to CdSe and ZnSe core QDs, respectively. This higher affinity of CdSe/ZnS QDs for the bacterial cells compared to that of the CdSe core QDs is consistent with the liposome lysis assays described in Chapter 3, and further explains the increased membrane disruption of the shelled QDs. However, the higher affinity of ZnSe/ZnS QDs for bacterial cells compared to that of the ZnSe core QDs was an unexpected result considering the lower membrane disruption activity of the shelled QDs. This finding shows the limitations of using simple liposomes to model complex bacteria.

#### 4.5.2 Using Hyperspectral Imaging to Investigate QD-Bacteria Association

Hyperspectral darkfield microscopy was the first qualitative assessment used to visualize QD-bacteria association. This technique is capable of identifying and locating objects so long as they show unique optical reflectance signatures.<sup>205</sup> The

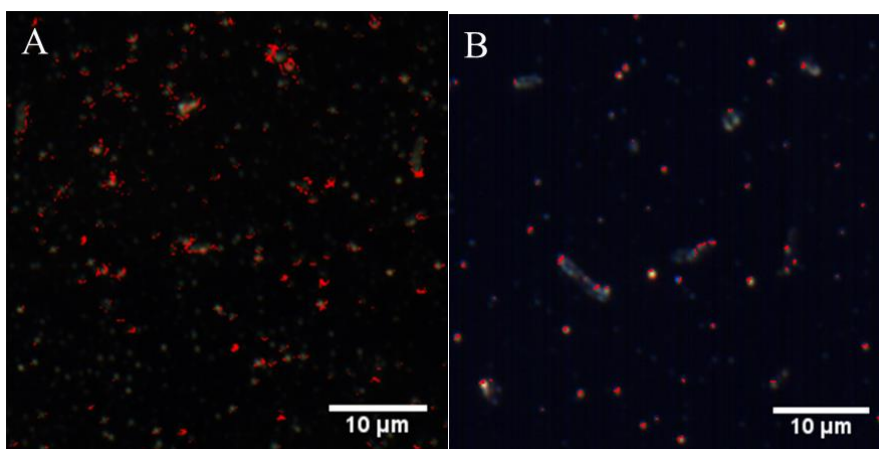
hyperspectral data cube acquisition, namely hyperspectral ‘pushbroom’ scanning, generates 3D data consisting of two spatial (x,y) dimensions and one spectral (z) dimension.<sup>206</sup> Hence, a hyperspectral image can be treated as a darkfield image with the spectral information associated with each pixel of the image.<sup>207</sup> This spectral information is built into libraries by the instrument’s region of interest (ROI) tool, which converts the pixels’ information into spectral libraries specific to the imaged object. These libraries are loaded into the spectral angle mapper (SAM) function which uses an algorithm to differentiate spectral libraries, and allows the mapping of different objects within mixed samples. Summatively, the hyperspectral imaging process includes darkfield imaging, hyperspectral data acquisition, spectral library construction, spectral library filtering, and object mapping. The method has a limited ability to localize individual QDs due to its diffraction limits, but it is able to colocalize the QDs with the much larger bacteria cells.

Figure 4.2 shows the lone object hyperspectral images (left column) of *S. oneidensis* (A), CdSe QDs (B), and CdSe/ZnS(3ML) QDs (C), and their corresponding spectral libraries (right column). The right column was built from 499 pixels for the *S. oneidensis* library, 438 pixels for the CdSe QDs’ library, and 403 pixels for the CdSe/ZnS(3ML) QDs’ library. Maximum (max), minimum (min), and mean reflectance intensity are determined from these libraries’ files. These values qualitatively demonstrate that the average reflectance intensity of the *S. oneidensis* is much lower than that of the tested QDs. In addition, cross-comparisons of the bacteria’s and QDs’ spectral libraries indicated that they were indeed unique.



**Figure 4.2:** Hyperspectral reflectance microscopy library images of *S. oneidensis* (A), CdSe QDs (B), and CdSe/ZnS(3ML) QDs (C). The QDs are false-colored red. The spectral reference libraries are shown to the right of each image. (Previously published as Figure 6 in Williams *et al.* Applied Nano Materials. 2018, 1 (9), 4788-4800.<sup>148</sup>)

Figure 4.3 shows hyperspectral images of *S. oneidensis* incubated with CdSe (A) and CdSe/ZnS(3ML) (B) QDs. The pixels representing the QDs were pseudo-colored ‘red’ after SAM analysis. The overlapping proximity of the QDs and bacterial cells is observable in both images. This proximity preliminarily supports claims of the QDs’ association with the negatively charged bacterial membranes of the *S. oneidensis*. However, the diffraction limit of this imaging technique limits the assuredness of these conclusions, as even the overlap of spectral signatures does not guarantee direct physical contact between the micron-scale bacteria (which can be resolved with this technique) and the nanoscale QDs (which cannot be resolved).



**Figure 4.3:** Images of QD-incubated bacteria which were analyzed using the reference spectral libraries in Figure 4.2. *S. oneidensis* (gray) were exposed to CdSe core (A) and CdSe/ZnS (B) QDs (red). In many cases, QDs are in the vicinity of bacteria, which is indicative of QD-membrane association. (Published as Figure 7 in Williams *et al.* Applied Nano Materials. 2018, 1 (9), 4788-4800.<sup>148</sup>)

#### 4.5.3 Using BioTEM to Investigate QD-Bacteria Association

BioTEM provided a qualitative assessment of QDs’ association with bacteria with greater resolution than the hyperspectral imaging. Representative BioTEM images of bacteria which were exposed to 0.1 mg/L selenium equivalents of ZnSe/ZnS and CdSe/ZnS QDs are shown in Figure 4.4. The low magnification used in the figure is required to view the bacteria, and only enables the observation of the

dark spots of QD aggregates associated with the cells, but not individual QDs which are only nanometers in diameter. However, these dark QD aggregate spots have been imaged at higher magnification to differentiate between QD aggregates and cell organelles (images not shown). These QD aggregates are evident in all panels and demonstrate the colocalization of QDs with the bacteria. *S. oneidensis* incubated with ZnSe/ZnS QDs (Figure 4.4 A and B) appear to maintain their expected cell shape and integrity. However, *S. oneidensis* incubated with CdSe/ZnS QDs (Figure 4.4 C and D) appear distorted—with released cell organelles and disintegrated cell membranes. The CdSe/ZnS QDs, the most disruptive QDs to liposomes and most associated with bacterial cells, appear to cause significantly more damage to the cells than ZnSe/ZnS QDs, which is consistent with our QD-liposome lysis assay results.

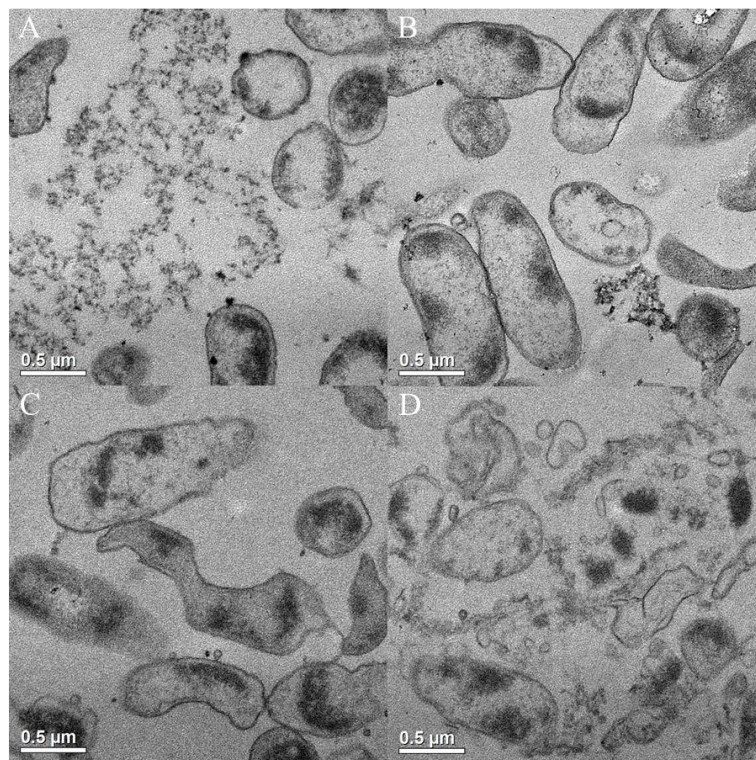


**Figure 4.4:** Representative BioTEM micrographs of *S. oneidensis* treated with ZnSe/ZnS QDs (A-B) and CdSe/ZnS QDs (C-D). Images A-B show ZnSe/ZnS QD-associated bacteria with expected cell shape and integrity. Images C-D show CdSe/ZnS QD-associated bacteria with significant cell malformations, membrane disintegration, and release of cell organelles.

## 4.6 Investigating the Impact of QDs on *Shewanella oneidensis* MR-1 Viability

### 4.6.1 Cadmium-free and Cadmium-containing QDs' Impact on Cell Viability

Having observed qualitative differences in the QDs' cell impact via BioTEM, drop plate viability studies were conducted to quantitatively assess the impact of QDs

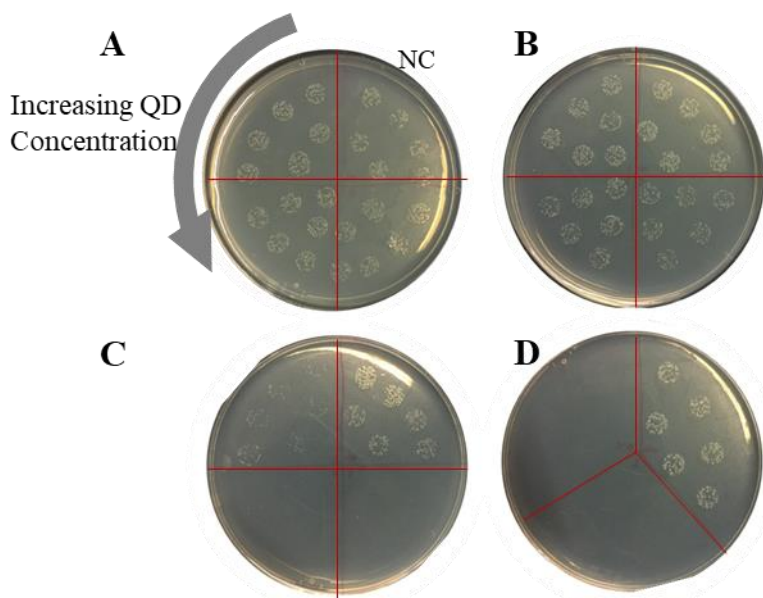


**Figure 4.5:** *S. oneidensis* colony growth after exposure to increasing concentrations of ZnSe (A), ZnSe/ZnS (B), CdSe (C), and CdSe/ZnS(3ML) (D) QDs compared to negative controls (NC, QD free bacteria) on each plate. The QD concentration increases counterclockwise around the plates.

on cell viability. Figure 4.5 shows qualitative images of bacterial cell culture plates following *S. oneidensis* exposures to increasing concentrations, ranging from 0 to 0.5 mg/L Se equivalents, of cadmium-containing and cadmium-free QDs. The ZnSe and ZnSe/ZnS QDs had negligible impact on cell

viability even at the highest tested concentration (0.5 mg/L selenium equivalents) (Figure 4.5 A and B). In contrast, exposure of *S. oneidensis* to 0.01 mg/L selenium equivalents of CdSe and CdSe/ZnS(3ML) QDs led to an almost total reduction in the measured cell viability (Figure 4.5 C and D). Colony counting was used to quantitatively assess these drop plate cultures. Figure 4.6 describes the viability of *S. oneidensis*—normalized to negative control bacteria growth—as a function of the QDs' concentration. As observed in the plates of Figure 4.5 and in the liposome assays of Figure 3.1, the cadmium-containing QDs have a greater impact on bacterial

viability than the cadmium-free QDs. Neither the ZnSe core nor ZnSe/ZnS QDs cause a reduction of *S. oneidensis*'s viability, even up to 0.5 mg/L selenium ion equivalent exposures (Figure 4.6A). However, there is an even greater decrease in viability observed with the CdSe/ZnS(3ML) QDs compared to the evident decrease in viability caused by the CdSe core QDs (Figure 4.6B). These results support the hypothesis that the substitution of the cadmium core for a zinc core can reduce the toxicity of QDs against model environmental organisms without further modification of the QD system. However, as was similarly concluded in the liposome studies, these results do not support the hypothesis that coating the cadmium-containing QDs with a ZnS shell could mitigate viability impacts.

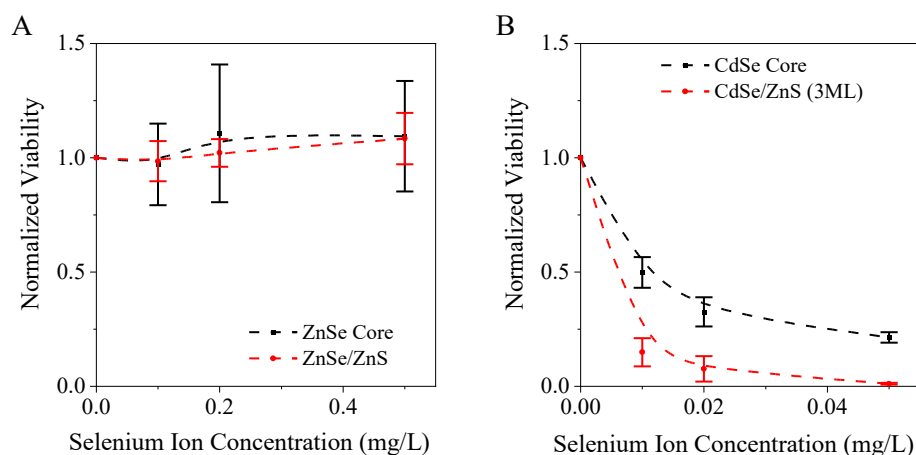


**Figure 4.6:** Normalized *S. oneidensis* viability as a function of ZnSe and ZnSe/ZnS QDs' (A) and CdSe and CdSe/ZnS(3ML) QDs' (B) concentration. (N=4; Note the different x-axis scales.)

#### 4.6.2 Additional Modifications Which Impact QDs' Viability Implications

We investigated the impact of CdSe/ZnS QDs with varying shell thickness on the viability of *S. oneidensis*. Figure 4.7 describes the normalized bacterial cell viability as a function of the CdSe/ZnS QDs' concentration (in selenium equivalents) for CdSe QDs (black) and CdSe/ZnS QDs with shell thickness of one ML (red), three

ML (blue), and six ML (green). As with the liposome lysis studies, a greater decrease in bacterial viability is observed for the cadmium-containing QDs as the ZnS shell thickness increases. These results are indicative of the complex nature of the interactions between luminescent QDs and bacteria. On one hand, passivating

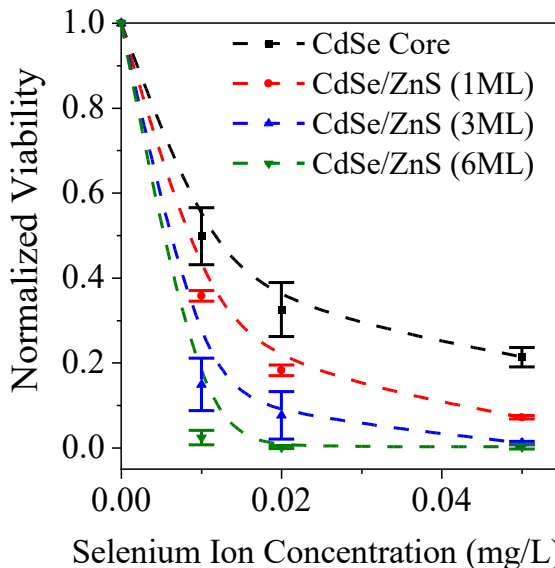


**Figure 4.7:** Normalized *S. oneidensis* viability after exposure to CdSe/ZnS QDs of increasing shell thickness. (N=4)

CdSe QDs with a higher energy bandgap shell of ZnS is known to decrease the rate of ROS generation when irradiated and lower their toxicity.<sup>27, 29, 51, 161</sup> On the other hand, the chemical instability of the shell due to crystal plane mismatches along the core/shell interface<sup>208, 209</sup>, particularly in complex aqueous solutions, increases their rate of zinc ion dissolution and increases QDs' toxicity against the *Shewanella oneidensis* MR-1 bacterium.

We also investigated the impact of manganese doping in ZnSe/ZnS QDs (Mn:ZnSe/ZnS) on *S. oneidensis* viability. This was investigated since transition metal doping is often used to red shift the optical properties of ZnSe QDs.<sup>14, 173, 174, 210</sup> Additionally, Mn is often used for doping and has known beneficial effects on the viability of *S. oneidensis* due to this bacterium's ability to reduce it for metabolic purposes.<sup>43, 172, 174, 203</sup> Specifically, 0.4 mmol of manganese stearate and 0.6 mmol of zinc stearate was used to make the Mn:ZnSe core which was then shelled with the same size ZnS shell as the undoped ZnSe core QDs. *S. oneidensis* exposed to

increasing concentrations of the Mn:ZnSe/ZnS QDs observed a concentration-dependent stimulated growth compared to the negative control bacteria (Figure 4.8). In the literature, this phenomenon has been owed to the specific manganese reducing capabilities of the MR-1 strain used in this study.<sup>172, 203</sup>

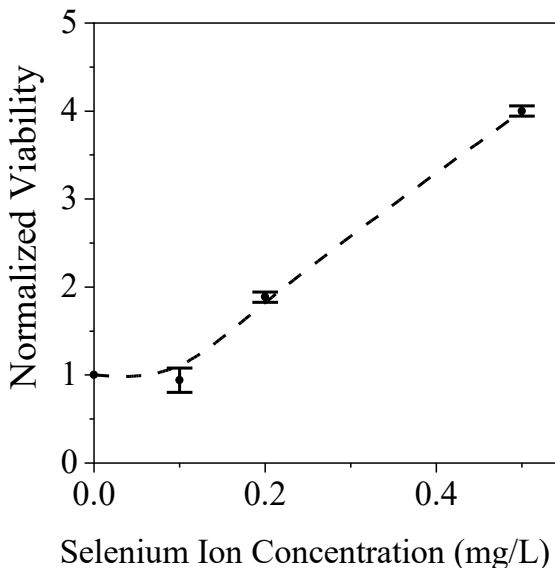


**Figure 4.8:** Normalized *S. oneidensis* viability after exposure to Mn:ZnSe/ZnS QDs. (N=3)

Lastly, we investigated the viability of *S. oneidensis* with exposures to ligand and ion controls. The DHLA-PEG-OCH<sub>3</sub> ligands alone did not significantly impact the viability of *S. oneidensis* (data not shown). Salts which would readily generate Cd<sup>2+</sup>, Zn<sup>2+</sup>, and Se<sup>4+</sup> were chosen to conduct ion control exposures as these are the predominately expected oxidation states on these ions in water.<sup>187, 188</sup> Appendix Figures 4.1 shows the results of the *S. oneidensis* ion control exposures. The cadmium ion control did not result in any significant decrease in bacterial cell viability until 2 mg/L, the amount of cadmium in about 0.2 mg/L selenium equivalents of CdSe and CdSe/ZnS QDs as determined by ICP-MS. The relevant concentrations for selenium ion controls never caused a significant decrease in cell viability for the bacteria. The zinc ion controls resulted in significant decreases in bacterial cell viability only at concentrations relevant to shelled CdSe and ZnSe QDs. The impact of these zinc ion controls on *S. oneidensis* and the previously demonstrated dissolution of the ZnS

from shelled CdSe QDs may explain the increased impact of CdSe/ZnS QDs compared to all other QDs in this study.

#### 4.7 Conclusions

These studies support the findings of the liposome assays with cadmium-containing and cadmium-free QDs in Chapter 3, and exemplify the relevance of QDs' semiconductor material and structure for their environmental implications. ICP-MS, hyperspectral imaging, and BioTEM measurements suggest that all tested QDs associate with *Shewanella oneidensis* MR-1 cells. After this association, the cadmium-free ZnSe and ZnSe/ZnS QDs minimally impact the viability of the cells, while the cadmium-containing CdSe and CdSe/ZnS QDs significantly reduce their viability. Surprisingly, shelling the CdSe core QDs with a ZnS shell increases—rather than decreases—the impact of these QDs on bacterial cell cultures. These are unwelcome findings, since it is generally accepted that shelling cadmium-containing QDs with a ZnS shell should lower QD toxicity due to a reduced rate of ROS generation and a mitigating layer between the toxic material containing core and essential organisms.

The increased viability impact from the CdSe/ZnS QDs can be attributed to the increased affinity and association between these QDs and bacterial cells, and to the increasing the chemical instability of these QDs as their shell size grows—due to the crystal plane mismatches—which lends to a high rate of shell dissolution from the QDs. The dissolution of the ZnS shell while the CdSe/ZnS QDs are associated to bacteria lends to a high concentration of zinc ions near the membrane, which additionally destabilizes the bacteria and lends to greater viability impacts. Further, the

ion control experiments show that even if the most impactful CdSe/ZnS QDs are completely dissolved in solution, the resulting ion levels are not sufficient to induce the level of viability impact we observe with the QD incubations. This highlights that the impacts in this study are QD structure specific, rather than just relevant to the metals used.

## Chapter 5: Investigating the Activity of Polymer- and Peptide-coated CdTe QDs with Human Health Cell Models.

*This chapter includes text and figures that are a modified reproduction of work published in Williams et al. Poly(oxanorbornene)-Coated CdTe Quantum Dots as Antibacterial Agents. ACS Applied Bio Materials. 2020, 3 (2), 1097–1104.<sup>149</sup>*

### 5.1 Purpose

This chapter discusses the investigation of the antibacterial and hemolytic activity of novel peptide- and polymer-conjugated QDs, and their potential to be synergistic antibacterial entities. The peptide, polymer series, and QDs used were specifically chosen because of their demonstrated antimicrobial activity and selectivity. The LL-37 peptide is a naturally occurring, human-derived antimicrobial peptide which has a demonstrated preference for interacting with pathogenic microbes over mammalian cells. The synthetic poly(oxanorbornene) (PON) polymers are mimics of antimicrobial peptides which have demonstrated tunable, broad-spectrum antibacterial activity. The CdTe core QDs have demonstrated light-activated antibacterial activity against multidrug resistant bacteria. These entities were used to the hypothesis that conjugated PONs-QD and peptide-QD treatments would result in synergistic light-activatable antibacterial activity due to the combination of the coatings' and QDs' varying antibacterial mechanisms of action.

### 5.2 Introduction

Globally, health organizations have deemed drug-resistant organisms to be amongst the top threats to human health, with multidrug-resistant (MDR) bacteria being of the greatest concern since they have the greatest mortality and morbidity

rates.<sup>87, 211</sup> In the US alone, the U.S. Centers for Disease Controls and Prevention estimate that more than 2.8 million people are infected with various MDR bacteria each year, which leads to about 35 thousand deaths.<sup>88</sup> Additionally, the occurrence of MDR bacterial infections is especially concerning considering the ESKAPE (*Enterococcus faecium*, *Staphylococcus aureus*, *Klebsiella pneumoniae*, *Acinetobacter baumannii*, *Pseudomonas aeruginosa*, and the *Enterobacter* species) list of hospital-acquired bacterial infections; which accounts for the majority of hospital-acquired infections in general.<sup>100, 101</sup> More than 15% of ESKAPE infections are MDR, which has owed hospital-acquired bacterial infections an estimated 6-10% death rate every year since 2002, globally.<sup>98, 101-104</sup> The high occurrences of drug-resistant bacteria are being attributed to: 1) the fact 60% of food industry antibiotics are also being used for human treatment, 2) the improper and over prescription of antibiotics, and 3) the improper and self-prescribed use of antibiotics.<sup>86, 87, 212</sup>

The overwhelming and increasing occurrences of drug-resistant bacterial infections intensify the need for the development of new antibacterial agents. Despite this need, the slow development of traditional small molecule antibiotic candidates is not successfully filling the clinical pipeline with promising drug candidates.<sup>106</sup> So, while research into new classes of these traditional antibacterial molecules is ongoing, concurrently, there are increasing studies aimed at developing nontraditional antibacterial agents. Antibacterial polymer, peptide and nanoparticle conjugates are some of the nontraditional antibacterial agents currently under investigation for potential use in hospital and dentistry settings—where antibacterial surface and wound treatments are essential to preventing the spread of drug-resistant bacteria

between immune compromised patients.<sup>115, 213, 214</sup> As with molecular antibiotics, the literature has shown that these alternatives have the greatest clinical outcomes if they are multitargeting, can inhibit bacteria from mounting self-defense mechanisms, and are not readily recognized by efflux pumps.<sup>140</sup>

In general, the conjugation of antibacterial entities to nanoparticles has led to mixed outcomes. The conjugates range between being synergistic, effective treatments toward a specific bacterial target, and being completely antagonistic with the properties of the surface-bound antibacterial being disrupted by the conjugation.<sup>25, 31, 37, 44, 50, 131, 140, 141, 215, 216</sup> Broad-spectrum, synergistic activity has been realized by conjugating functionalized thiol molecules<sup>140</sup>, cationic peptides<sup>131</sup>, the photosynthesizer toluidine blue O<sup>37</sup>, small molecule antibiotics (such as vancomycin<sup>25</sup>, ceftriaxone<sup>31</sup>, polymyxin-B<sup>50</sup>, indolicidin<sup>44</sup>, and penicillin<sup>141</sup>), and other antibacterial entities to different nanomaterials. The observed synergism is typically the result of 1) the combination of the nanoparticles' inherent activity with the activity of their antibacterial coating, 2) the high localized delivery of the conjugated antibacterial molecules to the bacterial targets, and 3) the reorganization of the surface antibacterial agent into a conformation with increased antibacterial activity after conjugation to the nanoparticles' surface. In contrast, there are other examples where conjugating antibacterial agents to nanoparticles has diminished their antibacterial activity. For example, zinc oxide nanoparticles have been shown to decrease the activity of amoxicillin, penicillin, nitrofurantoin, vancomycin, and carbenicillin against *S. aureus* and the activity of erythromycin against *E. coli*.<sup>215, 216</sup> Other potential problems with the conjugation of antibacterial molecules to

nanoparticles include a decreased uptake rate and the emergence of off-target toxicity which is introduced by the nanoparticles.<sup>216</sup>

In this chapter, the antibacterial activity of CdTe QDs is combined with the antibacterial mechanisms of cationic polymers and peptides through direct conjugation. CdTe core QDs—with a bandgap of 2.4 eV—were chosen as they have well studied broad-spectrum antibacterial activity in the dark, which can be enhanced by direct irradiation

due to light-induced increased generation of the ROS responsible for their anticellular activity.<sup>47</sup> LL-37 (Figure 5.1), a 37 amino acid cationic segment of the human Cathelicidin peptide, was chosen for its documented activity against a broad-spectrum of bacteria, viruses, fungus, parasites, biofilms, and enzymes.<sup>112, 125, 217, 218</sup> The non-cell selective activity of this antimicrobial peptide is correlated to its structure and association behavior at neutral pH. Upon association with zwitterionic lipid membranes, this peptide forms a tetramer which burrows and forms cell lysis-inducing membrane pores.<sup>121, 219</sup> Upon electrostatic association with anionic membranes, this peptide adopts a disordered C-terminal which ‘carpets’ and destabilizes the membrane to induce cell lysis.<sup>1, 219</sup> The poly(oxanorbornene)-based synthetic mimics of antimicrobial peptides, or PONs, are facially amphiphilic polymers with tunable hydrophobicity due to varying combinations of a charged ammonium-terminated side chain and a hydrophobic alkyl side chain in each repeat unit (Figure 5.2; Synthesis discussion is in the Appendix.).<sup>220</sup> The polymers’ mechanism of antibacterial activity involves the

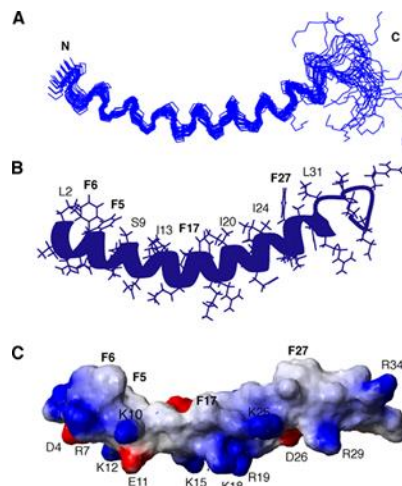


**Figure 5.1:** The solution structure of human LL-37 shown as an ensemble of 28 out of 200 backbone residues (A), a ribbon representation with the hydrophobic side chains labeled (B), and a potential energy surface (C).

positive side chains of the molecules attracting them to the negatively charged bacterial outer envelope, and then the alkyl side chains potentially partitioning into the membrane's hydrophobic interior.<sup>221</sup> PONs of appropriate amphiphilicity have shown selective, broad-spectrum activity against bacteria as free molecules and surface-attached polymer

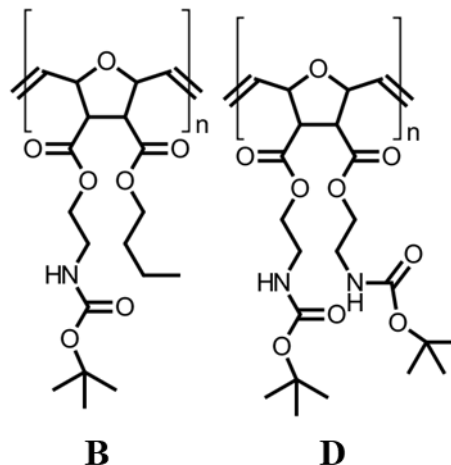


**Figure 5.2:** Structure of the BOC-protected butyl amine (B) and diamine (D) oxanorbornene monomers.

networks.<sup>115, 127, 214, 221-224</sup> Further, a recent study in our lab with PONs-conjugated gold nanoparticles has shown that their conjugation to nanoparticles enhances their membrane penetration activity.<sup>177</sup>

We hypothesized that the cationic LL-37 and PONs surface coatings would facilitate the association of peptide-QD and PONs-QD conjugates with bacterial cells. After association, the surface coatings could act at the cell surface to disrupt the membrane and the CdTe QDs would generate ROS in close proximity to cell membranes and organelles in order to induce bacterial cell death. Further, we hypothesized that 1) the activity of all conjugates could be enhanced by direct irradiation and that 2) varying the amine content of PONs would affect the activity of PONs-QD conjugates.

### 5.3 Materials, Instrumentation, and Methods

#### 5.3.1 Materials and Reagents

2-(N-morpholino)ethanesulfonic acid (MES) buffer (1.0 M) was purchased from Alfa Aesar. LL-37 (antimicrobial peptide, human) was purchased from

Anaspec, Inc. Tris buffer was purchased from AppliChem. Sterile water was either purchased from BBraun or prepared by autoclaving Millipore water. Mueller Hinton Broth (MHB) was purchased from BD Difco. An Ultrathin LED Light Panel (Neutral White) was purchased from Environmental Lights (San Diego, CA). EDTA-blood was either drawn fresh every day of assay from an approved volunteer or purchased from Innovative Research, Inc. (Michigan, U.S.). *E. coli* (Strain ATCC25922) and *S. aureus* (Strain ATCC6538) cells were purchased from the Leibniz-Institute DSMZ. 1-ethyl-3-(3-(dimethylamino)propyl) carbodiimide (EDC), 2',7'-dichlorofluorescein (H<sub>2</sub>DCF), Tris(hydroxymethyl)aminomethane acetate-ethylenediaminetetraacetic acid (Tris-EDTA) buffer, and Triton X-100 were purchased from Sigma-Aldrich. Poly(oxanorbornenes) (PONs) were synthesized and characterized as previously reported.<sup>220, 222</sup> These synthesis details are reported in the Appendix.

### 5.3.2 Ethics Statement

Red blood cells that were drawn the day of some hemolytic assays were obtained from human volunteers who had previously given their written consent according to the Helsinki declaration, which was approved by the Ethics Board of the Albert-Ludwigs University, Freiburg, Germany.

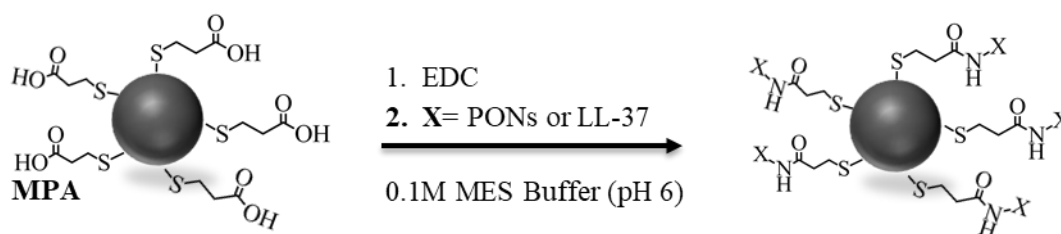
### 5.3.3 Instrumentation

Hydrodynamic size and zeta potential were measured using the Malvern Zetasizer Nano ZS instrument. The PerkinElmer Pyris 1 instrument was used to conduct thermogravimetric analysis. UV/Vis absorption spectra were obtained using a Thermo Scientific Evolution 201 UV/Vis spectrophotometer. Fluorescence spectroscopy measurements were performed using a PTI-Horiba QuantaMaster 400

fluorimeter. A Molecular Devices SpectraMax M5 Microplate reader was also used to measure changes in absorbance and fluorescence intensity over time.

#### 5.3.4 Coupling LL-37 and PONS to MPA-CdTe QDs

LL-37 and PONS were conjugated to the MPA-QDs' surface via EDC methods, similar to a PONS coupling procedure reported for gold nanoparticles (Scheme 5.1).<sup>177</sup> In a 20 mL vial with a stir bar, 10 nmol of purified CdTe cores and 1.4  $\mu\text{mol}$  of LL-37 or PONS were combined in 3 mL of 0.1 M MES buffer (pH 5). While stirring, 10  $\mu\text{mol}$  of EDC was added to the solution. The reaction was stirred overnight and then ran through a pre-rinsed 30,000 MWCO centrifugal filter, at 2,000  $\times$  g, to rid of excess reactants. The conjugates were suspended in fresh 0.1 M MES buffer and stored in the fridge and protected from light until use.



**Scheme 5.1:** Conjugation of poly(oxanorbornenes) and LL-37 peptides to CdTe quantum dots.

#### 5.3.5 H<sub>2</sub>DCF Fluorescence Assay for Detection of ROS

H<sub>2</sub>DCF was used to detect the inherent ROS generation of the MPA-QDs and PONS-QDs following the procedures of a previously reported cell-free assay.<sup>225</sup> A 50  $\mu\text{M}$  H<sub>2</sub>DCF in Millipore water solution was prepared under inert gas. In 96 well plates, duplicate wells with 100  $\mu\text{L}$  of 50  $\mu\text{M}$  H<sub>2</sub>DCF, 90  $\mu\text{L}$  of Millipore water, and 10  $\mu\text{L}$  of the respective MPA-QDs and PONS-QDs samples were prepared. Concentrations for the PONS-QDs ranged from 6.25 to 400  $\mu\text{g}/\text{mL}$  PONS equivalents, and MPA-QDs equivalents in both the PONS- and MPA-QDs samples ranged from

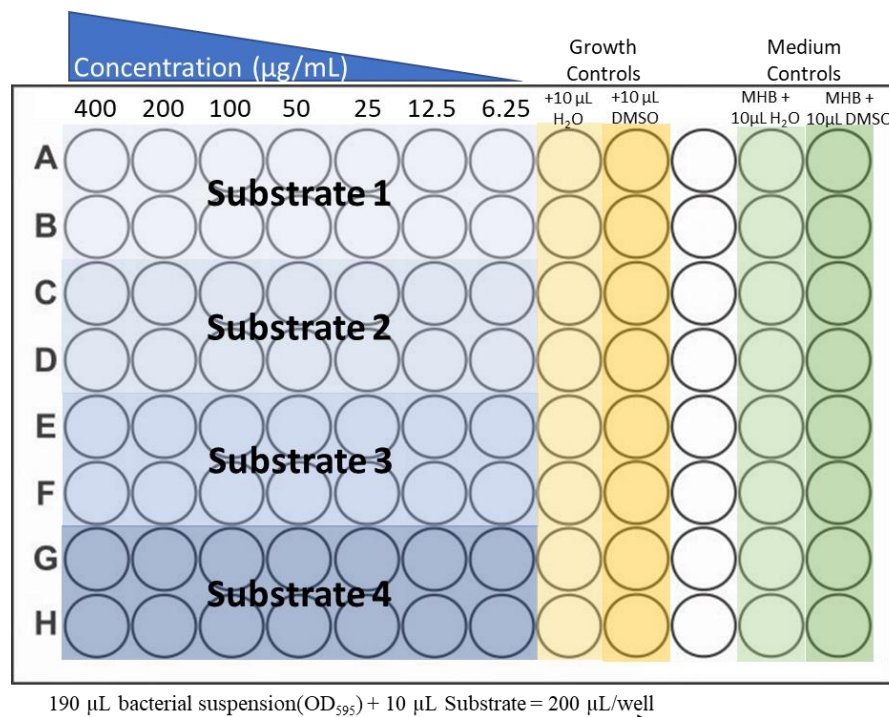
12.5 to 800 nM in these wells. ROS generated from MPA-QDs and PONs-QDs, with and without irradiation with a neutral white LED plate, was detected in relative fluorescence units using a Molecular Devices SpectraMax M5 Microplate reader with  $\lambda_{\text{ex}}$ : 495 nm and  $\lambda_{\text{em}}$ : 500–600 nm. An initial reading was taken and followed by a reading every hour for 6 hr in the plate reader. These readings were also measured with a PTI-Horiba QuantaMaster 400 fluorimeter under the same conditions for MPA-QDs and H<sub>2</sub>DCF control samples.

#### 5.3.6 Thermogravimetric Analysis (TGA) of MPA-QDs and QD Conjugates

Prior to TGA, MPA-QDs and QDs conjugates were pelleted via centrifugation at  $2,000 \times g$  for 5 min in order for the supernatant to be removed. The pellets were suspended in minimal Millipore water for transfer to a TGA heating pan, which was placed into a PerkinElmer Pyris 1 TGA instrument. The pan was heated for 15 min at 100 °C to evaporate the water. Then the temperature was ramped from 100 to 900 °C at 25 °C/min. The mass loss between 100 and 700 °C was used to determine the total amount of MPA, LL-37, and PONs originally on the QD surface. All mass values were normalized to the mass at 700 °C, a temperature where all organic content is desorbed from the QD surface, for analysis.

#### 5.3.7 Minimum Inhibitory Concentration (MIC) Assay with Bacteria

*E. coli* and *S. aureus* suspension cultures were inoculated in 5 mL of MHB the day before conducting the MIC assays. After shaking overnight at 37 °C, 500  $\mu\text{L}$  of the bacterial suspension were transferred to an Eppendorf tube and centrifuged at 8,000 rpm for 1.5 min. The supernatant was removed, and the bacterial pellet was



**Scheme 5.2:** Example 96 well plate layout for one biological replicate of the bacterial MIC assay. (Note: Empty wells were filled with 200 uL of sterile water.)

resuspended in fresh MHB. These washed cells were diluted to a final OD<sub>595</sub> of 0.001—corresponding to a bacterial concentration of about 10<sup>6</sup> cells/mL.

The bacterial MIC assays were performed with controls and varying concentrations of the substrates in a MHB system (pH 7.3), in 96 well plates (Scheme 5.2). First, 10 µL of polymers, peptides, MPA-QDs, QD conjugates, and controls—at prepared stock concentrations—were pipetted into the wells in duplicate. (One duplicate = one biological replicate.) Then, 190 µL of the washed bacterial cells or control solvents were transferred to each appropriate well in the plates. MES buffer and DMSO were tested with bacteria to ensure the solvents alone did not influence bacteria growth. MHB alone, and with DMSO and MES buffer were tested as negative controls. The final well concentrations ranged from 6.25 to 400 µg/mL PONs equivalents for the free PONs and PONs-QDs samples, from 1.25 to 80 µg/mL

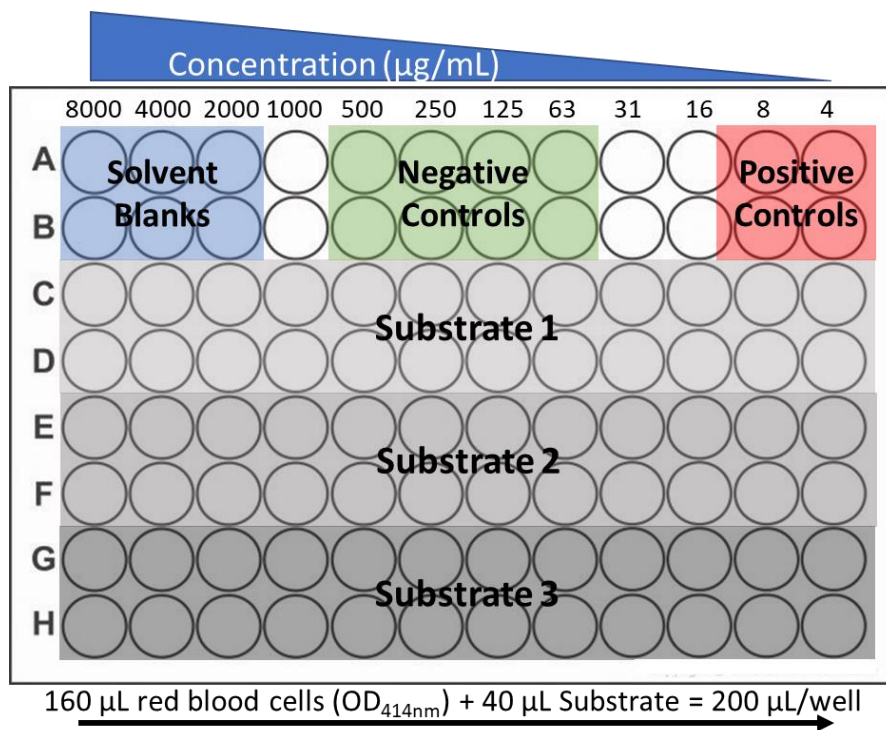
LL-37 equivalents for the free peptides and peptide-QDs samples, and from 0.001 to 1  $\mu\text{M}$  QD equivalents for the MPA-QDs and QD conjugate samples. The plates were mixed well before being placed into a 37 °C incubator. For exposures with irradiation, plates were rested directly on top of the neutral white light LED plate for 2 hr at the beginning of the incubation in the 37 °C incubator. After incubating overnight, the OD<sub>595</sub> was evaluated to quantify bacteria cell viability. The percent cell growth was calculated via the equation:

$$\text{Percent Cell Growth} = \left( \frac{\text{OD}_{595, \text{Substrate}} - \text{OD}_{595, \text{Medium Control}}}{\text{OD}_{595, \text{Growth Control}} - \text{OD}_{595, \text{Medium Control}}} \right) \times 100$$

#### 5.3.8 Hemolysis Assay

Red blood cells (RBCs) were either purchased or harvested from a volunteer the morning of hemolysis assays and preserved in Tris-EDTA. Per 96 well plate, 30  $\mu\text{L}$  of EDTA-blood in 10 mL of Tris buffer was centrifuged at 3,000 rpm for 5 min. The supernatant was removed from the RBC pellet. Ten mL of Tris buffer was added to resuspend the pellet, and this washing was repeated for three total wash and resuspension cycles. The number of RBCs was counted using a Neubauer chamber to check for blood quality.

Hemolysis assays were performed with controls and varying concentrations of the substrates in a Tris buffer system (pH 7.0), in 96 well plates (Scheme 5.3). First, 40  $\mu\text{L}$  of the controls or substrates—at prepared stock concentrations—were added to wells in duplicate. (One duplicate = one biological replicate.) Then, 160  $\mu\text{L}$  of the RBCs in Tris buffer solution or solvent controls were added to each sample well; for a total well volume of 200  $\mu\text{L}$ . A 10% Triton-X solution was used as positive control in this assay. Aqua, MES buffer and DMSO were used as negative controls. Tris



**Scheme 5.3:** Example 96 well plate layout for one biological replicate of the hemolysis assay.

buffer was tested as a solution blank. The final well concentrations of free PONs and PONs-QDs samples ranged from 0.1 to 8,000 µg/mL PONs equivalents. The final well concentrations of free peptide and peptide-QDs ranged from 0.15 to 80 µg/mL. The final well concentrations of MPA-QDs and QD conjugate samples ranged from 0.001 to 10 µM QD equivalents. The plates were incubated at 30 °C for 30 min, and then centrifuged at 3,000 rpm for 5 min. For exposures with irradiation, plates were rested directly on top of the neutral white light LED plate for the entire incubation period. 100 µL of the wells' supernatant was transferred via multichannel pipet to new plates for OD<sub>414</sub> measurements, which was used to quantify the amount of RBC lysis. The percent RBC lysis was calculated via the equation:

$$\text{Percent Hemolysis} = \left( \frac{\text{OD}_{414, \text{Substrate}} - \text{OD}_{414, \text{Solvent Blank}}}{\text{OD}_{414, \text{Positive Control}} - \text{OD}_{414, \text{Solvent Blank}}} \right) \times 100$$

## 5.4 Investigating the Activity of MPA-coated CdTe Core QDs

### 5.4.1 Reactive Oxygen Species Generation of CdTe QDs

Luminescent mercaptopropionic acid-coated (MPA-) CdTe QDs were synthesized as aqueous-miscible colloids via microwave methods, as described in Chapter 2. In addition to the optical and physical characterization previously described, the reactive oxygen species (ROS) generation from the MPA-CdTe QDs was characterized since this is the predominant antibacterial mechanism of action for semiconductor nanomaterials like CdTe QDs. For this, the oxidation-dependent changes in the fluorescence spectrum of the minimally fluorescent 2',7'-dichlorodihydrofluorescein (H<sub>2</sub>DCF) molecule oxidizing into the highly fluorescent 2',7'-dichlorofluorescein (DCF) molecule was evaluated (Figure 5.3). Figure 5.3A shows a fluorescence emission spectrum of H<sub>2</sub>DCF at  $t \approx 0$  ( $\lambda_{\text{ex}} = 495$  nm, black) compared to a spectrum at  $t = 6$  hr ( $\lambda_{\text{ex}} = 495$  nm, red)—when the dye has been oxidized to DCF by air exposure. Figure 5.3B shows the rate of H<sub>2</sub>DCF oxidation by

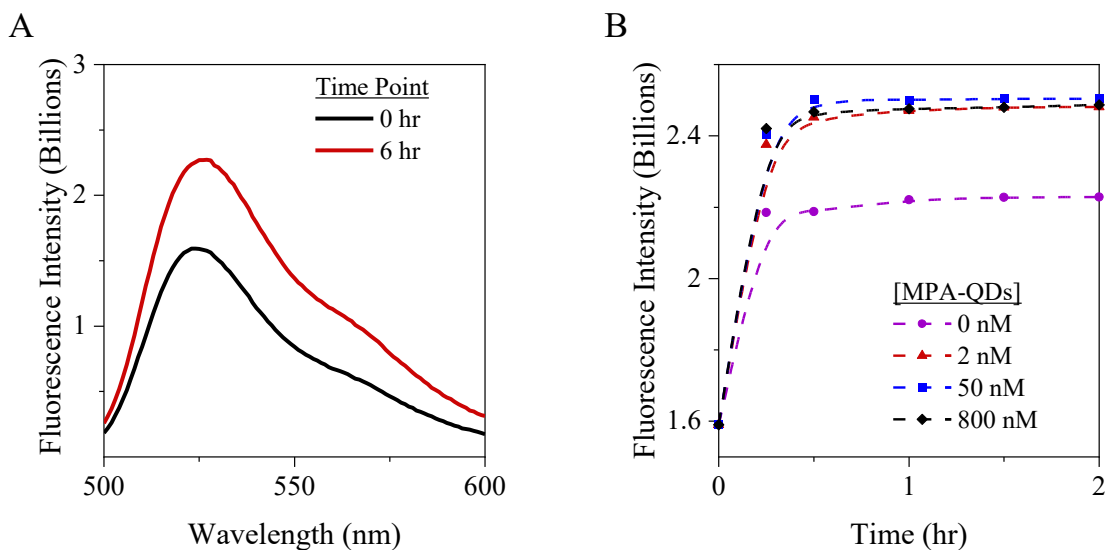


**Figure 5.3:** Fluorescence emission profile of H<sub>2</sub>DCF ( $t = 0$ , black) compared to the air-oxidation derived DCF ( $t = 6$  hr, red) ( $\lambda_{\text{ex}} = 495$  nm) (A). The rate of the oxidative ROS generation with increasing MPA-QDs concentration is faster than air oxidation of H<sub>2</sub>DCF samples ( $\lambda_{\text{ex}} = 495$  nm,  $\lambda_{\text{em}} = 525$  nm,  $N = 3$ ) (B).

air alone as a control (purple) and with increasing concentrations of the free MPA-QDs through monitoring the emission intensity at the emission peak wavelength of 525 nm. The emission increase of the control sample indicates a slow oxidation of H<sub>2</sub>DCF to DCF under these experimental conditions. MPA-QDs increase the rate of H<sub>2</sub>DCF oxidation, with the greatest change happening between 0 and 15 min. There are also minimal increases in the rate of QD ROS-induced oxidation with increasing QD concentration within this time frame. After 30 min, the oxidation of the available H<sub>2</sub>DCF by the MPA-QDs is complete, as indicated by the fluorescence of DCF reaching its maximum intensity.

#### 5.4.2 Biological Characterization of MPA-CdTe QDs

Figure 5.4 describes the activity of MPA-QDs against *E. coli*, *S. aureus*, and RBCs with and without direct broad white light irradiation from a neutral white LED light panel. The panel's emission spectrum is shown in Appendix Figure 5.4. Figure 5.4A describes the antibacterial activity of the MPA-QDs. MPA-QD treatments, with (red) and without (black) irradiation, have concentration dependent activity against *E. coli* growth. This light-enhanced antigrowth activity of the QDs is what we aim to combine with the membrane-penetration activity of the PONs molecules in the PONs-QDs conjugates. *S. aureus* is not affected by nonirradiated treatments of MPA-QDs (blue). Irradiated MPA-QDs vs. *S. aureus* data was not collected due to the lack of QD conjugates' activity against *S. aureus*, as discussed later in this chapter. Figure 5.4B shows that the MPA-QDs had negligible hemolytic activity without direct irradiation. Further, irradiation had no significant effects on this hemolytic activity (data not shown).

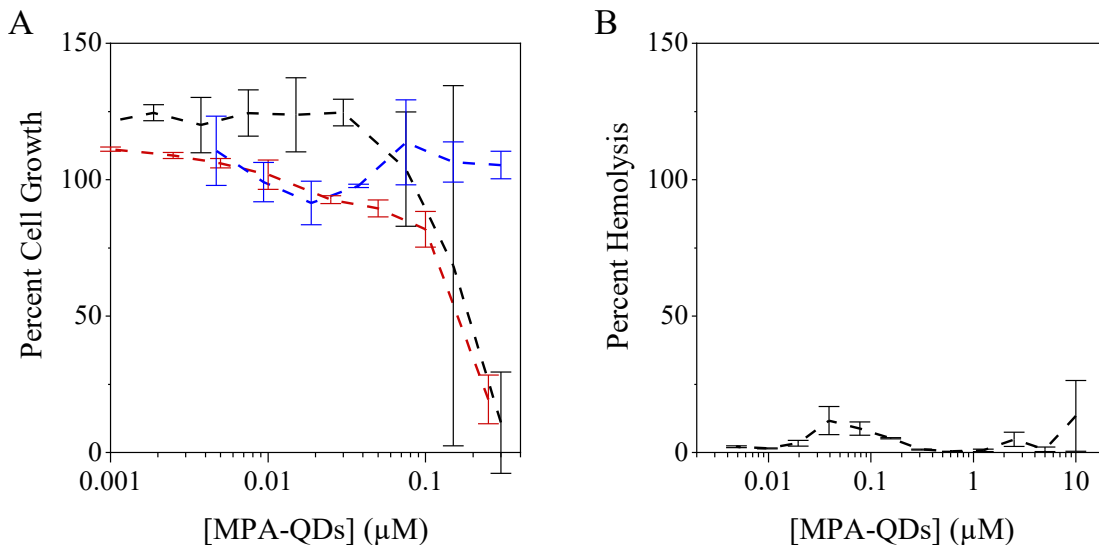


**Figure 5.4:** MPA-QDs cause a concentration dependent decrease in *E. coli* cell growth with (red) and without (black) irradiation, but do not affect *S. aureus* cell growth (blue) at tested concentrations(A). The MPA-QDs had no significant hemolytic activity at tested concentrations (B). (N $\geq$ 3 biological replicates.)

## 5.5 Investigating the Activity of PONs-coated CdTe QDs

### 5.5.1 Characterization of PONs-CdTe QDs

$\zeta$ -potential measurements were used to preliminarily determine if the PONs series was conjugated to the MPA-QDs. Figure 5.5A shows that prior to conjugation, the MPA-QDs were negatively charged with a  $\zeta$ -potential of  $-38$  mV. Following conjugation, the  $\zeta$ -potential values of PONs-QDs ranged between  $+15$  and  $+30$  mV, which confirms the conjugation of the positively charged PONs to the MPA-QDs.

Thermogravimetric analysis (TGA) measurements before and after PONs conjugation were used to determine the amount of MPA and PONs on the CdTe QDs' surface. The TGA traces of MPA-QDs (purple) and PONs-QDs with PONs of varying amine/alkyl ratio (red, black, green, and blue; in order of increasing amine content) are shown in Figure 5.5B. MPA-QDs showed a mass loss of  $29 \pm 2\%$  between 100 and 700 °C due to the desorption of MPA molecules from the QDs'

surfaces. When correcting for the  $29 \pm 2\%$  mass loss due to the loss of MPA from the QDs, the mass losses due to the loss of PONs from the PONs-QDs were  $54 \pm 8\%$  for the 55% amine PONs (red),  $50 \pm 8\%$  for the 75% amine PONs (black),  $51 \pm 5\%$  for the 95% amine PONs (green), and  $51 \pm 2\%$  for the 100% amine PONs (blue). These values indicate that the surface coverage of PONs on the QDs does not vary significantly even though the PONs have varying amine/alkyl side chain ratios. This contrasts with the previously observed significant dependence of PONs' surface coverage on their amine/alkyl ratio when conjugated to 30 nm diameter gold nanoparticles.<sup>177</sup> These findings suggest that the ratio between the polymer length and the diameter of the nanoparticles also affects the polymers' surface coverage of nanoparticles. Since the PONs surface coverage on our CdTe

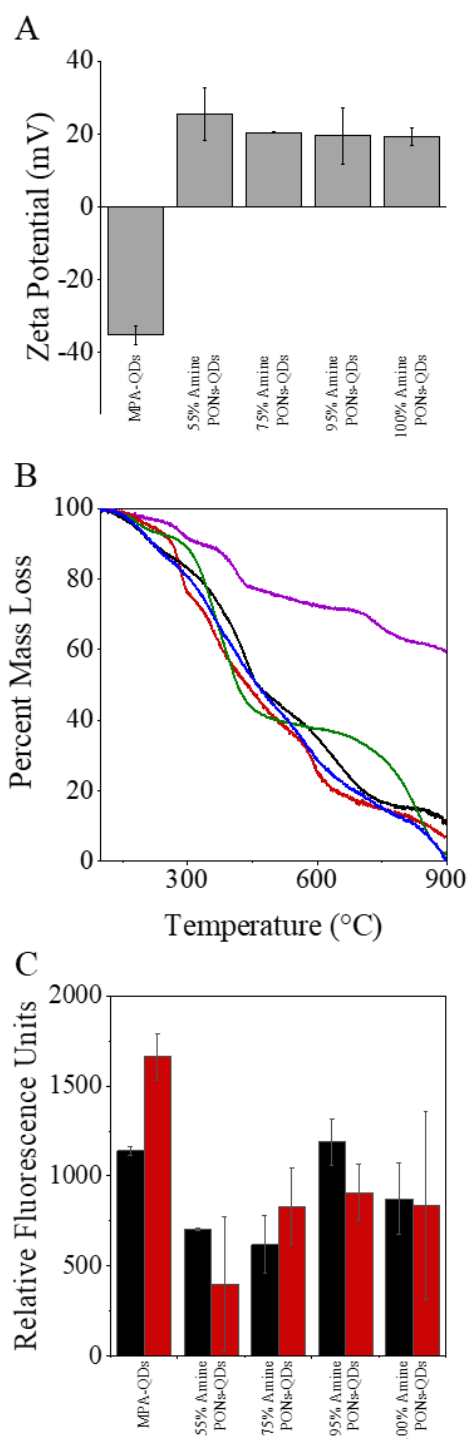


**Figure 5.5:** Zeta potential measurements show the MPA-QDs to be negatively charged and the PONs-QDs to be positively charged (A). TGA analysis show similar mass losses due to desorption of 55% (red), 75% (black), 95% (green), and 100% (blue) amine PONs from the surface of MPA-CdTe QDs (purple) with weak dependence on the amine/alkyl ratio in the conjugated PONs (B). Cell-free H<sub>2</sub>DCE ROS measurements with 6.25  $\mu\text{g}/\text{mL}$  PONs/12.5 nM QDs equivalents demonstrate higher ROS generation levels for free MPA-QDs with 2 hr of irradiation, but not for PONs-QDs (C). Further, the ROS levels of PONs-QDs depend on the PONs molecular structure. (N = 3 for panels A and B; N = 2 for panel C.)

QDs does not significantly depend on the PONs molecular structure, any changes in the activity of PONs-QDs coinciding with varying amine content is due to changes in PONs structure, and not due to differences in surface coverage.

With the similar number of varying amine content PONs per QD we expected to observe a greater difference in the  $\zeta$ -potential values between PONs-QDs of varying amine content, but interestingly we do not. The fact that we observe very similar  $\zeta$ -potential values between the varying amine content PONs-QDs indicates there is a likely a difference in orientation and packing of the PONs around the QDs, as was observed in the PONs-AuNPs study.<sup>177</sup> The hydrophilic amine side chains are oriented towards the surrounding solution, whereas the hydrophobic butyl side chains are packed against the QDs' surface. This would primarily leave only the amine side chains available for detection via  $\zeta$ -potential measurements, and could explain why there is minimal difference between the varying PONs-QDs  $\zeta$ -potential values. Further, this would result in the PONs-QDs with lower amine content PONs having tighter packing against the QD surface than the conjugates with higher amine PONs.

Figure 5.5C shows the effect of PONs conjugation on ROS generation from PONs-QDs in the absence (black) and presence (red) of irradiation during incubation. In agreement with previous studies,<sup>26</sup> irradiation of free MPA-QDs increases the ROS generation level by about 25% under our experimental conditions. However, conjugating the MPA-QDs to PONs prevented the same magnitude of ROS generation that was observed with free MPA-QDs. These observations might be attributed to the restricted access of water molecules, which are required for ROS generation, to the surface of QDs once they are coated with PONs. Further, without

irradiation the ROS generation from the PONs-QDs depends on the molecular structure of the PONs. This may be attributed to the access of water molecules to the PONs-QDs' surface being lower with increasing hydrophobicity (decreasing amine content) of the coating PONs. As previously discussed, the lower amine content PONs likely have a tighter packing around the QD surface than the higher amine content PONs, since the lower amine content PONs would have more hydrophobic side chains packed against the QD surface than the PONs-QDs with the higher amine content PONs. With irradiation, the ROS generation of the higher amine content (75–100%) PONs-QDs increases to similar levels observed for nonirradiated MPA-QDs.

#### 5.5.2 Antibacterial Activity of the free PONS and PONs-QDs Series

The anti-*S. aureus* activities of the PONs-QDs, with varying amine content PONs, were characterized parallel to the *S. aureus* MIC assays for the free PONs and the MPA-QDs. Figure 5.6A shows the normalized bacterial growth (in %) of *S. aureus* when incubated with free PONs of varying amine content and increasing concentration (6.25–100  $\mu\text{g}/\text{mL}$ ) without irradiation. The curves show a concentration dependent inhibition of *S. aureus* which—contrary to the literature<sup>115</sup>—only weakly depends on the PONs' molecular structure. These curves can be summarized by extrapolating the free PONs' concentration that inhibited at least 90% of bacterial growth ( $\text{MIC}_{90}$ ). The  $\text{MIC}_{90}$  values of the free PONs were 12.5  $\mu\text{g}/\text{mL}$  for 55% amine PONs and 50  $\mu\text{g}/\text{mL}$  for the remaining PONs. Figure 5.6B shows that the PONs-QDs are not at all effective against *S. aureus* growth. Considering the proven molecular weight-dependent activity of the PONs against gram-positive bacteria due

to their thick outer, cross-linked peptidoglycan layer preventing permeation of larger molecules to the inner plasma membrane<sup>127</sup>, the lack of PONs activity against *S. aureus* upon conjugation to a large nanoparticle makes sense. Because of the loss of inherent activity against *S. aureus* growth with QD conjugation, we did not pursue investigating the impact irradiation may have on this system.

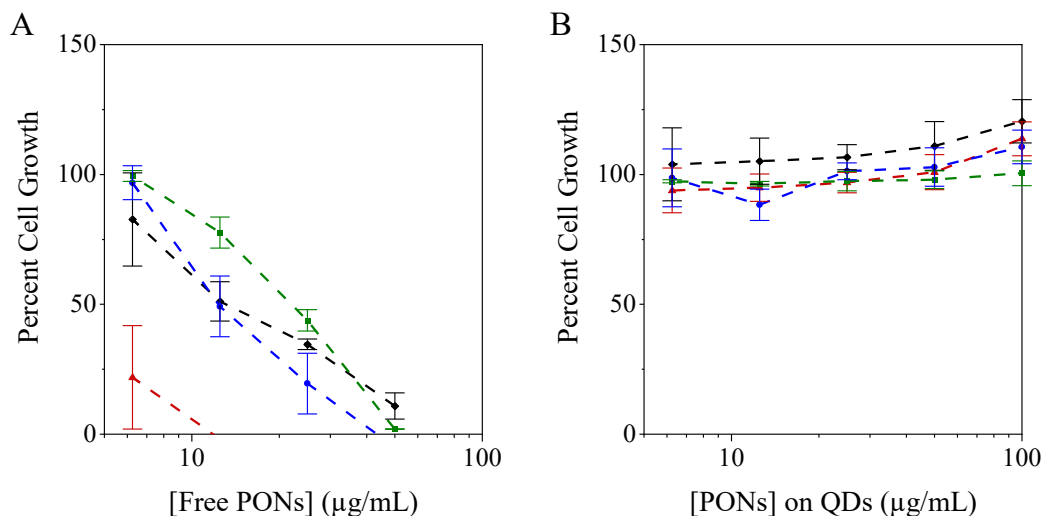


**Figure 5.6:** *S. aureus* growth after incubation with 6.25–100 µg/mL of free 55% (red), 75% (black), 95% (green), and 100% (blue) amine content PONs show that lower amine content PONs are more active than the higher amine content PONs (A). *S. aureus* growth when incubated with 6.25–100 µg/mL PONs equivalents (corresponding to 12.5–160 nM QD equivalents, as determined by TGA) of PONs-QDs without irradiation show that these cells are not sensitive to PONs-QD conjugates (B). (N ≥ 3 biological replicates.)

The anti-*E. coli* activities of the PONs-QDs, with varying amine content PONs, were characterized parallel to the *E. coli* MIC assays for the free PONs and the MPA-QDs (Figure 5.7). Figure 5.7A shows the normalized bacterial growth (in %) of *E. coli* when incubated with free PONs of varying amine content and increasing concentration (6.25–100 µg/mL) without irradiation. The MIC<sub>90</sub> values of the free PONs were 12.5 µg/mL for 55% amine PONs, 100 µg/mL for 75% amine PONs, and higher than 400 µg/mL for the 95% and 100% amine PONs. This data shows that the free PONs maintain the literature established trend of the lower amine content PONs

having greater activity against bacterial cell growth than the higher amine content PONs.<sup>115</sup> This trend has been attributed to the dependence of PONs' activity on the balance between the prevalence of cationic moieties which are necessary for electrostatic attraction of the PONs molecules to the anionic bacterial membrane, and the hydrophobic moieties which are needed to penetrate the membrane and lead to cell breakdown and death. We did not observe significant changes in the free PONs activity with irradiation (data not shown). Figures 5.7B and C show dose-response curves of *E. coli* growth when exposed to 6.25–100  $\mu\text{g/mL}$  PONs equivalents on the PONs-QDs. Without irradiation (Figure 5.5B), the PONs equivalent MIC<sub>90</sub> values for the conjugates against *E. coli* were 100, 200, 200, and 100  $\mu\text{g/mL}$  in order of increasing amine content PONs. With irradiation (Figure 5.5C), the PONs equivalent MIC<sub>90</sub>

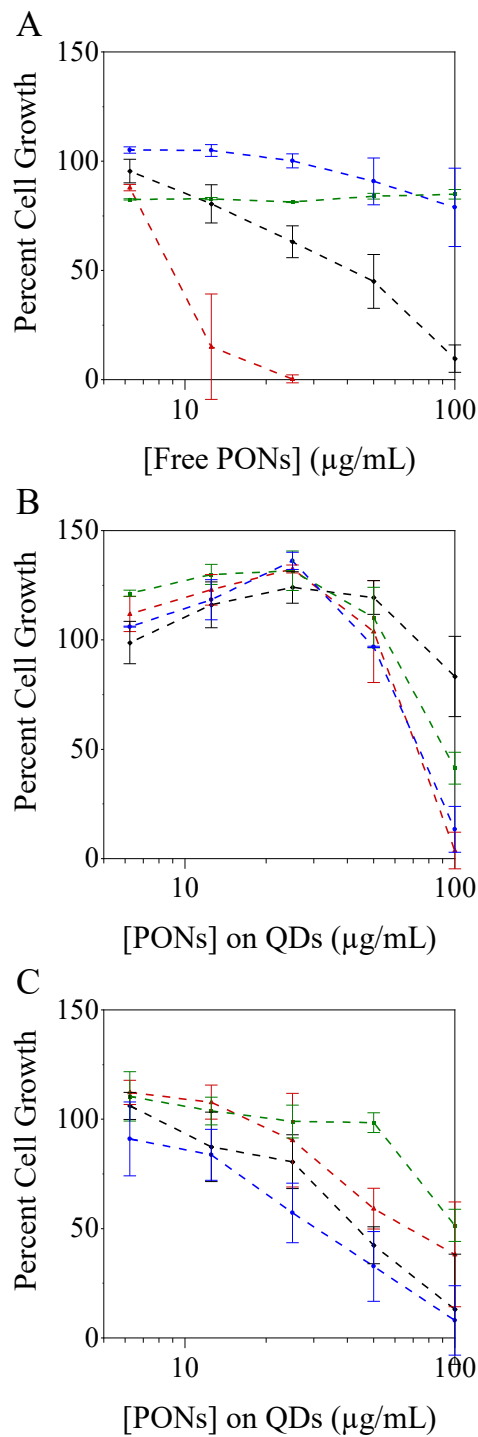


**Figure 5.7:** *E. coli* growth after incubation with 6.25–100  $\mu\text{g/mL}$  of free 55% (red), 75% (black), 95% (green), and 100% (blue) amine content PONs show that lower amine content PONs are more active than the higher amine content PONs (A). *E. coli* growth when incubated with 6.25–100  $\mu\text{g/mL}$  PONs equivalents (corresponding to 12.5–160 nM QD equivalents, as determined by TGA) of PONs-QDs without (B) and with 2 hr irradiation (C) show that higher amine PONs-QDs have increased antibacterial activity compared to their respective free PONs. Lower amine content PONs have decreased activity once conjugated to QDs. ( $N \geq 3$  biological replicates.)

values of 100, 100, 200, and 50  $\mu\text{g}/\text{mL}$  for PONs-QDs, in order of increasing amine content. These values only demonstrate an irradiation-induced increase in activity against bacterial growth for PONs-QDs with 75% and 100% amine/alkyl ratios. Regardless of irradiation, the lesser activity of the 55% and 75% amine content PONs-QD conjugates, compared to their activity as free PONs, coincides with their decreased ROS generation efficiency compared to the free MPA-QDs (Figure 5.5C). On the contrary, the higher amine content PONs-QDs do not have a significant difference in their ROS generation compared to the MPA-QDs; so their increase in anti-*E. coli* growth activity, compared to the respective free PONs, can be attributed to the preservation of the ROS generation-based activity of the QDs being combined with the anti-membrane activity of the PONs surface coatings. Regardless of the use of irradiation, conjugating the higher amine content PONs to the QDs increases their activity against *E. coli* growth compared to the same mass used as free PONs. This is likely due to there being more positively charged hydrophilic amine/ammonium groups directed toward the aqueous medium ready to interact with the negatively charged bacterial. While free PONs molecules have only a few charges under physiological conditions, the QD-bound PONs are able to fully behave like polyelectrolytes—which strongly enhances their interactions with the bacteria.

### 5.5.3 Hemolytic Activity of the free PONs and PONs-QDs Series

Figure 5.8 compares the concentration of the free PONs and the PONs equivalents of PONs-QDs that led to 50% hemolysis ( $\text{HC}_{50}$ ). The corresponding hemolytic curves with PONs concentrations between 0.1 to 8,000  $\mu\text{g}/\text{mL}$ , from which the  $\text{HC}_{50}$  values were extrapolated, can be found in Appendix Figure 5.5. PONs-QDs

(Figure 5.8, red) with PONs of high amine content show negligible hemolytic activity at all tested concentrations, while 55% amine PONs-QDs had an  $HC_{50}$  of 31.25  $\mu\text{g/mL}$  PONs equivalents and 75% amine PONs-QDs had an  $HC_{50}$  of 3,000  $\mu\text{g/mL}$  PONs equivalents. The hemolytic activity of the MPA- and PONs-QDs samples were not statistically affected by irradiation during incubation with RBCs (data not

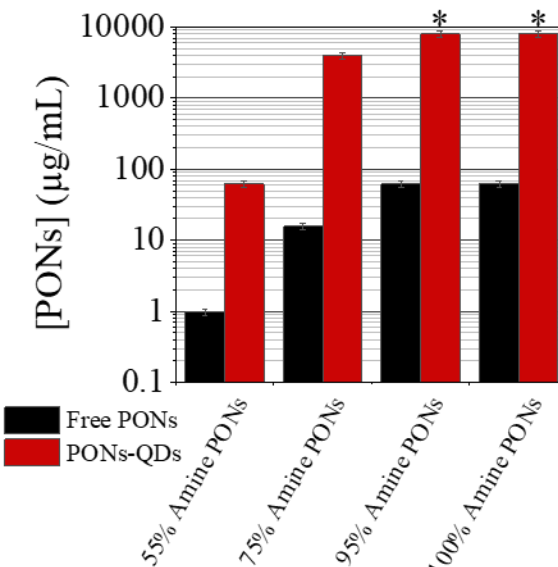


**Figure 5.8:** RBCs exposed to 0.1–8000  $\mu\text{g/mL}$  PONs equivalents of free PONs and PONs-QDs, the PONs-QDs (red) were found to have lower hemolytic activity than free PONs molecules (black).  $N = 3$  biological replicates. (\*Note:  $HC_{50}$  values for 95% and 100% amine PONs-CdTe QDs were not found within the tested concentration range, and are thus represented as bars to the highest tested concentration.)

shown). The hemolytic activity of all PONs-QDs is at least 2 orders of magnitude lower than that of the free PONs (Figure 5.8, black) which had measured  $HC_{50}$ 's of 1, 15.6, 31.25, and 41  $\mu\text{g/mL}$  in order of increasing amine content.

Once the PONs are attached to the QD surface, the restricted motility of the PONs and the QD surface-hugging orientation of the hydrophobic butyl side chains likely results in a lower effective concentration of hydrophobic groups interacting with the RBCs, and thus lesser hemolytic activity. Numerous studies have shown that synthetic mimics of antimicrobial peptides become toxic to mammalian cells (at the same cationic charge density) when they are too hydrophobic—for example, when the length of the alkyl side chain is increased by one repeat unit.<sup>115</sup> This is because increased molecular hydrophobicity results in an increased insertion of these surface-

active molecules into the hydrophobic part of the mammalian cell membrane. Thus, the decrease in toxicity of the QD-bound PONs can be interpreted as a reduced effective hydrophobicity compared to free PONs.

#### 5.5.4 Therapeutic Indices of free PONs vs PONs-QDs Series

Taking into consideration the change in anti-*E. coli* and hemolytic activities once the PONs were conjugated to the MPA-QDs, we calculated the therapeutic indices of the PONs-QDs and compared them to the therapeutic indices of free PONs. We defined the therapeutic index as a sample's  $HC_{50}$  divided by its  $MIC_{90}$ . We calculated the indices for free PONs against *E. coli* to be 0.08 for 55% amine PONs, 0.12 for 75% amine PONs, and inconclusive for 95% and 100% amine PONs due to the lack of antibacterial activity for these two free PONs at tested concentrations. The free PONs tested in this study had a smaller therapeutic window than found in the literature<sup>115</sup>, but the trend of higher amine content PONs having a larger therapeutic index than the smaller amine content PONs remained due to the higher amine content PONs having a lower hemolytic activity than the smaller amine content PONs. With irradiation, the therapeutic indices for PONs-QDs were 0.63, 40, > 40, and > 160, in order of increasing amine content. ('>' is used when the sample had no detected hemolytic activity.) The indices for the PONs-QDs are significantly larger in magnitude than the free PONs' therapeutic indices, especially for the 95% and 100% amine content PONs-QDs for which minimal hemolytic activity was detected even though there was antibacterial activity. The lower hemolytic activity of the PONs-QDs compared to free PONs against *E. coli* and the resulting therapeutic index

improvement demonstrates the potential for a higher PONs concentration to be used when in conjugate form (rather than free polymer form).

## 5.6 Investigating the Activity of LL-37-coated CdTe QDs

### 5.6.1 Characterization of LL-37-coated QDs

LL-37-coated QDs (peptide-QDs) were characterized via  $\zeta$ -potential and TGA measurements. After conjugation and thorough cleaning, the peptide-QDs had a positive potential. This positive  $\zeta$ -potential confirmed the conjugation of the cationic peptides to the MPA-QDs' surface. After correcting for the  $29 \pm 2\%$  mass loss due to the loss of MPA from the QDs, TGA analysis determined the peptide accounted for  $57 \pm 2\%$  of the total peptide-QDs' mass (Figure 5.9).

### 5.6.2 Biological Activity of LL-37-coated QDs

Only the anti-*E. coli* and hemolytic activity of the peptide and peptide-QDs, with and without irradiation, was compared to the activity of PONs-QDs since the PONs-QDs showed no anti-*S. aureus* activity. Figure 5.10A and B show the normalized bacterial growth (in %) of *E. coli* when incubated with free peptide and peptide-QDs of increasing concentration (1.25-20  $\mu\text{g/mL}$ ), with (B) and without (A) irradiation. The curves show concentration dependent inhibition of bacterial viability for both samples. Without irradiation

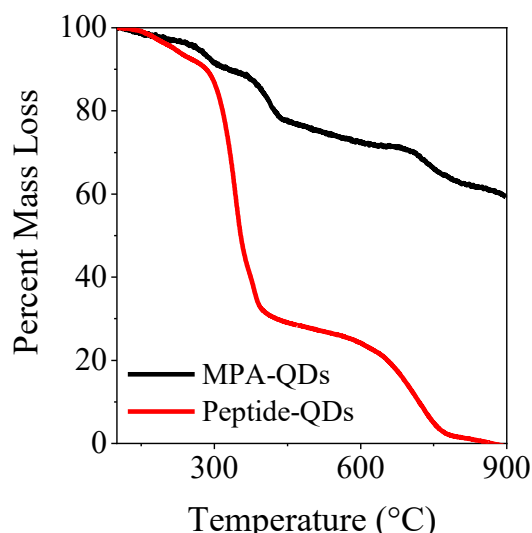


**Figure 5.9:** TGA analysis illustrate that  $57 \pm 2\%$  of the peptide-QDs' mass was LL-37 peptides. (N=3)

(Figure 5.10A), the MIC<sub>90</sub> values were 20  $\mu\text{g}/\text{mL}$  for both samples. With irradiation (Figure 5.10B), the MIC<sub>90</sub> value remained the same for the free peptide, but decreased to 10  $\mu\text{g}/\text{mL}$  for the peptide-QDs, which demonstrates a light activated increase in antibacterial activity at a similar magnitude as that observed with the 75% and 100% amine PONs-QDs. Figure 5.10C shows the normalized hemolytic activity (in %) when RBCs were incubated with free peptide and peptide-QDs of increasing concentration (1.25-20  $\mu\text{g}/\text{mL}$ ) with irradiation. (Without irradiation, the activity is statistically similar.) The hemolytic activity of the free and conjugated peptides are similar, as expected since this peptide does not have a hydrophobic region that can be effectively buried to prevent its insertion into the hydrophobic region of mammalian membranes, like the PONs do.

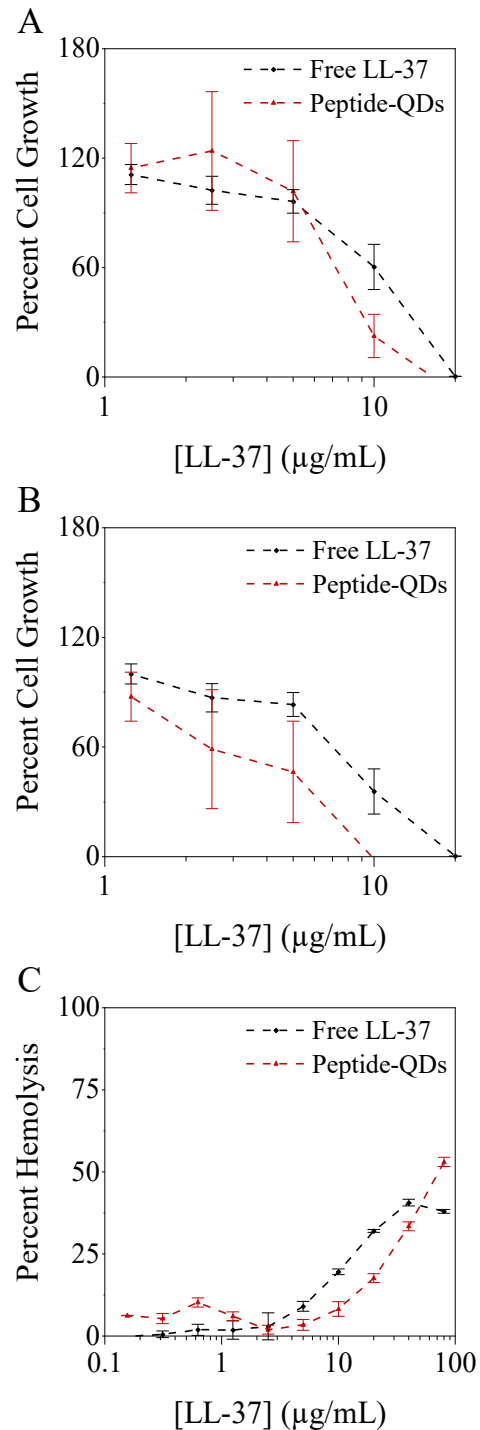


**Figure 5.10:** Without irradiation, *E. coli* cells exposed to 1.25–20  $\mu\text{g}/\text{mL}$  LL-37 equivalents of the free LL-37 peptide (black) and peptide-QDs (red) show a concentration dependent decrease in growth (A). With 2 hr irradiation at the beginning of incubation, the peptide-QDs have irradiation enhanced activity, while the free peptides activity is maintained (B). The free LL-37 peptide and peptide-QDs had similar concentration dependent hemolytic activity at tested concentrations, with and without light activation (C). (N = 3 biological replicates.)

The therapeutic index for the irradiated peptide-QDs, 8, is smaller than the PONs-QDs of the highest amine contents. We interpret this to mean that the conjugates with the tunable synthetic antimicrobial peptide mimics, PONs, may be the better alternative antibacterial treatment compared to the conjugates with the naturally occurring antimicrobial peptide.

## 5.7 Conclusions

A series of PONs with varying amine/alkyl ratios and the LL-37 peptide were conjugated to the surface of MPA-CdTe QDs in order to study the PONs-QDs and peptide-QDs conjugates' antibacterial and hemolytic activity. Prior to conjugation, the free MPA-QDs—at a concentration range of 1–160 nM—only exhibited significant antibacterial activity when they were irradiated, and had no significant hemolytic activity with or without irradiation. Prior to conjugation, the free PONs' antibacterial and hemolytic activity decreased as the amine content increased from 55% to 100%, in agreement with previous studies.<sup>115</sup> PONs conjugation to the surface of the CdTe QDs resulted in a general loss of the trend of amine content-dependent antibacterial activity and loss in activity against *S. aureus* viability. However, we did observe 1) irradiation-enhanced anti-*E. coli* activity from the PONs-QD conjugates which was comparable to that of the free PONs of similar PONs mass, 2) a decrease in hemolytic activity especially for the higher amine content PONs-containing conjugates, and 3) an increase in the therapeutic index. Similarly, conjugating the LL-37 peptide to the CdTe QDs resulted in increased irradiation-enhanced anti-*E. coli* activity and increased therapeutic index. The larger therapeutic indices may enable the use of both PONs-QDs and peptide-QDs at greater and more effective

concentrations against drug-resistant gram-negative bacteria, such as *E. coli*, with reduced concerns about hemolytic and toxic activity against mammalian cells. Further, our studies demonstrate that the light activated PONs-QDs treatments may be the better of the two options.

## Chapter 6: Conclusions

### 6.1 Summary

This dissertation is a composition of fundamental studies which elucidate molecular interactions between quantum dots (QDs) and cells in the context of antibacterial QD technologies. These studies specifically investigate how systematic changes to the material, structural, and surface ligand compositions of antibacterial QDs affect their interactions with pathogenic and essential cells relevant to human and environmental health.

The studies of Chapter 3 developed a foundational understanding of how QDs of varying compositions interact with the outer interface of the cell—the membrane—using simple liposome models. The liposome models varied in lipid composition in order to mimic some of the differences between bacterial and mammalian cell membranes of various species. Additionally, different dyes were incorporated into the liposomes in order that optical signals could be detected and interpreted to tell if the QDs interacted with the membranes and, if so, how. Experiments with calcein-labeled liposomes confirmed the literature-sourced hypothesis that cadmium-containing QDs tend to have more toxic interactions with bacterial membranes than cadmium-free QDs. Experiments with nitrobenzoxadiazole-labeled liposomes demonstrated that nonirradiated QDs can destabilize the membrane through membrane depolarization, but that this was not always a significant cause of destructive cytotoxicity since the cadmium-free QDs depolarized the membrane without causing significant membrane lysis. Experiments with unlabeled liposomes and ICP-MS measurements revealed

how the structure of QDs impacted their stability in various mediums and their anti-membrane activity. The cadmium-free QDs were more stable in the HEPES buffer than the cadmium-containing QDs. Thus, there was minimal toxic heavy metal dissolution from the cadmium-free QDs compared to the cadmium-containing QDs. FRET experiments with rhodamine-labeled liposomes revealed the dependence of QD-membrane association on both the QDs' and liposomes'  $\zeta$  potential, and demonstrated electrostatic interactions as a major driver of QD-liposome association. Furthermore, all the outcomes of this chapter imply that QDs' miscibility and stability—in every medium—needs to be considered before inferring the potential interactions between them and surrounding organisms.

Chapter 4 studies further reiterated the need to consider QDs' chemical behavior, but in the context of an environmentally-relevant bacterial model's interactions with QDs of varying material and structural composition. The same cadmium-containing QDs that showed greater anti-membrane activity in Chapter 3 had greater antibacterial activity against *Shewanella oneidensis* MR-1, a prevalent gram-negative bacterium with a unique metal-reducing metabolism. Even though *S. oneidensis* has resistance to some heavy metals—because of its metabolism—and was not affected by exposures to ZnSe and ZnSe/ZnS QDs in these studies, its viability was inhibited after exposures to cadmium-containing QDs with concentration and shell size dependency. ICP-MS and ion control incubation studies revealed that *S. oneidensis*'s responses to QD incubations could be explained by the same phenomenon's that distinguished the cadmium-containing and cadmium-free QDs in Chapter 3.

Chapter 5 studies built upon the QD-membrane affinity trends observed between the QDs and membrane models in the literature and Chapter 3, but brought these trends into the context of human health models' interactions with unique antibacterial polymer- and antimicrobial peptide-coated QD conjugates. Cadmium-containing core QDs were chosen for these conjugates as our prior studies revealed that these were optimal for maximizing the intended bacterial cell death. Thus, the QD conjugates were built from the base of CdTe core QDs, which have demonstrated light-enhanceable antibacterial activity through ROS interactions. The second piece of prior information that was incorporated into the design of these conjugates was the role of electrostatic attractions in QD-membrane association. We wanted to design cytotoxic QD conjugates that would have an inherently greater attraction for bacterial membranes than mammalian membranes in order to limit off target toxicity. Thus, a PONs polymer series and the LL-37 peptide were conjugated to the surface of the QDs as these entities have demonstrated antibacterial selectivity and activity. We found that all QD conjugates had greater activity against *Escherichia coli* growth and larger therapeutic indexes than any of the entities alone, with and without irradiation. Further, we found that the higher amine density PONs-QD conjugates had the greatest activity and therapeutic indexes of all the tested conjugates. Digressing, in general, the increase in therapeutic indexes observed with the conjugates is likely due to 1) the increased cationic charge density of the antibacterial coatings once they were conjugated to the QD surface—effectively increasing the attraction between the conjugates and the bacterial cells—and 2) the minimized effective hydrophobic

character of the coating entities after their conjugation, which further minimized their potential to interact with mammalian cells.

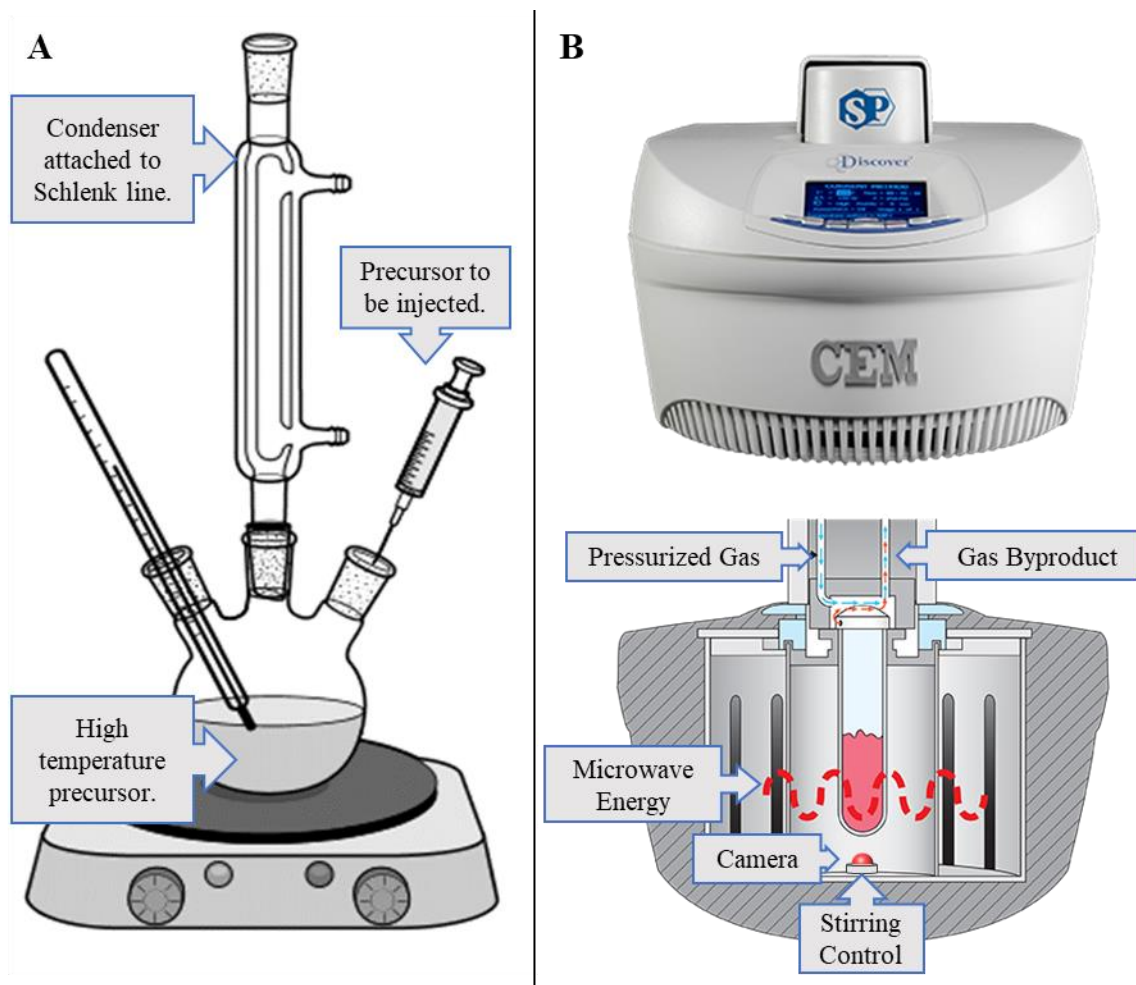
## **6.2 Future Directions**

While this work has made deconvoluted conclusions about the interactions between QDs and bacteria that have enabled the design of unique antibacterial QD conjugates, there are still some fundamental questions and some missing project complexities that can be addressed in future work. First, an obvious shortcoming that can be identified is the simplicity of the liposome models. Membrane vesicle models with cholesterol and other lipids, with lipid rafts, with peptidoglycan layers, and of larger sizes would be closer to genuine bacterial membranes. There are increasingly more vesicle formulations and available vesicle components that can be used in future experiments to achieve more realistic model formulations. Moving forward with these more complex vesicle formulations may improve upon the conclusions that can be drawn from observing QD interactions with them. Another concept that would be interesting to investigate is whether the QDs are instantaneously bursting the liposomes used in Chapter 3, or simply inducing a slow leakage. Single molecule fluorescence microscopy may be a useful technique to employ for investigating this curiosity. A third area of valuable future work would be to expand these same QD-bacteria interaction studies to panels of human and environmental health bacteria. It would be valuable to determine if the found trends of activity remain; such as, will the PONs-QDs be effective against other gram-negative bacteria—even if MDR—and remain ineffective against other gram-positive bacteria.

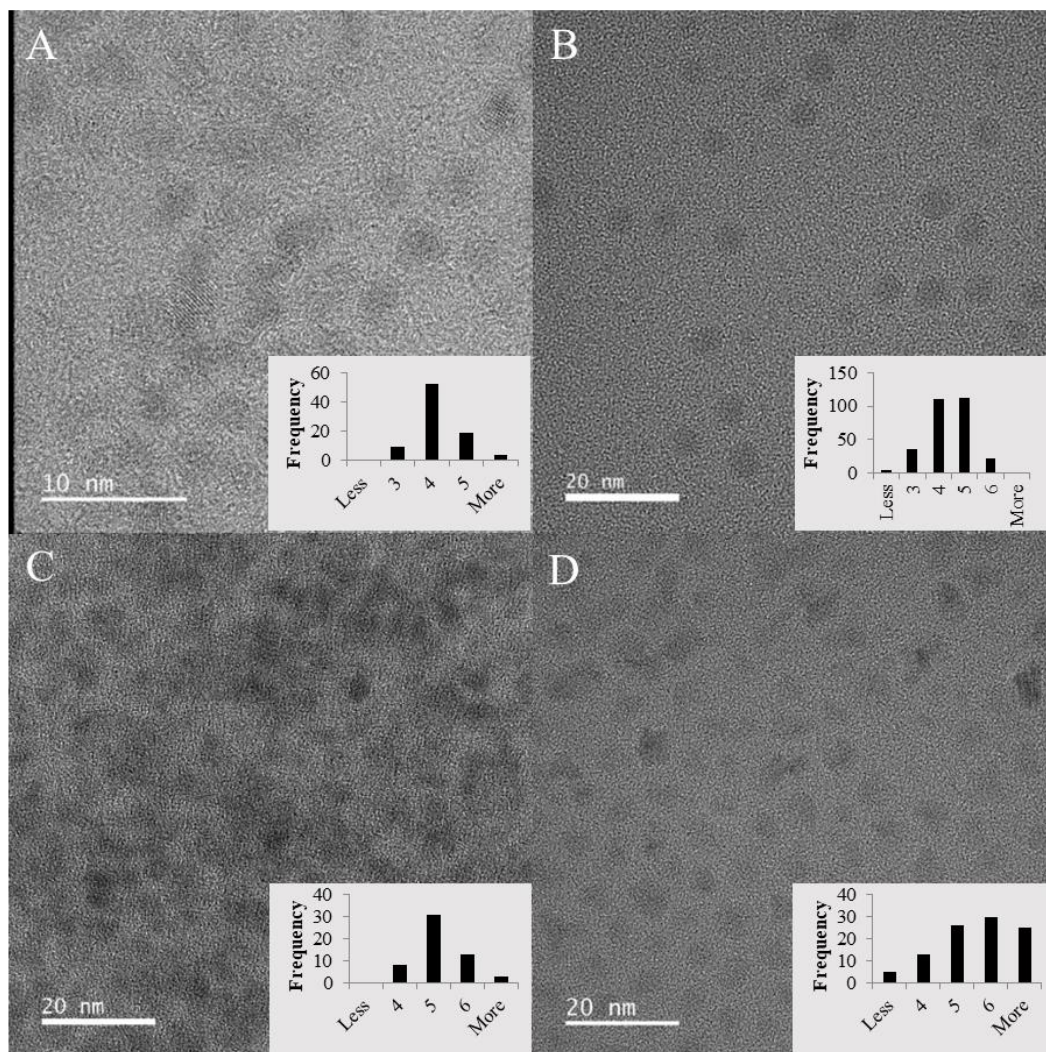
While the aforementioned experimental approaches would certainly provide valuable insight into the robustness of this dissertation's findings, theoretical and computational chemistry approaches may be more suitable for considering the full extent of variables which may affect the interactions between antibacterial QD constructs, pathogenic cells, and essential cells in reasonable timeframes. Even hands-on experiments designed to consider all the possible cell compositions with just one QD construct requires the efforts of several scientists, over several years, and immense financial support. The improving chemical modeling capabilities at the molecular and cellular levels may allow simulative approaches to inform the design of experiments to include investigations of only the 'most important/necessary' variables, and remove some of the time and resource burdens that considering all the variables would require.

Clearly, there is more work to be done to fully elucidate the complexity of interactions between QDs and cells. Nevertheless, this dissertation does conclude fundamental information on well characterized QD-bacteria interactions which can be harmonized with other works and used to support the design of the next generation of effective antibacterial entities.

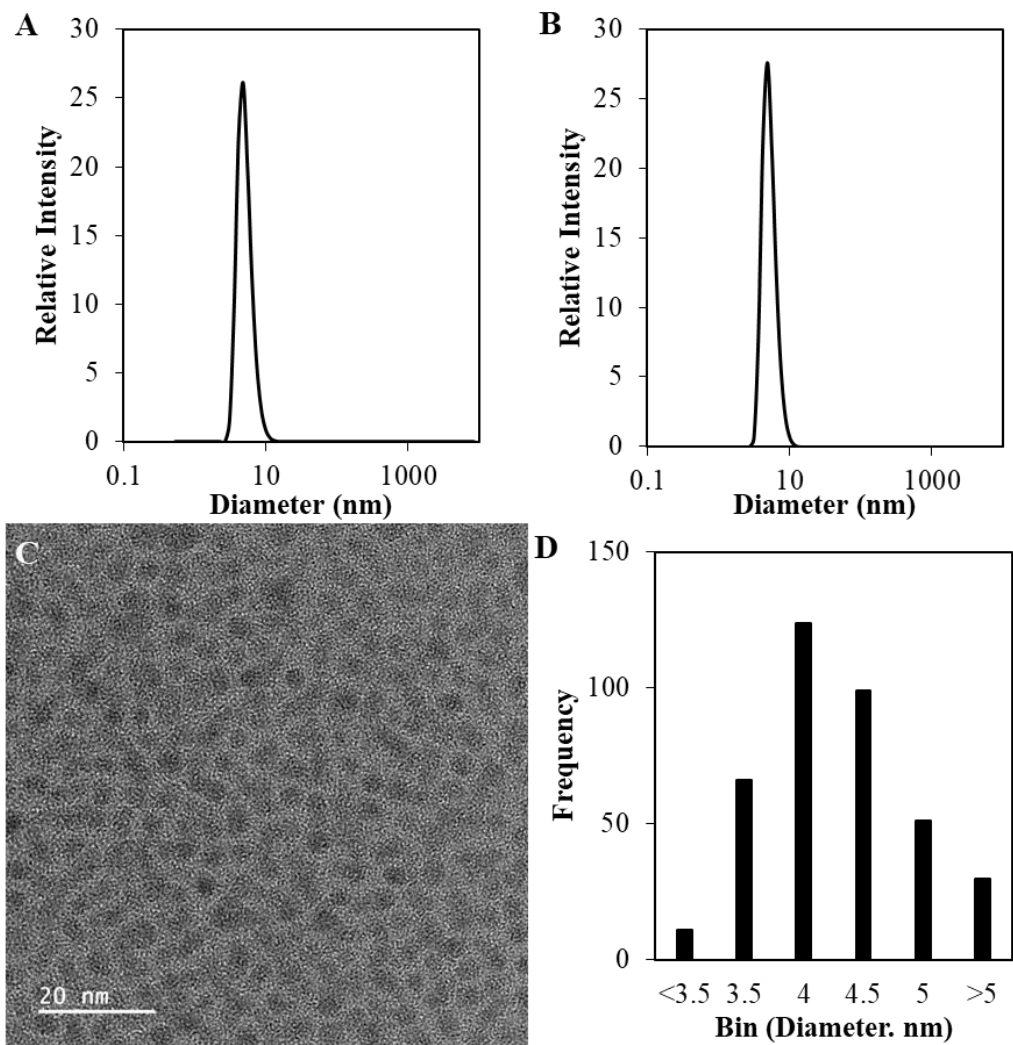
## Appendices



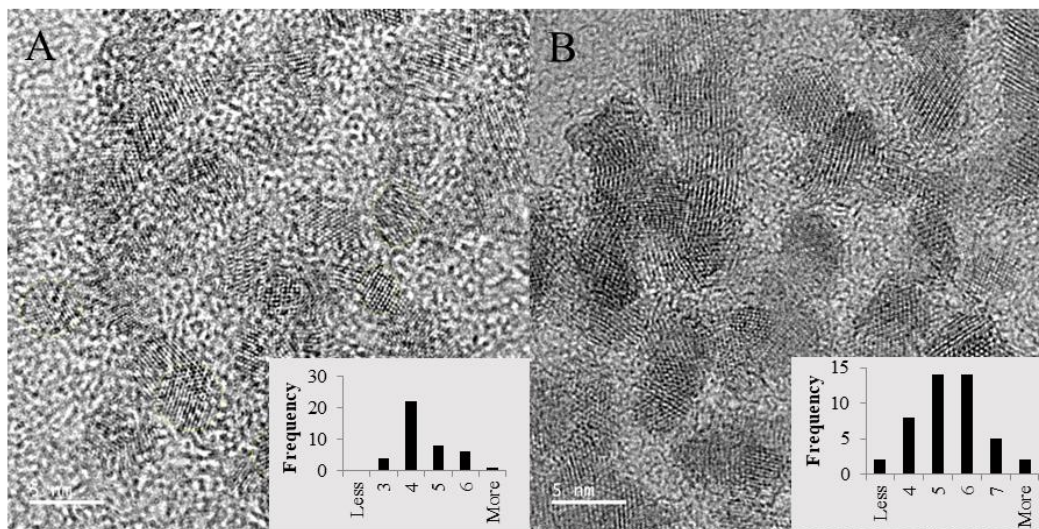
**Appendix Figure 2.1:** Glassware set-up for the hot injection synthesis technique (A). Diagram of microwave for dielectric QD synthesis (B), modified from the CEM website.



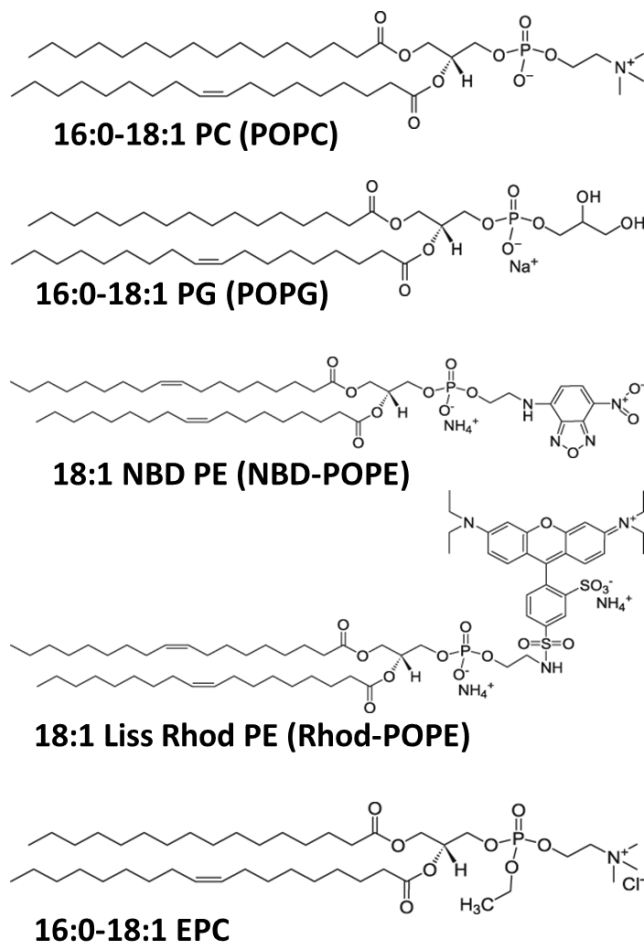
**Appendix Figure 2.2:** HRTEM images, with size distribution inserts showing  $3.9 \pm 0.5$  nm CdSe cores (A),  $4.2 \pm 0.8$  nm CdSe/ZnS (1 ML) (B),  $5.0 \pm 0.9$  nm CdSe/ZnS (3 ML) (C), and  $5.9 \pm 0.8$  nm CdSe/ZnS (6 ML) (D) QDs. Figures were previously published in Williams et al. Applied Nano Materials. 2018, 1 (9), 4788-4800.<sup>148</sup>



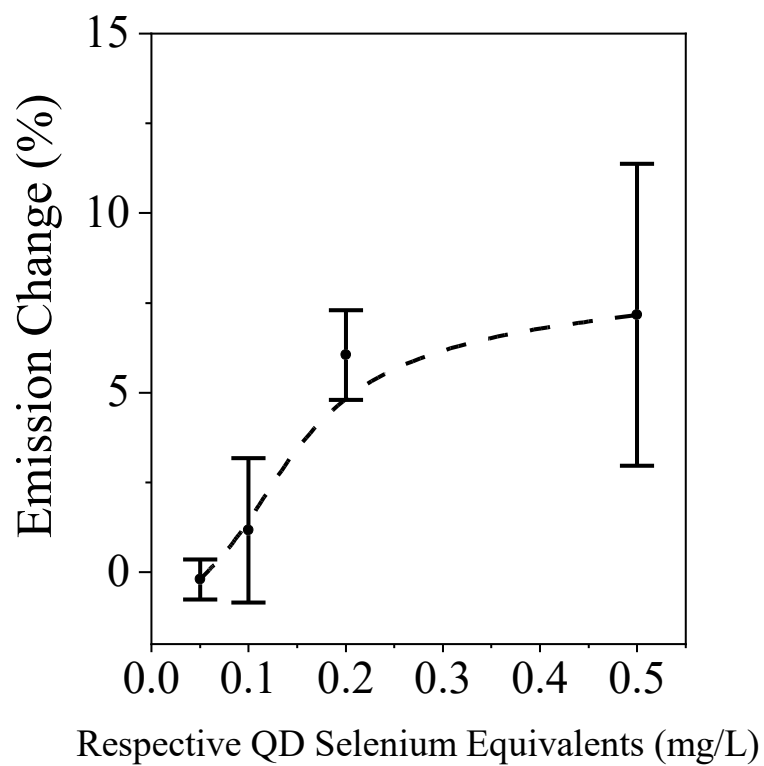
**Appendix Figure 2.3:** Additional HRTEM images of the CdTe QDs. DLS-measured number size distribution of MPA-QDs in Tris buffer (pH 7) determined their hydrodynamic diameter to be  $5.2 \pm 1.3$  nm (A); N=3. DLS-measured number size distribution of MPA-QDs in water (pH 7) determined their hydrodynamic diameter to be  $5.2 \pm 1.2$  nm (B); N=3. A representative HRTEM image of MPA-QDs (C) and the binned ImageJ analysis of several HRTEM images (D) represent their diameter to be  $4.0 \pm 0.6$  nm; N=381. Figures were previously published in Williams et al. Applied Bio Materials. 2020, 3(2), 1097-1104.<sup>149</sup>



**Appendix Figure 2.4:** HRTEM images of  $3.5 \pm 0.4$  nm ZnSe core QDs (A) and  $5.0 \pm 1.2$  nm ZnSe/ZnS QDs (B). Inserts show size distribution of all analyzed QDs.



**Appendix Figure 3.1:** Molecular structures of the lipids used in Chapter 3.



**Appendix Figure 3.2:** Liposome lysis of calcein-containing liposomes when exposed to the DHLA-PEG ligands controls. The concentrations of the ligands used at the respective QD equivalents are as calculated on the next page.

### Calculations of QD Ligand Coverage

Step 1: Calculating the number of ligands per QD. Literature, which characterized the number of surface binding sites for nanoparticles via XPS, has estimated moderately covered nanoparticles to have 4.5 surface binding sites/nm<sup>2</sup>.<sup>226</sup> This ratio was used to calculate the number of binding sites and ligands on these QDs. Note: The DHLA-PEG ligand is bidentate, which means it will occupy two binding sites on a QD.

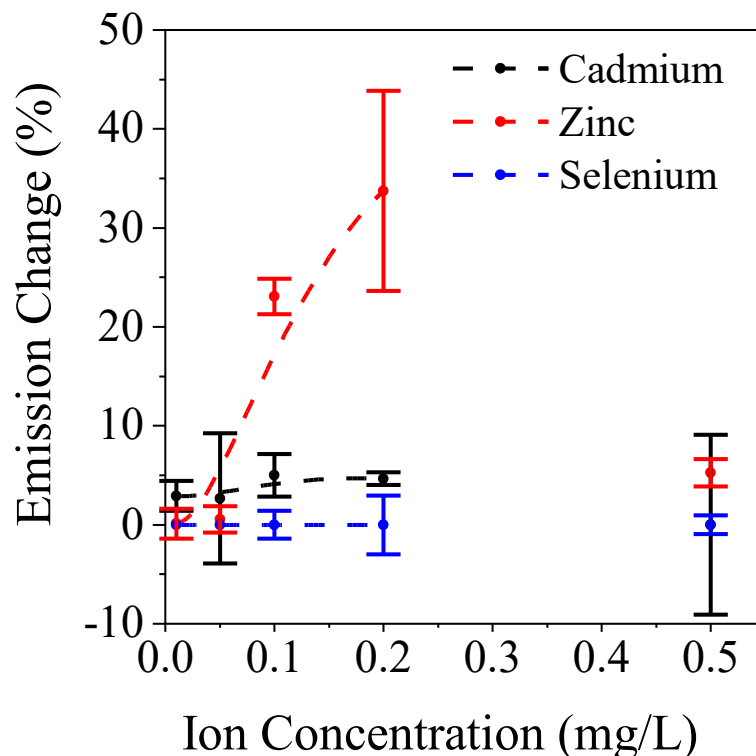
For a ~3.5 nm diameter QD at 173 sites/particle: 87 bidentate ligands/QD  
For a ~4.0 nm diameter QD at 226 sites/particle: 113 bidentate ligands/QD  
For a ~4.3 nm diameter QD at 260 sites/particle: 131 bidentate ligands/QD  
For a ~5.0 nm diameter QD at 353 sites/particle: 177 bidentate ligands/QD  
For a ~6.0 nm diameter QD at 509 sites/particle: 254 bidentate ligands/QD

Step 2: Calculating the number of ligands per exposure. ICP-MS was used to convert between mg/L and moles of QDs so that we could determine the number of ligands per QD exposure. The ligand control assays illustrated in Appendix Figure 3.1 involved DHLA-PEG ligand concentrations up to the amount of ligand that theoretically exists on the surface of the largest concentration of the largest QDs tested, 0.5 mg/L CdSe/ZnS(6 ML) QDs. The calculations are as follows:

A 1 mL sample at 0.5 mg/L selenium equivalents of CdSe/ZnS(6 ML) QDs  
= 0.7 pmol QDs (as determined by ICP-MS)  
=  $1.07 \times 10^{14}$  ligands (converted using Step 1)  
= 165 ng ligands (converted using MW of ligand = 927 g/mol)  
= 0.165 mg/L DHLA-PEG ligands

Step 3: Extrapolate the calculations to all tested CdSe/ZnS(6 ML) QD concentrations.

For 0.01 mg/L selenium equivalents = 0.0033 mg/L DHLA-PEG750-OCH<sub>3</sub>  
For 0.05 mg/L selenium equivalents = 0.0066 mg/L DHLA-PEG750-OCH<sub>3</sub>  
For 0.1 mg/L selenium equivalents = 0.033 mg/L DHLA-PEG750-OCH<sub>3</sub>  
For 0.2 mg/L selenium equivalents = 0.066 mg/L DHLA-PEG750-OCH<sub>3</sub>  
For 0.5 mg/L selenium equivalents = 0.165 mg/L DHLA-PEG750-OCH<sub>3</sub>



**Appendix Figure 3.3:** Liposome lysis of calcein-containing liposomes when exposed to the  $\text{Cd}^{2+}$ ,  $\text{Zn}^{2+}$ , and  $\text{Se}^{4+}$  controls. ( $N \geq 3$ )

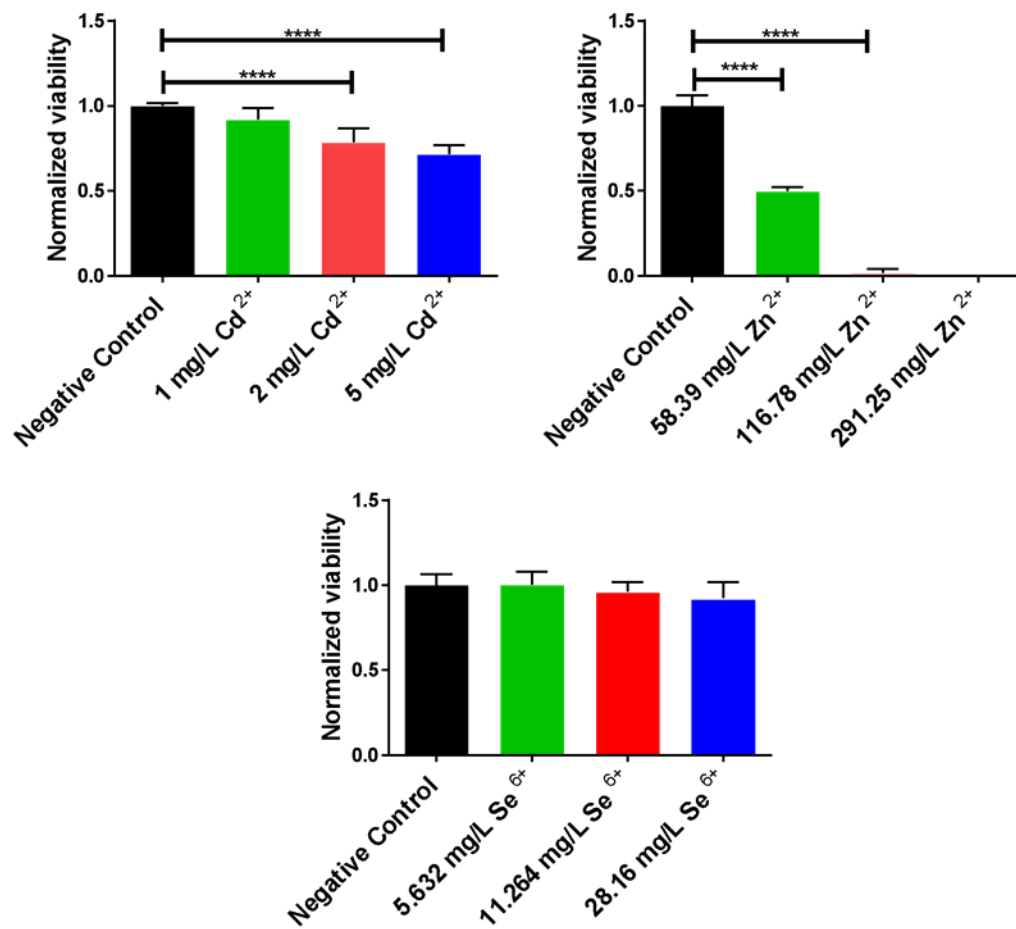
Cadmium and zinc ion controls caused minimal liposome lysis. Zinc ions induce significant lysis at concentrations relevant to the full dissolution of CdSe/ZnS, ZnSe core, and ZnSe/ZnS QDs. This zinc ion behavior further supports the notion that ZnS dissolution from the CdSe core may contribute to its toxicity, and that the stability of (ie: lack of ion dissolution from) the ZnSe and ZnSe/ZnS prevents zinc ion toxicity. (High concentrations of all ions quenched calcein fluorescence. Hence, 0.5 mg/L of all ions are plotted but not included in the linear projection.)

**Appendix Table 3.1:** Size and zeta potential characterization of POPC-based liposomes with varying amount of rhod-lipids.

<b>Liposome Formulation (mole : mole)</b>	<b>Diameter (nm)</b>	<b>St. Dev.</b>	<b>Zeta Potential (mV)</b>	<b>St. Dev.</b>
POPC	73.04	20.29	-2.54	11.8
0.01 rhod-POPE:1 POPC	57.67	19.98	-6.58	12.0
0.02 rhod-POPE:1 POPC	74.80	19.70	-7.81	9.44
0.03 rhod-POPE:1 POPC	70.17	19.79	-9.43	10.2
0.04 rhod-POPE:1 POPC	64.91	18.31	-23.2	15.0
0.05 rhod-POPE:1 POPC	74.74	20.31	-15.3	9.88
0.06 rhod-POPE:1 POPC	73.73	32.26	-24.7	7.46
0.07 rhod-POPE:1 POPC	69.59	18.97	-20.2	11.7
0.08 rhod-POPE:1 POPC	70.05	18.02	-20.5	12.0
0.10 rhod-POPE:1 POPC	65.68	18.33	-26.7	14.6
0.20 rhod-POPE:1 POPC	83.00	32.46	-34.6	17.5
0.30 rhod-POPE:1 POPC	66.78	17.24	-38.3	14.2

**Appendix Table 3.2:** Size and zeta potential characterization of the 5 membered 3 mol% rhod-liposome charge series. The liposomes' lipids that are not rhod-POPE or the table indicated charged lipid are the zwitterionic POPC lipids.

<b>Liposome Formulation</b>	<b>Diameter (nm)</b>	<b>St. Dev.</b>	<b>Zeta Potential (mV)</b>	<b>St. Dev.</b>
20% POPG	70.91	18.97	-32.70	19.80
10% POPG	77.34	19.37	-26.90	17.30
Just POPC	81.30	21.46	-12.20	11.10
10% EPC	67.70	18.75	17.90	10.00
20% EPC	62.03	18.83	39.80	12.20



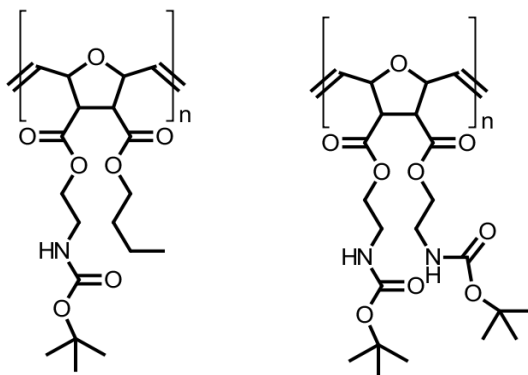
**Appendix Figure 4.1:** *S. oneidensis* viability after exposure to ion controls.

## Butyl Poly(oxanorbornene) Polymers (PONs) Synthesis and Characterization

This section on PONs synthesis is a modified reproduction of Supporting Information for Williams *et al.* Poly(oxanorbornene)-Coated CdTe Quantum Dots as Antibacterial Agents. *ACS Applied Bio Materials*. 2020, 3 (2), 1097–1104.<sup>149</sup>

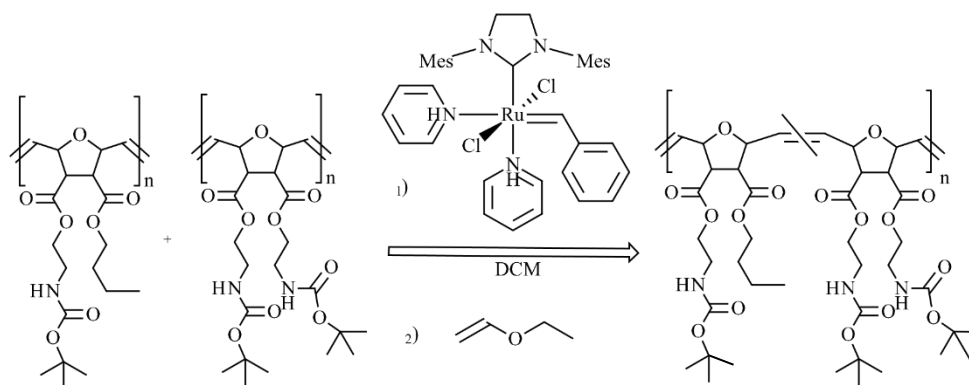
**Materials.** All chemicals and solvents were used as received from Sigma Aldrich, Fluka, or Acros Organic.

**Instrumentation.** Gel permeation chromatography (GPC) was performed on a Polymers Standards Service styrene-divinylbenzene (SDV) copolymer network column using chloroform as the solvent system at a 1.0 mL/min flow rate and 30 °C. GPC was calibrated with poly (methyl methacrylate) standards. Nuclear Magnetic Resonance (NMR) spectra were recorded on a Bruker 250 MHz spectrometer. Deuterated methanol and chloroform were used as solvents, and tetramethylsilane was used as the internal reference.

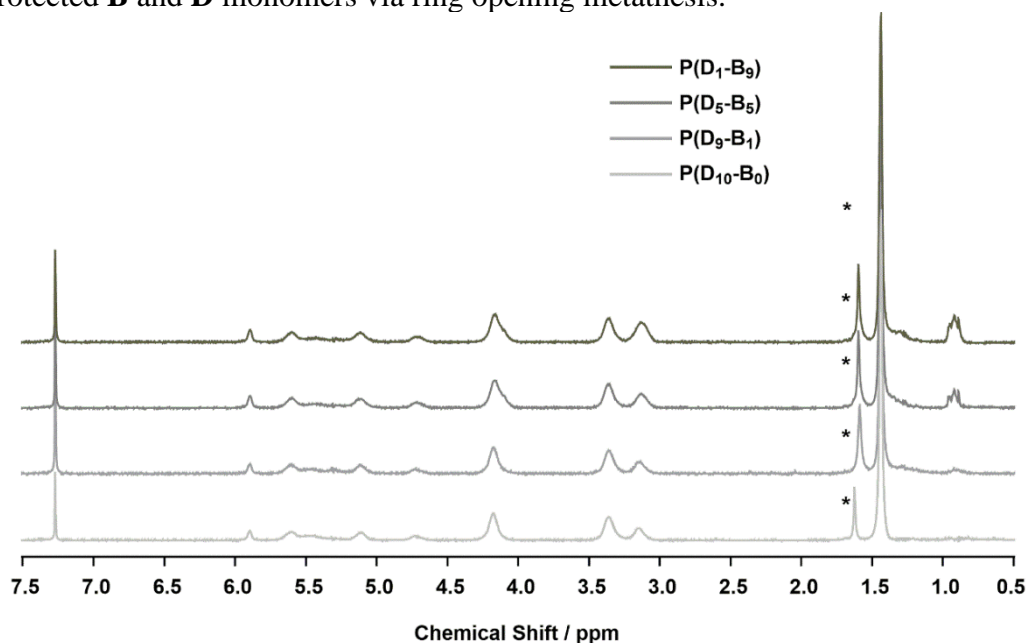


**Appendix Figure 5.1:** Structure of the two BOC-protected oxanorbornene monomers **B** (left) and **D** (right).

**Polymer Synthesis and Characterization.** The polymers in this study are the same as reported in the publication by Zheng *et al.* on the membrane disruption activity of PONs-covered gold nanoparticles.<sup>177</sup> Figure S1 shows the two monomers, one with a butyl and an amine side chain (**B**) and the other with two diamine side chains (**D**), synthesized and polymerized according to previously reported protocols.<sup>220, 222</sup> The monomers were synthesized with tert-butyloxycarbonyl(BOC) protection on the amine functional groups. For polymerization (Scheme S1), dichloromethane mixtures of the monomers and Grubbs' third generation catalyst, synthesized as described by Love *et al.*<sup>227</sup>, were allowed to react for 30 minutes under inert N<sub>2</sub> gas. The ratio of **B** to **D** monomers was varied in order to obtain polymers with varying amine content (Table S1). The reaction was stopped with the addition of excess ethyl vinyl ether. BOC-protected polymers were precipitated with cold hexane and dried under vacuum. To remove the BOC protecting groups, polymers were dissolved in a 1:1 mixture of dry chloroform and 4M HCl in dioxane. The precipitated, deprotected polymers were dissolved in dry methanol and finally re-precipitated in cold diethyl ether under vacuum. NMR and GPC were used to confirm the polymer structure and mass according to previous literature.



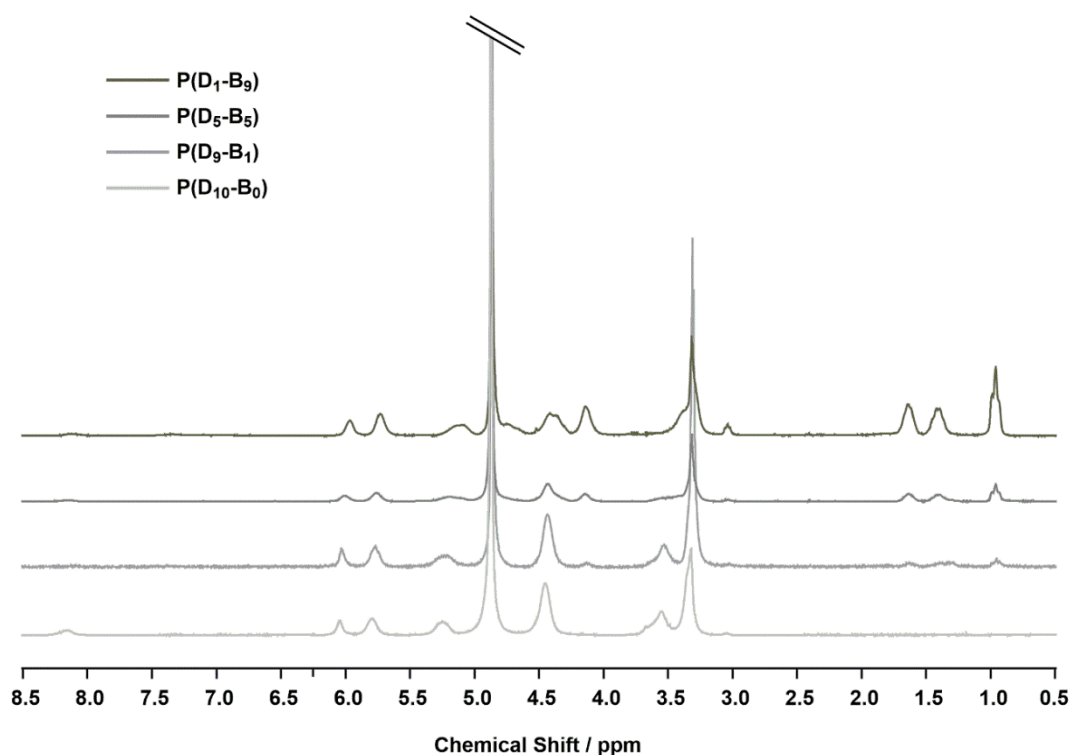
**Appendix Scheme 5.1:** Grubbs' third generation catalysts initiated polymerization of BOC-protected **B** and **D** monomers via ring opening metathesis.



**Appendix Figure 5.2:** NMR data of BOC-protected PONs in deuterated chloroform. <sup>1</sup>H-NMR (250 MHz, CDCl<sub>3</sub>) δ = 5.85 - 5.93 (br m, C=CH, trans), 5.55 - 5.66 (br m, C=CH, cis), 5.32 - 5.46 (br s, NH), 5.07 - 5.19 (br m, C=CH-CH, cis), 4.65 - 4.76 (br m, C=CH-CH, trans), 4.04 - 4.26 (m, O-CH), 3.27 - 3.45 (br m, N-CH<sub>2</sub>), 3.05 - 3.21 (br m, CH), 1.55 - 1.63 (m, CH<sub>2</sub>), 1.23 - 1.49 (m, B-CH<sub>2</sub> & 3 × boc-CH<sub>3</sub>), 0.93 (t, B-CH<sub>3</sub>). Note: \* Indicates water peak.

**Appendix Table 5.1:** The properties of the BOC-protected PONs with 10 repeat units and varying amine content. \*Determined via GPC analysis.

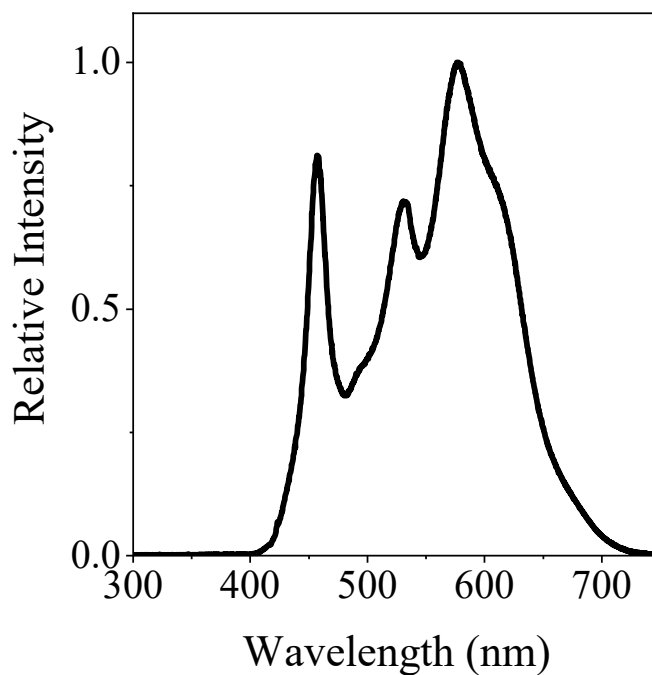
PONs Sample	nd: nb	Average	
		MW <sub>Monomer</sub> (g/mol)	MW <sub>Polymer</sub> * (g/mol)
55% Amine	1:9	391.89	3900
75% Amine	5:5	426.71	4000
95% Amine	9:1	461.53	4700
100% Amine	10:0	470.23	4700



**Appendix Figure 5.3:** NMR data for deprotected PONs.  $^1\text{H-NMR}$  (250 MHz, MeOD- $d_4$ , peaks corresponding to  $\text{C}=\text{CH-CH}$  (trans) and  $\text{CH}$  overlapped with the solvent signals)  $\delta = 8.05 - 8.20$  (br. m,  $\text{NH}_3^+$ ),  $5.89 - 6.05$  (br m,  $\text{C}=\text{CH}$ , trans),  $5.63 - 5.84$  (br m,  $\text{C}=\text{CH}$ , cis),  $5.01 - 5.29$  (br m,  $\text{C}=\text{CH-CH}$ , cis),  $4.01 - 4.53$  (m,  $\text{O-CH}$ ),  $3.30 - 3.70$  (m,  $\text{N-CH}_2$ ),  $1.55 - 1.73$  (m,  $\text{CH}_2$ ),  $1.30 - 1.50$  (m,  $\text{B-CH}_2$ ),  $0.97$  (t,  $\text{B-CH}_3$ ).

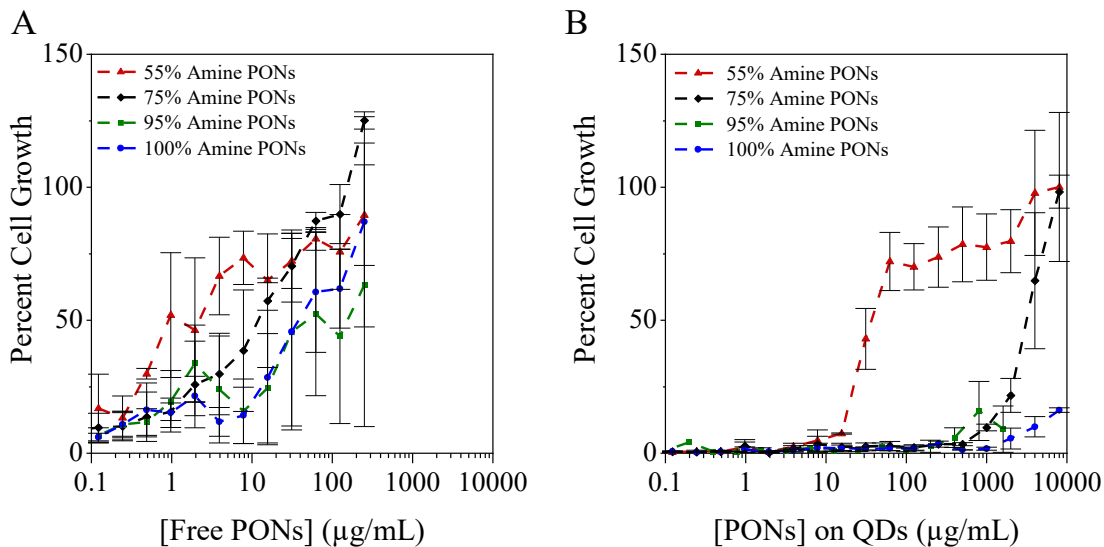
**Appendix Table 5.2:** The properties of the deprotected PONs, which were synthesized to have 10 repeat units of varying amine content.

PONs Sample	nd: nb	Average $\text{MW}_{\text{Monomer}}$ (g/mol)	Average $\text{MW}_{\text{Polymer}}$ (g/mol)
55% Amine	1:9	281.74	2800
75% Amine	5:5	276.52	2800
95% Amine	9:1	271.30	2700
100% Amine	10:0	270.00	2700



**Appendix Figure 5.4:** Emission spectrum of the Environmental Lights Ultra Thin LED Light Panel (Neutral White), which was characterized using an EO Edmund CCD Spectrometer.

Additionally, the panel was measured to have an average output of 3 mW using the Newport Corporation 843-R Optical Power Meter, with the 919P-030-18 thermopile sensor placed on the opposite side of an empty 96 well plate from the LED panel.



**Appendix Figure 5.5:** Hemolytic activity curves of the free PONs (A) and the PONs-QDs (B). All PONs-QDs have lower hemolytic activity than free PONs molecules. Incubations were done with and without LED panel irradiation during incubation. Irradiated incubation did not change the hemolytic activity of the MPA-QDs or PONs-QDs samples (data not shown).

## Bibliography

1. Wang, G., Structures of Human Host Defense Cathelicidin LL-37 and Its Smallest Antimicrobial Peptide KR-12 in Lipid Micelles. *Journal of Biological Chemistry* **2008**, 283 (47), 32637-32643.
2. Ekimov, A. I.; Onushchenko, A. A., Quantum size effect in three-dimensional microscopic semiconductor crystals. *Jetp Lett* **1981**, 34 (6), 345-349.
3. Kamat, P.; Scholes, G., Quantum Dots Continue to Shine Brightly. *Journal of Physical Chemistry Letters* **2016**, 7 (3), 584-585.
4. Reiss, P.; Protiere, M.; Li, L., Core/Shell Semiconductor Nanocrystals. *Small* **2009**, 5 (2), 154-168.
5. Protesescu, L.; Yakunin, S.; Bodnarchuk, M.; Krieg, F.; Caputo, R.; Hendon, C.; Yang, R.; Walsh, A.; Kovalenko, M., Nanocrystals of Cesium Lead Halide Perovskites (CsPbX<sub>3</sub>, X = Cl, Br, and I): Novel Optoelectronic Materials Showing Bright Emission with Wide Color Gamut. *Nano Letters* **2015**, 15 (6), 3692-3696.
6. Bawendi Research Group, Research: <http://nanocluster.mit.edu/research.php>.
7. Yu, W.; Peng, X., Formation of high-quality CdS and other II-VI semiconductor nanocrystals in noncoordinating solvents: Tunable reactivity of monomers. *Angewandte Chemie-International Edition* **2002**, 41 (13), 2368-2371.
8. Liu, D.; Snee, P., Water-Soluble Semiconductor Nanocrystals Cap Exchanged with Metalated Ligands. *Acs Nano* **2011**, 5 (1), 546-550.
9. Bimberg, D., Quantum dots for lasers, amplifiers and computing. *Journal of Physics D-Applied Physics* **2005**, 38 (13), 2055-2058.
10. Venere, E., "Quantum Dots" Could Form Basis Of New Computers. Perdue News: West Lafayette, Indiana, 2001.
11. Ji, W.; Jing, P.; Xu, W.; Yuan, X.; Wang, Y.; Zhao, J.; Jen, A., High color purity ZnSe/ZnS core/shell quantum dot based blue light emitting diodes with an inverted device structure. *Applied Physics Letters* **2013**, 103 (5).
12. Zhao, K.; Pan, Z.; Zhong, X., Charge Recombination Control for High Efficiency Quantum Dot Sensitized Solar Cells. *Journal of Physical Chemistry Letters* **2016**, 7 (3), 406-417.
13. Bang, J.; Park, J.; Lee, J.; Won, N.; Nam, J.; Lim, J.; Chang, B.; Lee, H.; Chon, B.; Shin, J.; Park, J.; Choi, J.; Cho, K.; Park, S.; Joo, T.; Kim, S., ZnTe/ZnSe (Core/Shell) Type-II Quantum Dots: Their Optical and Photovoltaic Properties. *Chemistry of Materials* **2010**, 22 (1), 233-240.
14. Xu, G.; Zeng, S.; Zhang, B.; Swihart, M.; Yong, K.; Prasad, P., New Generation Cadmium-Free Quantum Dots for Biophotonics and Nanomedicine. *Chemical Reviews* **2016**, 116 (19), 12234-12327.
15. Liang, X.; Grice, J.; Zhu, Y.; Liu, D.; Sanchez, W.; Li, Z.; Crawford, D.; Le Couteur, D.; Cogger, V.; Liu, X.; Xu, Z.; Roberts, M., Intravital Multiphoton Imaging of the Selective Uptake of Water-Dispersible Quantum Dots into Sinusoidal Liver Cells. *Small* **2015**, 11 (14), 1711-1720.
16. Aldeek, F.; Mustin, C.; Balan, L.; Roques-Carmes, T.; Fontaine-Aupart, M.-P.; Schneider, R., Surface-engineered quantum dots for the labeling of

- hydrophobic microdomains in bacterial biofilms. *Biomaterials* **2011**, *32* (23), 5459-5470.
17. Yong, K.; Ding, H.; Roy, I.; Law, W.; Bergey, E.; Maitra, A.; Prasad, P., Imaging Pancreatic Cancer Using Bioconjugated InP Quantum Dots. *Acs Nano* **2009**, *3* (3), 502-510.
  18. Yong, K.-T.; Wang, Y.; Roy, I.; Rui, H.; Swihart, M. T.; Law, W.-C.; Kwak, S. K.; Ye, L.; Liu, J.; Mahajan, S. D., Preparation of quantum dot/drug nanoparticle formulations for traceable targeted delivery and therapy. *Theranostics* **2012**, *2* (7), 681.
  19. Seil, J. T.; Webster, T. J., Antimicrobial applications of nanotechnology: methods and literature. *International journal of nanomedicine* **2012**, *7*, 2767-2781.
  20. Singh, A.; Dubey, A. K., Various biomaterials and techniques for improving antibacterial response. *ACS Applied Bio Materials* **2018**, *1* (1), 3-20.
  21. Lakshmeesha, R.; Moin, A.; Gowda, D. V.; Santhosh, T. R.; Abhilasha, T. P.; Sebastian, G.; Ali, R.; Osmani, M., Quantum Dots: A New-fangled Loom in Drug Delivery and Therapeutics. *World Journal of Pharmaceutical Sciences* **2016**, *4* (4), 125-134.
  22. Jamieson, T.; Bakhshi, R.; Petrova, D.; Pocock, R.; Imani, M.; Seifalian, A. M., Biological applications of quantum dots. *Biomaterials* **2007**, *28* (31), 4717-4732.
  23. Frasco, M. F.; Chaniotakis, N., Semiconductor quantum dots in chemical sensors and biosensors. *Sensors* **2009**, *9* (9), 7266-7286.
  24. Mattoussi, H.; Palui, G.; Na, H. B., Luminescent quantum dots as platforms for probing in vitro and in vivo biological processes. *Advanced drug delivery reviews* **2012**, *64* (2), 138-166.
  25. Chen, H.; Zhang, M.; Li, B.; Chen, D.; Dong, X.; Wang, Y.; Gu, Y., Versatile antimicrobial peptide-based ZnO quantum dots for in vivo bacteria diagnosis and treatment with high specificity. *Biomaterials* **2015**, *53*, 532-544.
  26. Courtney, C.; Goodman, S.; McDaniel, J.; Madinger, N.; Chatterjee, A.; Nagpal, P., Photoexcited quantum dots for killing multidrug-resistant bacteria. *Nature Materials* **2016**, *15* (5), 529-534.
  27. Derfus, A.; Chan, W.; Bhatia, S., Probing the cytotoxicity of semiconductor quantum dots. *Nano Letters* **2004**, *4* (1), 11-18.
  28. Dumas, E.; Gao, C.; Suffern, D.; Bradforth, S. E.; Dimitrijevic, N. M.; Nadeau, J. L., Interfacial Charge Transfer between CdTe Quantum Dots and Gram Negative Vs Gram Positive Bacteria. *Environmental Science & Technology* **2010**, *44* (4), 1464-1470.
  29. Lai, L.; Li, S.; Feng, J.; Mei, P.; Ren, Z.; Chang, Y.; Liu, Y., Effects of Surface Charges on the Bactericide Activity of CdTe/ZnS Quantum Dots: A Cell Membrane Disruption Perspective. *Langmuir* **2017**, *33* (9), 2378-2386.
  30. Leptihn, S.; Guo, L.; Frecer, V.; Ho, B.; Ding, J.; Wohland, T., Single molecule resolution of the antimicrobial action of quantum dot-labeled sushi peptide on live bacteria. *Virulence* **2010**, *1* (1), 42-44.
  31. Luo, Z.; Wu, Q.; Zhang, M.; Li, P.; Ding, Y., Cooperative antimicrobial activity of CdTe quantum dots with rocephin and fluorescence monitoring for

- Escherichia coli. *Journal of Colloid and Interface Science* **2011**, 362 (1), 100-106.
32. Mahendra, S.; Zhu, H.; Colvin, V.; Alvarez, P., Quantum Dot Weathering Results in Microbial Toxicity. *Environmental Science & Technology* **2008**, 42 (24), 9424-9430.
  33. Pramanik, S.; Hill, S. K. E.; Zhi, B.; Hudson-Smith, N. V.; Wu, J. J.; White, J. N.; McIntire, E. A.; Kondeti, V. S. S. K.; Lee, A. L.; Bruggeman, P. J., Comparative toxicity assessment of novel Si quantum dots and their traditional Cd-based counterparts using bacteria models *Shewanella oneidensis* and *Bacillus subtilis*. *Environmental Science: Nano* **2018**, 5 (8), 1890-1901.
  34. Kuo, W.-S.; Shao, Y.-T.; Huang, K.-S.; Chou, T.-M.; Yang, C.-H., Antimicrobial amino-functionalized nitrogen-doped graphene quantum dots for eliminating multidrug-resistant species in dual-modality photodynamic therapy and bioimaging under two-photon excitation. *ACS applied materials & interfaces* **2018**, 10 (17), 14438-14446.
  35. Applerot, G.; Lipovsky, A.; Dror, R.; Perkas, N.; Nitzan, Y.; Lubart, R.; Gedanken, A., Enhanced antibacterial activity of nanocrystalline ZnO due to increased ROS-mediated cell injury. *Advanced Functional Materials* **2009**, 19 (6), 842-852.
  36. Nguyen, K. C.; Seligy, V. L.; Tayabali, A. F., Cadmium telluride quantum dot nanoparticle cytotoxicity and effects on model immune responses to *Pseudomonas aeruginosa*. *Nanotoxicology* **2013**, 7 (2), 202-211.
  37. Narband, N.; Mubarak, M.; Ready, D.; Parkin, I.; Nair, S.; Green, M.; Beeby, A.; Wilson, M., Quantum dots as enhancers of the efficacy of bacterial lethal photosensitization. *Nanotechnology* **2008**, 19 (44), 445102.
  38. Chen, B.; Liu, Q.; Zhang, Y.; Xu, L.; Fang, X., Transmembrane delivery of the cell-penetrating peptide conjugated semiconductor quantum dots. *Langmuir* **2008**, 24 (20), 11866-11871.
  39. Erogbogbo, F.; Yong, K.; Roy, I.; Xu, G.; Prasad, P.; Swihart, M., Biocompatible luminescent silicon quantum dots for imaging of cancer cells. *ACS Nano* **2008**, 2 (5), 873-878.
  40. Fan, H.-y.; Yu, X.-h.; Wang, K.; Yin, Y.-j.; Tang, Y.-j.; Tang, Y.-l.; Liang, X.-h., Graphene quantum dots (GQDs)-based nanomaterials for improving photodynamic therapy in cancer treatment. *European journal of medicinal chemistry* **2019**, 111620.
  41. Manshian, B.; Soenen, S.; Al-Ali, A.; Brown, A.; Hondow, N.; Wills, J.; Jenkins, G.; Doak, S., Cell Type-Dependent Changes in CdSe/ZnS Quantum Dot Uptake and Toxic Endpoints. *Toxicological Sciences* **2015**, 144 (2), 246-258.
  42. Carlini, L. Photosensitization of InP/ZnS quantum dots for photodynamic therapy. McGill University McGill University Montreal, Quebec, Canada, 2011.
  43. Drobintseva, A. O.; Matyushkin, L. B.; Aleksandrova, O. A.; Drobintsev, P. D.; Kvetnoy, I. M.; Mazing, D. S.; Moshnikov, V. A.; Polyakova, V. O.; Musikhin, S. F., Colloidal CdSe and ZnSe/Mn quantum dots: Their cytotoxicity and effects on cell morphology. *St. Petersburg Polytechnical University Journal: Physics and Mathematics* **2015**, 1 (3), 272-277.

44. Galdiero, E.; Siciliano, A.; Maselli, V.; Gesuele, R.; Guida, M.; Fulgione, D.; Galdiero, S.; Lombardi, L.; Falanga, A., An integrated study on antimicrobial activity and ecotoxicity of quantum dots and quantum dots coated with the antimicrobial peptide indolicidin. *International Journal of Nanomedicine* **2016**, *11*, 4199-4211.
45. Green, M.; Howman, E., Semiconductor quantum dots and free radical induced DNA nicking. *Chemical Communications* **2005**, (1), 121-123.
46. Lee, B.-T.; Kim, H.-A.; Williamson, J. L.; Ranville, J. F., Bioaccumulation and in-vivo dissolution of CdSe/ZnS with three different surface coatings by *Daphnia magna*. *Chemosphere* **2016**, *143*, 115-122.
47. Lu, Z.; Li, C. M.; Bao, H.; Qiao, Y.; Toh, Y.; Yang, X., Mechanism of Antimicrobial Activity of CdTe Quantum Dots. *Langmuir* **2008**, *24* (10), 5445-5452.
48. Mei, J.; Yang, L.; Lai, L.; Xu, Z.; Wang, C.; Zhao, J.; Jin, J.; Jiang, F.; Liu, Y., The interactions between CdSe quantum dots and yeast *Saccharomyces cerevisiae*: Adhesion of quantum dots to the cell surface and the protection effect of ZnS shell. *Chemosphere* **2014**, *112*, 92-99.
49. Mir, I. A.; Radhakrishnan, V. S.; Rawat, K.; Prasad, T.; Bohidar, H. B., Bandgap tunable AgInS based quantum dots for high contrast cell imaging with enhanced photodynamic and antifungal applications. *Scientific reports* **2018**, *8* (1), 1-12.
50. Park, S.; Chibli, H.; Wong, J.; Nadeau, J., Antimicrobial activity and cellular toxicity of nanoparticle-polymyxin B conjugates. *Nanotechnology* **2011**, *22* (18), 185101.
51. Priester, J.; Stoimenov, P.; Mielke, R.; Webb, S.; Ehrhardt, C.; Zhang, J.; Stucky, G.; Holden, P., Effects of Soluble Cadmium Salts Versus CdSe Quantum Dots on the Growth of Planktonic *Pseudomonas aeruginosa*. *Environmental Science & Technology* **2009**, *43* (7), 2589-2594.
52. Rajendiran, K.; Zhao, Z.; Pei, D.-S.; Fu, A., Antimicrobial Activity and Mechanism of Functionalized Quantum Dots. *Polymers* **2019**, *11* (10), 1670.
53. Romoser, A.; Ritter, D.; Majitha, R.; Meissner, K. E.; McShane, M.; Sayes, C. M., Mitigation of quantum dot cytotoxicity by microencapsulation. *PloS one* **2011**, *6* (7), e22079-e22079.
54. Soenen, S. J.; Demeester, J.; De Smedt, S. C.; Braeckmans, K., The cytotoxic effects of polymer-coated quantum dots and restrictions for live cell applications. *Biomaterials* **2012**, *33* (19), 4882-4888.
55. Sun, M.; Yu, Q.; Liu, M.; Chen, X.; Liu, Z.; Zhou, H.; Yuan, Y.; Liu, L.; Li, M.; Zhang, C., A novel toxicity mechanism of CdSe nanoparticles to *Saccharomyces cerevisiae*: Enhancement of vacuolar membrane permeabilization (VMP). *Chemico-Biological Interactions* **2014**, *220*, 208-213.
56. Xiao, Y.; Ho, K.; Burgess, R.; Cashman, M., Aggregation, Sedimentation, Dissolution, and Bioavailability of Quantum Dots in Estuarine Systems. *Environmental Science & Technology* **2017**, *51* (3), 1357-1363.
57. Zhang, T.; Stilwell, J.; Gerion, D.; Ding, L.; Elboudwarej, O.; Cooke, P.; Gray, J.; Alivisatos, A.; Chen, F., Cellular effect of high doses of silica-coated

- quantum dot profiled with high throughput gene expression analysis and high content cellomics measurements. *Nano Letters* **2006**, *6* (4), 800-808.
58. Zhao, Y.; Liu, Q.; Shakoor, S.; Gong, J.; Wang, D., Transgenerational safety of nitrogen-doped graphene quantum dots and the underlying cellular mechanism in *Caenorhabditis elegans*. *Toxicology Research* **2015**, *4* (2), 270-280.
  59. Zhou, J.; Liu, Y.; Tang, J.; Tang, W., Surface ligands engineering of semiconductor quantum dots for chemosensory and biological applications. *Materials Today* **2017**, *20* (7), 360-376.
  60. Bottrill, M.; Green, M., Some aspects of quantum dot toxicity. *Chemical Communications* **2011**, *47* (25), 7039-7050.
  61. Maurer-Jones, M.; Gunsolus, I.; Murphy, C.; Haynes, C., Toxicity of Engineered Nanoparticles in the Environment. *Analytical Chemistry* **2013**, *85* (6), 3036-3049.
  62. Hardman, R., A toxicologic review of quantum dots: Toxicity depends on physicochemical and environmental factors. *Environmental Health Perspectives* **2006**, *114* (2), 165-172.
  63. Mo, D.; Hu, L.; Zeng, G.; Chen, G.; Wan, J.; Yu, Z.; Huang, Z.; He, K.; Zhang, C.; Cheng, M., Cadmium-containing quantum dots: properties, applications, and toxicity. *Applied Microbiology and Biotechnology* **2017**, *101* (7), 2713-2733.
  64. Chandrangsu, P.; Rensing, C.; Helmann, J. D., Metal homeostasis and resistance in bacteria. *Nature reviews. Microbiology* **2017**, *15* (6), 338-350.
  65. Zoroddu, M. A.; Aaseth, J.; Crisponi, G.; Medici, S.; Peana, M.; Nurchi, V. M., The essential metals for humans: a brief overview. *Journal of Inorganic Biochemistry* **2019**, *195*, 120-129.
  66. Lemire, J. A.; Harrison, J. J.; Turner, R. J., Antimicrobial activity of metals: mechanisms, molecular targets and applications. *Nature Reviews Microbiology* **2013**, *11*, 371.
  67. McDevitt, C. A.; Ogunniyi, A. D.; Valkov, E.; Lawrence, M. C.; Kobe, B.; McEwan, A. G.; Paton, J. C., A Molecular Mechanism for Bacterial Susceptibility to Zinc. *PLOS Pathogens* **2011**, *7* (11), e1002357.
  68. Groisman, E. A.; Hollands, K.; Kriner, M. A.; Lee, E.-J.; Park, S.-Y.; Pontes, M. H., Bacterial Mg<sup>2+</sup> homeostasis, transport, and virulence. *Annual review of genetics* **2013**, *47*, 625-646.
  69. Porcheron, G.; Garénaux, A.; Proulx, J.; Sabri, M.; Dozois, C. M., Iron, copper, zinc, and manganese transport and regulation in pathogenic Enterobacteria: correlations between strains, site of infection and the relative importance of the different metal transport systems for virulence. *Frontiers in cellular and infection microbiology* **2013**, *3*, 90-90.
  70. Staicu, L. C.; Oremland, R. S.; Tobe, R.; Mihara, H., Bacteria Versus Selenium: A View from the Inside Out. In *Selenium in plants: Molecular, Physiological, Ecological and Evolutionary Aspects*, Pilon-Smits, E. A. H.; Winkel, L. H. E.; Lin, Z.-Q., Eds. Springer International Publishing: Cham, 2017; pp 79-108.
  71. Macy, J. M.; Michel, T. A.; Kirsch, D. G., Selenate reduction by a *Pseudomonas* species: a new mode of anaerobic respiration. *FEMS Microbiology Letters* **1989**, *61* (1-2), 195-198.

72. Smith, A. T.; Smith, K. P.; Rosenzweig, A. C., Diversity of the metal-transporting P 1B-type ATPases. *JBIC Journal of Biological Inorganic Chemistry* **2014**, *19* (6), 947-960.
73. Ayangbenro, A. S.; Babalola, O. O., A new strategy for heavy metal polluted environments: a review of microbial biosorbents. *International Journal of Environmental Research and Public Health* **2017**, *14* (1), 94.
74. Gavrilescu, M., Removal of heavy metals from the environment by biosorption. *Engineering in Life Sciences* **2004**, *4* (3), 219-232.
75. Xu, F. F.; Imlay, J. A., Silver (I), mercury (II), cadmium (II), and zinc (II) target exposed enzymic iron-sulfur clusters when they toxify Escherichia coli. *Appl. Environ. Microbiol.* **2012**, *78* (10), 3614-3621.
76. Valko, M.; Morris, H.; Cronin, M. T. D., Metals, toxicity and oxidative stress. *Current medicinal chemistry* **2005**, *12* (10), 1161-1208.
77. Yasuyuki, M.; Kunihiro, K.; Kurissery, S.; Kanavillil, N.; Sato, Y.; Kikuchi, Y., Antibacterial properties of nine pure metals: a laboratory study using Staphylococcus aureus and Escherichia coli. *Biofouling* **2010**, *26* (7), 851-858.
78. Nishioka, H., Mutagenic activities of metal compounds in bacteria. *Mutation Research/Environmental Mutagenesis and Related Subjects* **1975**, *31* (3), 185-189.
79. Alexander, J. W., History of the Medical Use of Silver. *Surgical Infections* **2009**, *10* (3), 289-292.
80. Dollwet, H. H., Historic uses of copper compounds in medicine. *Trace Elem. Med.* **1985**, *2*, 80-87.
81. Grass, G.; Rensing, C.; Solioz, M., Metallic copper as an antimicrobial surface. *Applied and environmental microbiology* **2011**, *77* (5), 1541-1547.
82. Hobman, J. L.; Crossman, L. C., Bacterial antimicrobial metal ion resistance. *Journal of medical microbiology* **2015**, *64*, 471-497.
83. Turner, R. J., Metal-based antimicrobial strategies. *Microbial biotechnology* **2017**, *10* (5), 1062-1065.
84. Aminov, R. I., A brief history of the antibiotic era: lessons learned and challenges for the future. *Frontiers in microbiology* **2010**, *1*, 134-134.
85. Clardy, J.; Fischbach, M. A.; Currie, C. R., The natural history of antibiotics. *Current Biology* **2009**, *19* (11), R437-R441.
86. Ribeiro da Cunha, B.; Fonseca, L. P.; Calado, C. R. C., Antibiotic Discovery: Where Have We Come from, Where Do We Go? *Antibiotics (Basel, Switzerland)* **2019**, *8* (2), 45.
87. Moore, C. E., Changes in antibiotic resistance in animals. *Science* **2019**, *365* (6459), 1251-1252.
88. Centers for Disease Control and Prevention, *Antibiotic resistance threats in the United States, 2019*. Centers for Disease Control and Prevention, US Department of Health and Human Services: 2019.
89. Högberg, L. D.; Heddini, A.; Cars, O., The global need for effective antibiotics: challenges and recent advances. *Trends in pharmacological sciences* **2010**, *31* (11), 509-515.

90. Ruiz, J., Mechanisms of resistance to quinolones: target alterations, decreased accumulation and DNA gyrase protection. *J Antimicrob Chemother* **2003**, *51* (5), 1109-17.
91. Wolter, N.; Smith, A. M.; Farrell, D. J.; Schaffner, W.; Moore, M.; Whitney, C. G.; Jorgensen, J. H.; Klugman, K. P., Novel Mechanism of Resistance to Oxazolidinones, Macrolides, and Chloramphenicol in Ribosomal Protein L4 of the Pneumococcus. *Antimicrobial Agents and Chemotherapy* **2005**, *49* (8), 3554.
92. Ben-Ami, R.; Rodríguez-Baño, J.; Arslan, H.; Pitout, J. D. D.; Quentin, C.; Calbo, E. S.; Azap, Ö. K.; Arpin, C.; Pascual, A.; Livermore, D. M.; Garau, J.; Carmeli, Y., A Multinational Survey of Risk Factors for Infection with Extended-Spectrum  $\beta$ -Lactamase-Producing Enterobacteriaceae in Nonhospitalized Patients. *Clinical Infectious Diseases* **2009**, *49* (5), 682-690.
93. Munoz-Price, L. S.; Jacoby, G.; Snyderman, D., Extended-spectrum beta-lactamases. *UpToDate online* **2012**.
94. Egorov, A. M.; Ulyashova, M. M.; Rubtsova, M. Y., Bacterial Enzymes and Antibiotic Resistance. *Acta naturae* **2018**, *10* (4), 33-48.
95. Blanco, P.; Hernando-Amado, S.; Reales-Calderon, J. A.; Corona, F.; Lira, F.; Alcalde-Rico, M.; Bernardini, A.; Sanchez, M. B.; Martinez, J. L., Bacterial Multidrug Efflux Pumps: Much More Than Antibiotic Resistance Determinants. *Microorganisms* **2016**, *4* (1), 14.
96. von Wintersdorff, C. J. H.; Penders, J.; van Niekerk, J. M.; Mills, N. D.; Majumder, S.; van Alphen, L. B.; Savelkoul, P. H. M.; Wolffs, P. F. G., Dissemination of Antimicrobial Resistance in Microbial Ecosystems through Horizontal Gene Transfer. *Frontiers in Microbiology* **2016**, *7* (173).
97. Woodford, N.; Ellington, M. J., The emergence of antibiotic resistance by mutation. *Clinical Microbiology and Infection* **2007**, *13* (1), 5-18.
98. Theuretzbacher, U., Accelerating resistance, inadequate antibacterial drug pipelines and international responses. *International Journal of Antimicrobial Agents* **2012**, *39* (4), 295-299.
99. Bragg, R. R.; Meyburgh, C. M.; Lee, J. Y.; Coetzee, M. In *Potential Treatment Options in a Post-antibiotic Era*, Infectious Diseases and Nanomedicine III, Singapore, 2018//; Adhikari, R.; Thapa, S., Eds. Springer Singapore: Singapore, 2018; pp 51-61.
100. Pendleton, J. N.; Gorman, S. P.; Gilmore, B. F., Clinical relevance of the ESKAPE pathogens. *Expert Review of Anti-infective Therapy* **2013**, *11* (3), 297-308.
101. Santajit, S.; Indrawattana, N., Mechanisms of Antimicrobial Resistance in ESKAPE Pathogens. *BioMed research international* **2016**, *2016*, 2475067-2475067.
102. Weiner, L. M.; Webb, A. K.; Limbago, B.; Dudeck, M. A.; Patel, J.; Kallen, A. J.; Edwards, J. R.; Sievert, D. M., Antimicrobial-Resistant Pathogens Associated With Healthcare-Associated Infections: Summary of Data Reported to the National Healthcare Safety Network at the Centers for Disease Control and Prevention, 2011-2014. *Infection control and hospital epidemiology* **2016**, *37* (11), 1288-1301.

103. Weiner, L. M.; Fridkin, S. K.; Aponte-Torres, Z.; Avery, L.; Coffin, N.; Dudeck, M. A.; Edwards, J. R.; Jernigan, J. A.; Konnor, R.; Soe, M. M., Vital signs: Preventing antibiotic-resistant infections in hospitals—United States, 2014. *American Journal of Transplantation* **2016**, *16* (7), 2224-2230.
104. Hidron, A. I.; Edwards, J. R.; Patel, J.; Horan, T. C.; Sievert, D. M.; Pollock, D. A.; Fridkin, S. K., Antimicrobial-resistant pathogens associated with healthcare-associated infections: annual summary of data reported to the National Healthcare Safety Network at the Centers for Disease Control and Prevention, 2006–2007. *Infection Control & Hospital Epidemiology* **2008**, *29* (11), 996-1011.
105. World Health Organization, *Antibacterial agents in clinical development: an analysis of the antibacterial clinical development pipeline, including tuberculosis*; World Health Organization: 2017.
106. Thayer, A., Will the bugs always win? *Chemical & Engineering News* **2016**, *94* (35), 36-43.
107. Pew Charitable Trust, Antibiotics currently in global clinical development. *Pew Charitable Trusts, Philadelphia, PA: [www.pewtrusts.org/en/research-and-analysis/data-visualizations/2014/antibiotics-currently-in-clinical-development](http://www.pewtrusts.org/en/research-and-analysis/data-visualizations/2014/antibiotics-currently-in-clinical-development)* **2020**.
108. Deak, D.; Outterson, K.; Powers, J. H.; Kesselheim, A. S., Progress in the Fight Against Multidrug-Resistant Bacteria? A Review of U.S. Food and Drug Administration-Approved Antibiotics, 2010-2015. *Ann Intern Med* **2016**, *165* (5), 363-72.
109. Aghapour, Z.; Gholizadeh, P.; Ganbarov, K.; Bialvaei, A. Z.; Mahmood, S. S.; Tanomand, A.; Yousefi, M.; Asgharzadeh, M.; Yousefi, B.; Kafil, H. S., Molecular mechanisms related to colistin resistance in Enterobacteriaceae. *Infection and drug resistance* **2019**, *12*, 965-975.
110. Connor, K. A., Newer Intravenous Antibiotics in the Intensive Care Unit: Ceftaroline, Ceftolozane-Tazobactam, and Ceftazidime-Avibactam. *AACN Adv Crit Care* **2016**, *27* (4), 353-357.
111. Hallock, K.; Lee, D.; Ramamoorthy, A., MSI-78, an analogue of the magainin antimicrobial peptides, disrupts lipid bilayer structure via positive curvature strain. *Biophysical Journal* **2003**, *84* (5), 3052-3060.
112. Wang, G.; Li, X.; Wang, Z., APD3: The Antimicrobial Peptide Database as a Tool for Research and Education. *Nucleic Acids Research*: 2016; Vol. 44, pp D1087-D1093.
113. Shai, Y., Mechanism of the binding, insertion and destabilization of phospholipid bilayer membranes by alpha-helical antimicrobial and cell non-selective membrane-lytic peptides. *Biochimica Et Biophysica Acta-Biomembranes* **1999**, *1462* (1-2), 55-70.
114. Zasloff, M., Antimicrobial peptides of multicellular organisms. *Nature* **2002**, *415* (6870), 389-395.
115. Al-Ahmad, A.; Laird, D.; Zou, P.; Tomakidi, P.; Steinberg, T.; Lienkamp, K., Nature-Inspired Antimicrobial Polymers - Assessment of Their Potential for Biomedical Applications. *Plos One* **2013**, *8* (9), e73812.

116. Nelson, D.; Cox, M., Bioenergetics and metabolism. *Lehninger Principles of Biochemistry*. 3rd ed. New York: Worth Publishers **2000**, 598-619,770.
117. Allende, D.; Simon, S. A.; McIntosh, T. J., Melittin-induced bilayer leakage depends on lipid material properties: evidence for toroidal pores. *Biophysical journal* **2005**, *88* (3), 1828-1837.
118. Khandelia, H.; Ipsen, J.; Mouritsen, O., The impact of peptides on lipid membranes. *Biochimica Et Biophysica Acta-Biomembranes* **2008**, *1778* (7-8), 1528-1536.
119. Lee, M.; Hung, W.; Chen, F.; Huang, H., Mechanism and kinetics of pore formation in membranes by water-soluble amphipathic peptides. *Proceedings of the National Academy of Sciences of the United States of America* **2008**, *105* (13), 5087-5092.
120. Epand, R.; Schmitt, M.; Gellman, S.; Epand, R., Role of membrane lipids in the mechanism of bacterial species selective toxicity by two alpha/beta-antimicrobial peptides. *Biochimica Et Biophysica Acta-Biomembranes* **2006**, *1758* (9), 1343-1350.
121. Oren, Z.; Lerman, J.; Gudmundsson, G.; Agerberth, B.; Shai, Y., Structure and organization of the human antimicrobial peptide LL-37 in phospholipid membranes: relevance to the molecular basis for its non-cell-selective activity. *Biochemical Journal* **1999**, *341*, 501-513.
122. Durnaś, B.; Piktel, E.; Wątek, M.; Wollny, T.; Gózdź, S.; Smok-Kalwat, J.; Niemirowicz, K.; Savage, P. B.; Bucki, R., Anaerobic bacteria growth in the presence of cathelicidin LL-37 and selected ceragenins delivered as magnetic nanoparticles cargo. *BMC Microbiology* **2017**, *17* (1), 167.
123. Findlay, F.; Pohl, J.; Svoboda, P.; Shakamuri, P.; McLean, K.; Inglis, N.; Proudfoot, L.; Barlow, P., Carbon Nanoparticles Inhibit the Antimicrobial Activities of the Human Cathelicidin LL-37 through Structural Alteration. *Journal of Immunology* **2017**, *199* (7), 2483-2490.
124. Fumakia, M.; Ho, E., Nanoparticles Encapsulated with LL37 and Serpin A1 Promotes Wound Healing and Synergistically Enhances Antibacterial Activity. *Molecular Pharmaceutics* **2016**, *13* (7), 2318-2331.
125. Niemirowicz, K.; Prokop, I.; Wilczewska, A.; Wnorowska, U.; Piktel, E.; Watek, M.; Savage, P.; Bucki, R., Magnetic nanoparticles enhance the anticancer activity of cathelicidin LL-37 peptide against colon cancer cells. *International Journal of Nanomedicine* **2015**, *10*, 3843-3853.
126. Zharkova, M. S.; Orlov, D. S.; Golubeva, O. Y.; Chakchir, O. B.; Eliseev, I. E.; Grinchuk, T. M.; Shamova, O. V., Application of Antimicrobial Peptides of the Innate Immune System in Combination With Conventional Antibiotics—A Novel Way to Combat Antibiotic Resistance? *Frontiers in Cellular and Infection Microbiology* **2019**, *9* (128).
127. Lienkamp, K.; Kumar, K.; Som, A.; Nusslein, K.; Tew, G., "Doubly Selective" Antimicrobial Polymers: How Do They Differentiate between Bacteria? *Chemistry-a European Journal* **2009**, *15* (43), 11710-11714.
128. Epand, R.; Mowery, B.; Lee, S.; Stahl, S.; Lehrer, R.; Gellman, S.; Epand, R., Dual mechanism of bacterial lethality for a cationic sequence-random copolymer

- that mimics host-defense antimicrobial peptides. *Journal of Molecular Biology* **2008**, *379* (1), 38-50.
129. Mowery, B.; Lee, S.; Kissounko, D.; Epanand, R.; Epanand, R.; Weisblum, B.; Stahl, S.; Gellman, S., Mimicry of antimicrobial host-defense peptides by random copolymers. *Journal of the American Chemical Society* **2007**, *129* (50), 15474-+.
  130. Lam, S.; O'Brien-Simpson, N.; Pantarat, N.; Sulistio, A.; Wong, E.; Chen, Y.; Lenzo, J.; Holden, J.; Blencowe, A.; Reynolds, E.; Qiao, G., Combating multidrug-resistant Gram-negative bacteria with structurally nanoengineered antimicrobial peptide polymers. *Nature Microbiology* **2016**, *1* (11).
  131. Liu, L.; Xu, K.; Wang, H.; Tan, P.; Fan, W.; Venkatraman, S.; Li, L.; Yang, Y., Self-assembled cationic peptide nanoparticles as an efficient antimicrobial agent. *Nature Nanotechnology* **2009**, *4* (7), 457-463.
  132. Gupta, A.; Landis, R. F.; Li, C.-H.; Schnurr, M.; Das, R.; Lee, Y.-W.; Yazdani, M.; Liu, Y.; Kozlova, A.; Rotello, V. M., Engineered Polymer Nanoparticles with Unprecedented Antimicrobial Efficacy and Therapeutic Indices against Multidrug-Resistant Bacteria and Biofilms. *Journal of the American Chemical Society* **2018**, *140* (38), 12137-12143.
  133. Williams, D. N.; Ehrman, S. H.; Pulliam Holoman, T. R., Evaluation of the microbial growth response to inorganic nanoparticles. *Journal of Nanobiotechnology* **2006**, *4* (1), 3.
  134. Fayaz, A.; Balaji, K.; Girilal, M.; Yadav, R.; Kalaichelvan, P.; Venketesan, R., Biogenic synthesis of silver nanoparticles and their synergistic effect with antibiotics: a study against gram-positive and gram-negative bacteria. *Nanomedicine-Nanotechnology Biology and Medicine* **2010**, *6* (1), 103-109.
  135. You, C.; Han, C.; Wang, X.; Zheng, Y.; Li, Q.; Hu, X.; Sun, H., The progress of silver nanoparticles in the antibacterial mechanism, clinical application and cytotoxicity. *Molecular Biology Reports* **2012**, *39* (9), 9193-9201.
  136. Pal, S.; Tak, Y. K.; Song, J. M., Does the Antibacterial Activity of Silver Nanoparticles Depend on the Shape of the Nanoparticle? A Study of the Gram-Negative Bacterium *Escherichia coli*. *Applied and Environmental Microbiology* **2007**, *73* (6), 1712.
  137. Courtney, C.; Goodman, S.; Nagy, T.; Levy, M.; Bhusal, P.; Madinger, N.; Detweiler, C.; Nagpal, P.; Chatterjee, A., Potentiating antibiotics in drug-resistant clinical isolates via stimuli-activated superoxide generation. *Science Advances* **2017**, *3* (10).
  138. Goodman, S. M.; Levy, M.; Li, F.-F.; Ding, Y.; Courtney, C. M.; Chowdhury, P. P.; Erbse, A.; Chatterjee, A.; Nagpal, P., Designing Superoxide-Generating Quantum Dots for Selective Light-Activated Nanotherapy. *Frontiers in Chemistry* **2018**, *6* (46).
  139. Levy, M.; Courtney, C. M.; Chowdhury, P. P.; Ding, Y.; Grey, E. L.; Goodman, S. M.; Chatterjee, A.; Nagpal, P., Assessing Different Reactive Oxygen Species as Potential Antibiotics: Selectivity of Intracellular Superoxide Generation Using Quantum Dots. *ACS Applied Bio Materials* **2018**, *1* (2), 529-537.

140. Bresee, J.; Bond, C.; Worthington, R.; Smith, C.; Gifford, J.; Simpson, C.; Carter, C.; Wang, G.; Hartman, J.; Osbaugh, N.; Shoemaker, R.; Melander, C.; Feldheim, D., Nanoscale Structure-Activity Relationships, Mode of Action, and Biocompatibility of Gold Nanoparticle Antibiotics. *Journal of the American Chemical Society* **2014**, *136* (14), 5295-5300.
141. Turos, E.; Reddy, G.; Greenhalgh, K.; Ramaraju, P.; Abeylath, S.; Jang, S.; Dickey, S.; Lim, D., Penicillin-bound polyacrylate nanoparticles: Restoring the activity of beta-lactam antibiotics against MRSA. *Bioorganic & Medicinal Chemistry Letters* **2007**, *17* (12), 3468-3472.
142. Tsay, J. M.; Trzoss, M.; Shi, L.; Kong, X.; Selke, M.; Jung, M. E.; Weiss, S., Singlet Oxygen Production by Peptide-Coated Quantum Dot-Photosensitizer Conjugates. *Journal of the American Chemical Society* **2007**, *129* (21), 6865-6871.
143. Zhang, F.; Yi, D.; Sun, H.; Zhang, H., Cadmium-based quantum dots: preparation, surface modification, and applications. *J Nanosci Nanotechnol* **2014**, *14* (2), 1409-24.
144. Åkerman, M. E.; Chan, W. C. W.; Laakkonen, P.; Bhatia, S. N.; Ruoslahti, E., Nanocrystal targeting in vivo. *Proceedings of the National Academy of Sciences* **2002**, *99* (20), 12617-12621.
145. Fu, P.; Xia, Q.; Hwang, H.; Ray, P.; Yu, H., Mechanisms of nanotoxicity: Generation of reactive oxygen species. *Journal of Food and Drug Analysis* **2014**, *22* (1), 64-75.
146. Li, Y.; Zhang, W.; Niu, J.; Chen, Y., Mechanism of Photogenerated Reactive Oxygen Species and Correlation with the Antibacterial Properties of Engineered Metal-Oxide Nanoparticles. *ACS Nano* **2012**, *6* (6), 5164-5173.
147. Li, X.; Xie, J.; Liao, L.; Jiang, X.; Fu, H., UV-curable polyurethane acrylate-Ag/TiO<sub>2</sub> nanocomposites with superior UV light antibacterial activity. *International Journal of Polymeric Materials and Polymeric Biomaterials* **2017**, *66* (16), 835-843.
148. Williams, D. N.; Pramanik, S.; Brown, R. P.; McIntire, E.; Zi, B.; Haynes, C.; Rosenzweig, Z., Adverse Interaction of Luminescent Semiconductor Quantum Dots with Liposomes and *Shewanella oneidensis*. *ACS Applied Nanomaterials* **2018**, *1* (9), 4788-4800.
149. Williams, D. N.; Saar, J. S.; Bleicher, V.; Rau, S.; Lienkamp, K.; Rosenzweig, Z., Poly(oxanorbornene)-Coated CdTe Quantum Dots as Antibacterial Agents. *ACS Applied Bio Materials* **2020**, *3* (2), 1097-1104.
150. Huang, J.; Mulfort, K. L.; Du, P.; Chen, L. X., Photodriven charge separation dynamics in CdSe/ZnS core/shell quantum dot/cobaloxime hybrid for efficient hydrogen production. *Journal of the American Chemical Society* **2012**, *134* (40), 16472-16475.
151. Yuan, Y.-J.; Chen, D.; Yu, Z.-T.; Zou, Z.-G., Cadmium sulfide-based nanomaterials for photocatalytic hydrogen production. *Journal of Materials Chemistry A* **2018**, *6* (25), 11606-11630.
152. Wu, Q.; Hou, J.; Zhao, H.; Liu, Z.; Yue, X.; Peng, S.; Cao, H., Charge recombination control for high efficiency CdS/CdSe quantum dot co-sensitized solar cells with multi-ZnS layers. *Dalton Transactions* **2018**, *47* (7), 2214-2221.

153. Lu, W.; Song, B.; Li, H.; Zhou, J.; Dong, W.; Zhao, G.; Han, G., Strategy for performance enhancement of Cd<sub>1-x</sub>Zn<sub>x</sub>Te/CdS core/shell quantum dot sensitized solar cells through band adjustment. *Journal of Alloys and Compounds* **2020**, *826*, 154050.
154. Kim, S.; Im, S. H.; Kim, S.-W., Performance of light-emitting-diode based on quantum dots. *Nanoscale* **2013**, *5* (12), 5205-5214.
155. Ratnesh, R. K., Hot injection blended tunable CdS quantum dots for production of blue LED and a selective detection of Cu<sup>2+</sup> ions in aqueous medium. *Optics & Laser Technology* **2019**, *116*, 103-111.
156. Subramaniyan, S. B.; Veerappan, A., Water soluble cadmium selenide quantum dots for ultrasensitive detection of organic, inorganic and elemental mercury in biological fluids and live cells. *RSC advances* **2019**, *9* (39), 22274-22281.
157. Sadeghi, S.; Abkenar, S. K.; Ow-Yang, C. W.; Nizamoglu, S., Efficient White LEDs Using Liquid-state Magic-sized CdSe Quantum Dots. *Scientific reports* **2019**, *9* (1), 1-9.
158. Liu, W.; Zhang, Y.; Ruan, C.; Wang, D.; Zhang, T.; Feng, Y.; Gao, W.; Yin, J.; Wang, Y.; Riley, A.; Hu, M.; Yu, W., ZnCuInS/ZnSe/ZnS Quantum Dot-Based Downconversion Light-Emitting Diodes and Their Thermal Effect. *Journal of Nanomaterials* **2015**.
159. Medintz, I.; Uyeda, H.; Goldman, E.; Mattoussi, H., Quantum dot bioconjugates for imaging, labelling and sensing. *Nature Materials* **2005**, *4* (6), 435-446.
160. Faroon, O.; Ashizawa, A.; Wright, S.; Tucker, P.; Jenkins, K.; Ingerman, L.; Rudisill, C., Toxicological profile for cadmium. **2012**.
161. Xie, R.; Battaglia, D.; Peng, X., Colloidal InP nanocrystals as efficient emitters covering blue to near-infrared. *Journal of the American Chemical Society* **2007**, *129* (50), 15432-+.
162. Reisch, A.; Klymchenko, A. S., Fluorescent Polymer Nanoparticles Based on Dyes: Seeking Brighter Tools for Bioimaging. *Small (Weinheim an der Bergstrasse, Germany)* **2016**, *12* (15), 1968-1992.
163. Singh, R. K.; Kumar, R.; Singh, D. P.; Savu, R.; Moshkalev, S. A., Progress in microwave-assisted synthesis of quantum dots (graphene/carbon/semiconducting) for bioapplications: a review. *Materials Today Chemistry* **2019**, *12*, 282-314.
164. Ippen, C.; Greco, T.; Kim, Y.; Kim, J.; Oh, M.; Han, C.; Wedel, A., ZnSe/ZnS quantum dots as emitting material in blue QD-LEDs with narrow emission peak and wavelength tunability. *Organic Electronics* **2014**, *15* (1), 126-131.
165. Mei, B.; Susumu, K.; Medintz, I.; Mattoussi, H., Polyethylene glycol-based bidentate ligands to enhance quantum dot and gold nanoparticle stability in biological media. *Nature Protocols* **2009**, *4* (3), 412-423.
166. Mei, B.; Susumu, K.; Medintz, I.; Delehanty, J.; Mountziaris, T.; Mattoussi, H., Modular poly(ethylene glycol) ligands for biocompatible semiconductor and gold nanocrystals with extended pH and ionic stability. *Journal of Materials Chemistry* **2008**, *18* (41), 4949-4958.

167. Sinatra, L.; Pan, J.; Bakr, O. M., Methods of synthesizing monodisperse colloidal quantum dots. *Material Matters* **2017**, *12*, 3-7.
168. Murray, C. B.; Kagan, C. R.; Bawendi, M. G., Synthesis and Characterization of Monodisperse Nanocrystals and Close-Packed Nanocrystal Assemblies. *Annual Review of Materials Science* **2000**, *30* (1), 545-610.
169. Yu, W.; Qu, L.; Guo, W.; Peng, X., Experimental determination of the extinction coefficient of CdTe, CdSe and CdS nanocrystals (vol 15, pg 2854, 2003). *Chemistry of Materials* **2004**, *16* (3), 560-560.
170. Lyons, T.; Williams, D.; Rosenzweig, Z., Addition of Fluorescence Lifetime Spectroscopy to the Tool Kit Used to Study the Formation and Degradation of Luminescent Quantum Dots in Solution. *Langmuir* **2017**, *33* (12), 3018-3027.
171. Wang, K.; Li, N.; Hai, X.; Dang, F., Lysozyme-mediated fabrication of well-defined core-shell nanoparticle@metal-organic framework nanocomposites. *Journal of Materials Chemistry A* **2017**, *5* (39), 20765-20770.
172. Heidelberg, J.; Paulsen, I.; Nelson, K.; Gaidos, E.; Nelson, W.; Read, T.; Eisen, J.; Seshadri, R.; Ward, N.; Methe, B.; Clayton, R.; Meyer, T.; Tsapin, A.; Scott, J.; Beanan, M.; Brinkac, L.; Daugherty, S.; DeBoy, R.; Dodson, R.; Durkin, A.; Haft, D.; Kolonay, J.; Madupu, R.; Peterson, J.; Umayam, L.; White, O.; Wolf, A.; Vamathevan, J.; Weidman, J.; Impraim, M.; Lee, K.; Berry, K.; Lee, C.; Mueller, J.; Khouri, H.; Gill, J.; Utterback, T.; McDonald, L.; Feldblyum, T.; Smith, H.; Venter, J.; Nealson, K.; Fraser, C., Genome sequence of the dissimilatory metal ion-reducing bacterium *Shewanella oneidensis*. *Nature Biotechnology* **2002**, *20* (11), 1118-1123.
173. Pu, C.; Ma, J.; Qin, H.; Yan, M.; Fu, T.; Niu, Y.; Yang, X.; Huang, Y.; Zhao, F.; Peng, X., Doped Semiconductor-Nanocrystal Emitters with Optimal Photoluminescence Decay Dynamics in Microsecond to Millisecond Range: Synthesis and Applications. *Acs Central Science* **2016**, *2* (1), 32-39.
174. Zhang, L.; Shen, X.; Liang, H.; Chen, F.; Huang, H., Phosphine-free synthesis of ZnSe:Mn and ZnSe:Mn/ZnS doped quantum dots using new Se and S precursors. *New Journal of Chemistry* **2014**, *38* (1), 448-454.
175. Haldar, S.; Chattopadhyay, A., Application of NBD-labeled lipids in membrane and cell biology. In *Fluorescent Methods to Study Biological Membranes*, Springer: Berlin, Heidelberg, 2012; Vol. 13.
176. Amaro, M.; Filipe, H. A. L.; Ramalho, J. P. P.; Hof, M.; Loura, L. M. S., Fluorescence of nitrobenzoxadiazole (NBD)-labeled lipids in model membranes is connected not to lipid mobility but to probe location. *Physical Chemistry Chemical Physics* **2016**, *18* (10), 7042-7054.
177. Zheng, Z.; Saar, J.; Zhi, B.; Qiu, T. A.; Gallagher, M. J.; Fairbrother, D. H.; Haynes, C. L.; Lienkamp, K.; Rosenzweig, Z., Structure-Property Relationships of Amine-rich and Membrane-Disruptive Poly(oxonorborene)-Coated Gold Nanoparticles. *Langmuir* **2018**, *34* (15), 4614-4625.
178. Fortier, C. Preparation, Characterization, And Application of Liposomes in the Study of Lipid Oxidation Targeting Hydroxyl Radicals. University of New Orleans, University of New Orleans Theses and Dissertations, 2008.

179. Arbeloa, F. L.; Ojeda, P. R.; Arbeloa, I. L., Fluorescence self-quenching of the molecular forms of Rhodamine B in aqueous and ethanolic solutions. *Journal of luminescence* **1989**, *44* (1-2), 105-112.
180. Wenger, W.; Bates, F.; Aydile, E., Functionalization of Cadmium Selenide Quantum Dots with Poly(ethylene glycol): Ligand Exchange, Surface Coverage, and Dispersion Stability. *Langmuir* **2017**, *33* (33), 8239-8245.
181. Were, L.; Bruce, B.; Davidson, P.; Weiss, J., Size, stability, and entrapment efficiency of phospholipid nanocapsules containing polypeptide antimicrobials. *Journal of Agricultural and Food Chemistry* **2003**, *51* (27), 8073-8079.
182. Xie, R.; Kolb, U.; Li, J.; Basche, T.; Mews, A., Synthesis and characterization of highly luminescent CdSe-Core CdS/Zn<sub>0.5</sub>Cd<sub>0.5</sub>S/ZnS multishell nanocrystals. *Journal of the American Chemical Society* **2005**, *127* (20), 7480-7488.
183. Cornelison, G.; Mihic, S., Contaminating levels of zinc found in commonly-used labware and buffers affect glycine receptor currents. *Brain Research Bulletin* **2014**, *100*, 1-5.
184. Wang, X.; Yu, J.; Chen, R., Optical Characteristics of ZnS Passivated CdSe/CdS Quantum Dots for High Photostability and Lasing. *Scientific Reports* **2018**, *8* (1), 17323.
185. Dabbousi, B.; RodriguezViejo, J.; Mikulec, F.; Heine, J.; Mattoussi, H.; Ober, R.; Jensen, K.; Bawendi, M., (CdSe)ZnS core-shell quantum dots: Synthesis and characterization of a size series of highly luminescent nanocrystallites. *Journal of Physical Chemistry B* **1997**, *101* (46), 9463-9475.
186. Baranov, A. V.; Rakovich, Y. P.; Donegan, J. F.; Perova, T. S.; Moore, R. A.; Talapin, D. V.; Rogach, A. L.; Masumoto, Y.; Nabiev, I., Effect of ZnS shell thickness on the phonon spectra in CdSe quantum dots. *Physical Review B* **2003**, *68* (16), 165306.
187. Florence, T. M.; Batley, G. E., Determination of the chemical forms of trace metals in natural waters, with special reference to copper, lead, cadmium and zinc. *Talanta* **1977**, *24* (3), 151-158.
188. Barceloux, D. G., Selenium. *J Toxicol Clin Toxicol* **1999**, *37* (2), 145-72.
189. Al-Hajaj, N. A.; Moquin, A.; Neibert, K. D.; Soliman, G. M.; Winnik, F. o. M.; Maysinger, D., Short ligands affect modes of QD uptake and elimination in human cells. *Acs Nano* **2011**, *5* (6), 4909-4918.
190. Gao, X.; Li, D.; Tong, Y.; Ge, D.; Tang, Y.; Zhang, D.; Li, J., Highly sensitive fluorescence detection of glycoprotein based on energy transfer between CuInS<sub>2</sub> QDs and rhodamine B. *Luminescence* **2015**, *30* (8), 1389-1394.
191. Wang, W.; Guo, Y.; Tiede, C.; Chen, S.; Kopytynski, M.; Kong, Y.; Kulak, A.; Tomlinson, D.; Chen, R.; McPherson, M.; Zhou, D., Ultraefficient Cap-Exchange Protocol To Compact Biofunctional Quantum Dots for Sensitive Ratiometric Biosensing and Cell Imaging. *Acs Applied Materials & Interfaces* **2017**, *9* (18), 15232-15244.
192. Chou, K. F.; Dennis, A. M., Förster Resonance Energy Transfer between Quantum Dot Donors and Quantum Dot Acceptors. *Sensors (Basel, Switzerland)* **2015**, *15* (6), 13288-13325.

193. Shamirian, A.; Ghai, A.; Snee, P. T., QD-Based FRET Probes at a Glance. *Sensors (Basel, Switzerland)* **2015**, *15* (6), 13028-13051.
194. Dietrich, A.; Buschmann, V.; Müller, C.; Sauer, M., Fluorescence resonance energy transfer (FRET) and competing processes in donor–acceptor substituted DNA strands: a comparative study of ensemble and single-molecule data. *Reviews in Molecular Biotechnology* **2002**, *82* (3), 211-231.
195. Hoekstra, D.; De Boer, T.; Klappe, K.; Wilschut, J., Fluorescence method for measuring the kinetics of fusion between biological membranes. *Biochemistry* **1984**, *23* (24), 5675-5681.
196. Mensch, A. C.; Melby, E. S.; Laudadio, E. D.; Foreman-Ortiz, I. U.; Zhang, Y.; Dohnalkova, A.; Hu, D.; Pedersen, J. A.; Hamers, R. J.; Orr, G., Preferential interactions of primary amine-terminated quantum dots with membrane domain boundaries and lipid rafts revealed with nanometer resolution. *Environmental Science: Nano* **2020**.
197. Buchman, J. T.; Rahnamoun, A.; Landy, K. M.; Zhang, X.; Vartanian, A. M.; Jacob, L. M.; Murphy, C. J.; Hernandez, R.; Haynes, C. L., Using an environmentally-relevant panel of Gram-negative bacteria to assess the toxicity of polyallylamine hydrochloride-wrapped gold nanoparticles. *Environmental Science: Nano* **2018**, *5* (2), 279-288.
198. Lewis, R. W.; Bertsch, P. M.; McNear, D. H., Nanotoxicity of engineered nanomaterials (ENMs) to environmentally relevant beneficial soil bacteria – a critical review. *Nanotoxicology* **2019**, 1-37.
199. Ma, H.; Williams, P. L.; Diamond, S. A., Ecotoxicity of manufactured ZnO nanoparticles—a review. *Environmental Pollution* **2013**, *172*, 76-85.
200. Das, P.; Xenopoulos, M. A.; Williams, C. J.; Hoque, M. E.; Metcalfe, C. D., Effects of silver nanoparticles on bacterial activity in natural waters. *Environmental toxicology and Chemistry* **2012**, *31* (1), 122-130.
201. Khan, S. S.; Mukherjee, A.; Chandrasekaran, N., Studies on interaction of colloidal silver nanoparticles (SNPs) with five different bacterial species. *Colloids and Surfaces B: Biointerfaces* **2011**, *87* (1), 129-138.
202. Hang, M.; Gunsolus, I.; Wayland, H.; Melby, E.; Mensch, A.; Hurley, K.; Pedersen, J.; Haynes, C.; Hamers, R., Impact of Nanoscale Lithium Nickel Manganese Cobalt Oxide (NMC) on the Bacterium *Shewanella oneidensis* MR-1. *Chemistry of Materials* **2016**, *28* (4), 1092-1100.
203. Wroblewska-Wolna, A. M.; Harvie, A. J.; Rowe, S. F.; Critchley, K.; Butt, J. N.; Jeuken, L. J. C., Quantum dot interactions with and toxicity to *Shewanella oneidensis* MR-1. *Nanotechnology* **2020**, *31* (13), 134005.
204. Feng, Z.; Gunsolus, I.; Qiu, T.; Hurley, K.; Nyberg, L.; Frew, H.; Johnson, K.; Vartanian, A.; Jacob, L.; Lohse, S.; Torelli, M.; Hamers, R.; Murphy, C.; Haynes, C., Impacts of gold nanoparticle charge and ligand type on surface binding and toxicity to Gram-negative and Gram-positive bacteria. *Chemical Science* **2015**, *6* (9), 5186-5196.
205. Verebes, G.; Melchiorre, M.; Garcia-Leis, A.; Ferreri, C.; Marzetti, C.; Torreggiani, A., Hyperspectral enhanced dark field microscopy for imaging blood cells. *Journal of Biophotonics* **2013**, *6* (11-12), 960-967.

206. Gao, L.; Smith, R., Optical hyperspectral imaging in microscopy and spectroscopy - a review of data acquisition. *Journal of Biophotonics* **2015**, *8* (6), 441-456.
207. Zamora-Perez, P.; Tsoutsis, D.; Xu, R.; Rivera-Gil, P., Hyperspectral-Enhanced Dark Field Microscopy for Single and Collective Nanoparticle Characterization in Biological Environments. *Materials* **2018**, *11* (2), 243.
208. Gong, K.; Kelley, D., A predictive model of shell morphology in CdSe/CdS core/shell quantum dots. *Journal of Chemical Physics* **2014**, *141* (19).
209. Yu, Z.; Guo, L.; Du, H.; Krauss, T.; Silcox, J., Shell distribution on colloidal CdSe/ZnS quantum dots. *Nano Letters* **2005**, *5* (4), 565-570.
210. Gao, D.; Zhang, J.; Lyu, B.; Lyu, L.; Ma, J.; Yang, L., Poly(quaternary ammonium salt-epoxy) grafted onto Ce doped ZnO composite: An enhanced and durable antibacterial agent. *Carbohydrate Polymers* **2018**, *200*, 221-228.
211. Organization', W. H., Antimicrobial Resistance: Global Report on Surveillance. WHO Press: 2014.
212. Rather, I. A.; Kim, B. C.; Bajpai, V. K.; Park, Y. H., Self-medication and antibiotic resistance: Crisis, current challenges, and prevention. *Saudi J Biol Sci* **2017**, *24* (4), 808-812.
213. Hartleb, W.; Saar, J.; Zou, P.; Lienkamp, K., Just Antimicrobial is not Enough: Toward Bifunctional Polymer Surfaces with Dual Antimicrobial and Protein-Repellent Functionality. *Macromolecular Chemistry and Physics* **2016**, *217* (2), 225-231.
214. Kurowska, M.; Eickenscheidt, A.; Guevara-Solarte, D.; Widayaya, V.; Marx, F.; Al-Ahmad, A.; Lienkamp, K., A Simultaneously Antimicrobial, Protein-Repellent, and Cell-Compatible Polyzwitterion Network. *Biomacromolecules* **2017**, *18* (4), 1373-1386.
215. Banoee, M.; Seif, S.; Nazari, Z. E.; Jafari-Fesharaki, P.; Shahverdi, H. R.; Moballegh, A.; Moghaddam, K. M.; Shahverdi, A. R., ZnO nanoparticles enhanced antibacterial activity of ciprofloxacin against Staphylococcus aureus and Escherichia coli. *J Biomed Mater Res B Appl Biomater* **2010**, *93* (2), 557-61.
216. Allahverdiyev, A. M.; Kon, K. V.; Abamor, E. S.; Bagirova, M.; Rafailovich, M., Coping with antibiotic resistance: combining nanoparticles with antibiotics and other antimicrobial agents. *Expert review of anti-infective therapy* **2011**, *9* (11), 1035-1052.
217. Ferreira, L. d. S.; Comune, M. A Composition of Gold Nanoparticles having Antimicrobial Peptides Bound on their Surface for use the Treatment of Wound Healing or in the Treatment if Ischemic or Vascular Disease on in the Treatment of Skin Disorders. 2016.
218. Niemirowicz, K.; Piktel, E.; Wilczewska, A.; Markiewicz, K.; Durnas, B.; Watek, M.; Puszkarz, I.; Wroblewska, M.; Niklinska, W.; Savage, P.; Bucki, R., Core-shell magnetic nanoparticles display synergistic antibacterial effects against Pseudomonas aeruginosa and Staphylococcus aureus when combined with cathelicidin LL-37 or selected ceragenins. *International Journal of Nanomedicine* **2016**, *11*.
219. Li, Y.; Li, X.; Li, H.; Lockridge, O.; Wang, G., A novel method for purifying recombinant human host defense cathelicidin LL-37 by utilizing its inherent

- property of aggregation. *Protein Expression and Purification* **2007**, *54* (1), 157-165.
220. Lienkamp, K.; Madkour, A.; Musante, A.; Nelson, C.; Nusslein, K.; Tew, G., Antimicrobial polymers prepared by ROMP with unprecedented selectivity: A molecular construction kit approach. *Journal of the American Chemical Society* **2008**, *130* (30), 9836-9843.
221. Lienkamp, K.; Tew, G., Synthetic Mimics of Antimicrobial Peptides-A Versatile Ring-Opening Metathesis Polymerization Based Platform for the Synthesis of Selective Antibacterial and Cell-Penetrating Polymers. *Chemistry-a European Journal* **2009**, *15* (44), 11784-11800.
222. Lienkamp, K.; Madkour, A.; Kumar, K.; Nusslein, K.; Tew, G., Antimicrobial Polymers Prepared by Ring-Opening Metathesis Polymerization: Manipulating Antimicrobial Properties by Organic Counterion and Charge Density Variation. *Chemistry-a European Journal* **2009**, *15* (43), 11715-11722.
223. Zou, P.; Hartleb, W.; Lienkamp, K., It takes walls and knights to defend a castle - synthesis of surface coatings from antimicrobial and antibiofouling polymers. *Journal of Materials Chemistry* **2012**, *22* (37), 19579-19589.
224. Zou, P.; Laird, D.; Riga, E.; Deng, Z.; Dorner, F.; Perez-Hernandez, H.; Guevara-Solarte, D.; Steinberg, T.; Al-Ahmad, A.; Lienkamp, K., Antimicrobial and cell-compatible surface-attached polymer networks - how the correlation of chemical structure to physical and biological data leads to a modified mechanism of action. *Journal of Materials Chemistry B* **2015**, *3* (30), 6224-6238.
225. Roesslein, M.; Hirsch, C.; Kaiser, J.-P.; Krug, H. F.; Wick, P., Comparability of in vitro tests for bioactive nanoparticles: a common assay to detect reactive oxygen species as an example. *International journal of molecular sciences* **2013**, *14* (12), 24320-24337.
226. Torelli, M. D.; Putans, R. A.; Tan, Y.; Lohse, S. E.; Murphy, C. J.; Hamers, R. J., Quantitative determination of ligand densities on nanomaterials by X-ray photoelectron spectroscopy. *ACS Appl Mater Interfaces* **2015**, *7* (3), 1720-5.
227. Love, J. A.; Morgan, J. P.; Trnka, T. M.; Grubbs, R. H., A Practical and Highly Active Ruthenium-Based Catalyst that Effects the Cross Metathesis of Acrylonitrile. *Angewandte Chemie International Edition* **2002**, *41* (21), 4035-4037.

